DEPARTAMENTO DE ASTROFÍSICA

Universidad de La Laguna

The Star Formation History of Ultra-Faint Dwarf Galaxies

Memoria que presenta
Sara Murabito
para optar al grado de
Doctor por la Universidad de La Laguna

INSTITUTO Đ ASTROFÍSICA Đ CANARIAS
July 2018

Examination date: September, 2018
Thesis supervisor: Dr. Sebastian L. Hidalgo Rodríguez

Alla mia famiglia.
Un pensiero speciale va a mia zia Renza.

> "Le persone non smettono mai di mancarci. Impariamo soltanto a vivere tenendoci dentro, in qualche modo, l'enorme abissale vuoto lasciato dalla loro assenza."
>
> Alyson Noël

Resumen

La formación de galaxias y su evolución es a día de hoy una cuestión por resolver. En el escenario λCDM, las galaxias enanas son los componentes básicos de los cuales se forman las galaxias más grandes (White & Rees 1978; Blumenthal et al. 1984). Las enanas que observamos hoy en día podrían ser sistemas supervivientes que todavía no se han fusionado con galaxias más grandes y pueden por tanto, contener el registro fósil de la evolución temprana del Universo. De acuerdo con este escenario, el análisis de las galaxias enanas del Grupo Local (GL) juega un papel importante en la comprensión de cómo se forman y evolucionan las galaxias. Dado que se pueden resolver en estrellas, este grupo de galaxias ofrece un laboratorio ideal para hacer frente a muchos de los problemas que aún están abiertos en la formación y evolución de galaxias.

Recientemente se ha descubierto una nueva clase de galaxias enanas, las galaxias enanas ultra débiles. Esos son los sistemas estelares más pequeños, dominados por la materia oscura y los menos enriquecidos químicamente en el universo. Las enanas ultra débiles son objetos importantes para comprender la física de la materia oscura y la formación de galaxias en las escalas más pequeñas. Los detalles de su naturaleza proporcionan una contribución empírica crucial para verificar los escenarios de formación de la Vía Láctea (VL). En los últimos años han sido descubiertos muchos nuevos satélites de la Vía Láctea (p.ej, Balbinot et al. 2013; Belokurov et al. 2014; Laevens et al. 2014; Bechtol et al. 2015; Drlica-Wagner et al. 2015; Kim et al. 2015; Koposov et al. 2015a; Laevens et al. 2015b; Martin et al. 2015; Drlica-Wagner et al. 2016; Torrealba et al. 2016; Koposov et al. 2017; Torrealba et al. 2018; Koposov et al. 2018), pero la mayoría de estos nuevos objetos están mal estudiados en términos de su población estelar, parámetros estructurales, distancia y luminosidad.

Esta tesis es parte de un proyecto más amplio, llamado ESPIGA (Early Stellar Poverty In GAlaxies), enfocado en derivar una precisa y homogéneoa historias de formación estelares (HFE) de todas las galaxias resueltas del Grupo Local dentro de ~ 250 Kpc de distancia. La muestra de galaxias analizadas en el presente estudio está compuesta por tres galaxias enanas ultra débiles: Boötes I, Canes Venatici II y Leo IV. Los datos provienen del Telescopio Subaru en

el caso de Boötes I y del Telescopio Espacial Hubble (HST) en el caso de las otras dos galaxias. Para todas estas enanas, hemos obtenido diagramas color-magnitud (DCM) profundos que alcanzan los puntos de giro de las edades más viejas (oMSTO) necesarios para derivar una HFE detallada hasta las edades más avanzadas. También hemos analizamos los datos de Segue II obtenidos con el Telescopio Isaac Newton (INT) pero para esta galaxia no hemos podido obtener un DCM profundo. El DCM es la mejor herramienta para derivar la HFE de las galaxias resueltas. Si el DCM es lo suficientemente profundo se puede observar las estrellas nacidas durante toda la vida de la galaxia (Hidalgo & Aparicio, 2016). La fotometría PSF de Boötes ha sido obtenida con DAOPHOT (Stetson 1987), mientras que en los casos de CvnII y Leo IV la fotometría ha sido obtenida utilizando DOLPHOT (Dolphin 2000). En todos los casos obtenemos una HFE muy precisa, utilizando el método IAC, que consiste en un conjunto de códigos desarrollados por nuestro grupo: IACstar/IAC-pop/MinnIAC (Aparicio & Gallart 2004; Aparicio & Hidalgo 2009; Hidalgo et al. 2011). La HFE de estos sistemas es fundamental para obtener información más detalladas sobre sus poblaciones estelares, y especialmente sobre la presencia de gradientes radiales.

Las soluciones muestran que la HFE de las tres enanas está dominado por un viejo y único episodio principal con un pico que ocurre a $\sim$ 13.5 Gyr y que son sistemas muy pobres en metales ([Fe/H] $<$ -2). Hemos podido calcular la duración del evento inicial de formación estelar a 1.45 Gyr para Boötes I, a 0.78 Gyr para Cvn II y a 1.72 Gyr para Leo IV. Esto significa las galaxias acabaron temprano de formar estrellas.

Generalmente son invocados dos mecanismos principales como responsables de que los subhalos más pequeños no tengan una historia de formación estelar extendida: el calentamiento producido por la radiación de fondo cósmica ultra-violeta (UV) (Bullock et al. 2000) y la retroalimentación por supernovas (Mac Low & Ferrara 1999). El fondo cósmico UV aumenta la entropía del medio inter-galáctico alrededor de la época de reionización, evitando que los bariones caigan en los subhalos más pequeños, y también puede calentar y evaporar el medio interestelar de subhalos más grandes que han logrado cierta formación estelar. Los primeros nunca formarían estrellas, mientras que los segundos mostrarían una población estelar muy antigua (Mac Low & Ferrara 1999; Sawala et al. 2010; Shen et al. 2014; Benítez-Llambay et al. 2015).

Al considerar los resultados de las HFE obtenidas, así como los datos en la literatura, la pregunta que surge es si Boötes I, Cvn II y Leo IV son *verdaderos fósiles* de la era anterior a la reionización en el sentido introducido en Ricotti & Gnedin (2005): una enanas que ha experimentado más del 70% de su formación estelar antes de la fin de la reionización fijada en $\sim$ 12.77 Gyr (Becker et al.

2001) y que tienen una luminosidad $L_V < 10^6 L_\odot$. Todas las galaxias de la muestra satisfacen la segunda condición. En cuanto a la primera condición, la fracción de masa acumulada muestra que Boötes I y Leo IV formaron el 70% de su masa estelar $\sim$ 12 Gyr atrás, mientras que Cvn II formó el 70% de su masa estelar $\sim$ 13 Gyr atrás como derivado de la HFE.

De nuestro análisis basado en los resultados del modelo de Mac Low & Ferrara (1999) y el cálculo de la luminosidad mecánica liberada por SNe durante el breve episodio de formación estelar, podemos situar Boötes I y Canes Venatici II en el régimen de expulsión, mientras podemos colocar Leo IV en el régimen de pérdida de masa, pero bastante cerca del régimen de expulsión. En Boötes I y Cvn II la retroalimentación por SNe ha creado flujos que expulsan completamente el gas, mientras que en Leo IV la pérdida de masa por los vientos galácticos es importante, pero no completa. En otras palabras, Leo IV parece ser lo suficientemente masivo como para conservar al menos una fracción de su gas contra la retroalimentación de SNe. Hay que tener en cuenta que Leo IV tiene el HFE más extendida de las galaxias de esta muestra, alcanzando $\sim$ 1.7 Gyr, y un número total inferior de SNe. Esta evolución más lenta de Leo IV en comparación con las otras galaxias habría permitido a Leo IV de mantener un depósito de gas para seguir formando estrellas.

La masa estelar y la metalicidad son dos de las propiedades físicas fundamentales de las galaxias. Ambas son métrica del proceso de evolución de la galaxia. La primera refleja la cantidad de gas encerrado en estrellas y la segunda refleja el gas reprocesado por las estrellas y cualquier intercambio de gas entre la galaxia y su entorno. Comprender cómo estas cantidades evolucionan con el tiempo y se relacionan entre sí es fundamental para comprender los procesos físicos que regulan la eficiencia y el momento de la formación de estrellas en las galaxias. Hemos calculado la relación masa-metalicidad para las galaxias UFD analizadas en este trabajo y hemos comparado nuestros resultados con los obtenidos por Kirby et al. (2013) para CvnII y Leo IV (Boötes I no está en el muestra de Kirby). Para escalar la masa estelar obtenida en la HFE a toda la galaxia, hemos utilizado la magnitud absoluta de cada galaxia usando McConnachie (2012). De esta forma, hemos calculado la masa estelar total de cada galaxia y la hemos comparado con la metalicidad media obtenida anteriormente. Nuestros resultados están de acuerdo con los obtenidos por Kirby et al. (2013) y, sobre todo, podemos observar que los valores de las metalicidades medias obtenidas a través de la fotometría son muy similares a los obtenidos espectroscópicamente para las tres galaxias.

También hemos estudiado la distribución de las poblaciones estelares en Boötes en función del radio, seleccionando dos regiones en el campo observado.

La HFE obtenida para las regiones interna y externa no es muy diferente de la HFE obtenida para toda la galaxia. Podemos concluir que la galaxia, dentro del campo observado (34 × 27 arcmin) no muestra un gradiente de población estelar.

Se ha demostrado en varios estudios que la fotometría UV permite trazar las diversas subpoblaciones en los cúmulos globulares galácticos mucho mejor que las bandas fotométricas ópticas tradicionales y hacerlo en todo el diagrama color-magnitud, desde la secuencia principal (SP) hasta la rama horizontal. Hemos decidido aplicar, por primera vez, esta técnica para eventualmente trazar la presencia de una subpoblación distinta en Cvn II. Por este motivo, hemos propuesto completar los datos existentes en los filtros F606W y F814W con fotometría en el filtro *u'* de Sloan del Gran Telescopio CANARIAS (GTC13-17A; IP: Sara Murabito) y definir así un nuevo índice fotométrico $c_{u',F606W,F814W}$. Hemos comparado la fotometría ACS con la fotometría OSIRIS utilizando DAOMATCH y DAOMASTER. Nos enfocamos solo en las estrellas RGB ($0.4 < (F606W - F814W) < 0.8$ y $19 < F814W < 24.2$), ya que los datos de GTC llegan a la base de RGB. Desafortunadamente, solo $\sim 27,9\%$ de las estrellas RGB observadas con ACS también se han observado con OSIRIS. Después de mostrar que el problema de estas estrellas perdidas que no se observan con OSIRIS no depende de la región donde se encuentran (por ejemplo, no están cerca de una falla cosmética saturada o muy grande del CCD), podemos concluir que podrían ser más débiles en *u'* de lo esperado. Esto podría ser un indicador de que tenemos un grupo de estrellas en Cvn II con un patrón diferente en metalicidad que el resto de las estrellas. El pseudo-DCM resultante parece mostrar un margen de color en la rama de las gigantes rojas, pero la presencia de múltiples secuencias no es evidente. Por lo tanto, no podemos confirmar o negar la existencia de múltiples poblaciones estelares en Cvn II o en otras galaxias UFD. Lo cierto es que se necesitan más estudios en esta dirección.

Códigos UNESCO: 2101.04, 2209.18.

Abstract

GALAXY formation and evolution is still a fundamental open question in the Universe comprehension. In the hierarchical galaxy formation scenario dwarf galaxies would be the first galaxies ever formed, from which bigger structures would have formed via mergers (White & Rees 1978; Blumenthal et al. 1984). The dwarfs we observe today may be surviving systems that have not (yet) merged with larger galaxies and may contain the fossil record of the early evolution of galaxies and their building blocks. According to this scenario, the analysis of the dwarf galaxies of the Local Group (LG) play a major role in understanding how galaxies form and evolve. Since they can be resolved into stars, this group of galaxies offers a perfect laboratory in addressing the problems still open in galaxy formation and evolution.

A new class, the ultra-faint dwarf galaxies (UFD), has been recently introduced. They are the smallest, the most dark-matter dominated, and the least chemically enriched stellar systems in the Universe. They are important targets for understanding the physics of dark matter and galaxy formation on the smallest scales. The details of their nature provide crucial empirical input for verifying formation scenarios of the Milky Way (MW). Many new MW satellites have been discovered in the last few years (e.g., Balbinot et al. 2013; Belokurov et al. 2014; Laevens et al. 2014; Bechtol et al. 2015; Drlica-Wagner et al. 2015; Kim et al. 2015; Koposov et al. 2015a; Laevens et al. 2015b; Martin et al. 2015; Drlica-Wagner et al. 2016; Torrealba et al. 2016; Koposov et al. 2017; Torrealba et al. 2018; Koposov et al. 2018), but most of these new objects are poorly constrained in terms of their stellar population, structural parameters, distance and luminosity.

This thesis is part of a larger project, called ESPIGA (Early Stellar Populations In GAlaxies), focused on to derive homogeneously accurate star formation histories of all resolved galaxies of the Local Group within $\sim$ 250 Kpc of distance. The sample of galaxies analysed in the present study is composed of three UFD galaxies: Boötes I, Canes Venatici II and Leo IV. The data come from the Subaru Telescope in the case of Boötes I and from the Hubble Space Telescope (HST) in the case of the other two dwarfs. For all these galaxies we have ob-

tained deep CMDs reaching the oMSTO necessary to derive a detailed SFH up to the oldest ages. We also analyzed the Segue II data obtained with the Isaac Newton Telescope (INT) but for this galaxy we have not been able to obtain a deep CMD. The CMD is the best tool to derive the SFH of resolved galaxies. If the CMD is deep enough stars born all over the life-time of the galaxy can be observed (Hidalgo & Aparicio, 2016). The PSF photometry of Boötes has been obtained with DAOPHOT (Stetson 1987), while in the cases of CvnII and Leo IV the photometry has been obtained using DOLPHOT (Dolphin 2000). In all the cases we derived a very accurate SFH, using the IAC-method, which consists a set of codes developed by our group: IACstar/IAC-pop/MinnIAC (Aparicio & Gallart 2004; Aparicio & Hidalgo 2009; Hidalgo et al. 2011). The SFH of these systems is fundamental to obtain deeper insights into their stellar populations, and especially on the presence of radial gradients.

The solutions show that the SFH of the three UFDs is dominated by an old, main episode with a peak occurring $\sim$ 13.5 Gyr ago and that they are very metal-poor ([Fe/H] $<$ -2) systems. We have been able to confine the initial event of star formation to 1.45 Gyr for Boötes I, to 0.78 Gyr for Cvn II and to 1.72 Gyr for Leo IV. This means that they stopped early to form stars. Two main mechanisms are usually invoked as being responsible for the smallest subhalos failing to have an extended star formation history: heating from cosmic ultraviolet (UV) background radiation arising from the earliest star formation in the universe (Bullock et al. 2000) and internal supernova feedback (Mac Low & Ferrara 1999) following the first star formation episodes in the host dwarf galaxy. The cosmic UV background raises the entropy of the intergalactic medium around the epoch of reionization, preventing baryons from falling into the smallest subhalos, and it can also heat and evaporate the interstellar medium of larger subhalos that have managed some star formation. The former would never form stars while the latter would currently show only a very old stellar population (Mac Low & Ferrara 1999; Sawala et al. 2010; Shen et al. 2014; Benítez-Llambay et al. 2015) .

When considering the results of the retrieved SFHs as well as data in literature, the question arising is whether Boötes I, Cvn II and Leo IV are *true fossil* of the pre-reionization era in the sense introduced in Ricotti & Gnedin (2005): a dwarf that has experienced more than the 70% of its star formation before the end of the reionization fixed at $\sim$ 12.77 Gyr (Becker et al. 2001) and that has a luminosity $L_V < 10^6 L_\odot$. All the galaxies of the sample satisfy the second condition. Regarding the first condition, the cumulative mass fraction shows that Boötes I and Leo IV formed 70% of their stellar mass $\sim$ 12 Gyr ago, while Cvn II formed 70% of its stellar mass $\sim$ 13 Gyr ago as derived from the SFH.

From our analysis based on the model results by Mac Low & Ferrara (1999) and the calculation of the mechanical luminosity released from SNe during the brief episode of star formation, we can place Boötes I and Canes Venatici II in the blow-away regime, while place Leo IV in the regime of mass loss, but fairly close to the blow-away regime. In Boötes I and Cvn II the feedback of SNe would have created outflows that completely blow away the gas, whereas in Leo IV the mass loss by galactic winds is important, but not complete. In other words, Leo IV seems to be massive enough to conserve at least a fraction of its gas against SN feedback. Note that Leo IV has the more extended SFH of the galaxies of this sample, reaching $\sim$ 1.7 Gyr, and a lower total number of SNe. This slower evolution of Leo IV compared with the other galaxies of the sample would have allowed to Leo IV keep a gas reservoir to keep forming stars.

Stellar mass and metallicity are two of the most fundamental physical properties of galaxies. Both are metrics of the galaxy evolution process, the former reflecting the amount of gas locked up into stars, and the latter reflecting the gas reprocessed by stars and any exchange of gas between the galaxy and its environment. Understanding how these quantities evolve with time and in relation to one another is central to understanding the physical processes that govern the efficiency and timing of star formation in galaxies. We have calculated the mass–metallicity relation for the UFD galaxies analyzed in this work and we have compared our results which those obtained by Kirby et al. (2013) for CvnII and Leo IV (Boötes I is not in the Kirby's sample). In order to scale the stellar mass obtained from the SFH to the whole galaxy, we have used the absolute magnitude of each galaxy from McConnachie (2012). In this way we have calculated the total stellar mass of each galaxy and compared it with the mean metallicity obtained previously. Our results are in agreement with those obtained by Kirby et al. (2013) and, above all, we can note that the values of the mean metallicities obtained through photometry are very similar to those obtained spectroscopically for the three galaxies.

We have also studied the distribution of stellar populations in Boötes as a function of radius, selecting two regions in the field observed. The SFH obtained for the inner and outer regions does not differ substantially from that obtained for the entire galaxy. So we can say that the galaxy, within the observed field (34×27 arcmin) does not shows an stellar population gradient.

It has been shown in several studies that UV photometry allows to trace the various sub-populations in the Galactic GCs much better than the traditional optical photometric bands and do so across the whole color-magnitude diagram, from the main sequence (MS) all the way to the horizontal branch (HB). We decided to apply - for the first time - this technique to eventually trace the presence

of distinct sub-population in Cvn II. For this reason, we propose to complete the existing F606W and F814W data with photometry in the Sloan u' filter at Gran Telescopio CANARIAS (GTC13-17A; IP: Sara Murabito) and define a new photometric index $c_{u',F606W,F814W}$. We have matched the ACS photometry with the OSIRIS photometry using DAOMATCH and DAOMASTER. We focused only in the RGB stars ($0.4 < (F606W - F814W) < 0.8$ and $19 < F814W < 24.2$), since the GTC data reach to the base of RGB. Unfortunately only $\sim 27,9\%$ of the RGB stars observed with ACS have also been observed with OSIRIS. After showing that the problem of these missing stars not observed with OSIRIS not depends on the region where they are located (e.g. are not near a saturated or very large cosmetic failure of the CCD), we can hypothesize that they might be much dimmer in u' than expected. This could be an indicator that we have a group of stars in Cvn II with a different pattern in metallicity than the rest of the stars. The resulting pseudo-CMD seems to show a color spread in the RGB, but the presence of multiple sequences is not evident. So, we can not confirm or deny the existence of multiple stellar populations in Cvn II or in others UFDs galaxies. What is certain is that further studies are needed in this direction.

Códigos UNESCO: 2101.04, 2209.18.

Contents

List of Figures

List of Tables

1

Introduction

GALAXY formation and evolution are still open questions in astronomy. A large observational effort has been undertaken in the past decades trying to shed some light on the problem, resulting in a true explosion of data and discoveries. In this sense, the galaxies of the Local Group (LG) offer an unique opportunity to study the galaxy evolution. Due to their proximity, they can be largely resolved into their individual stars, an therefore they can be studied with unparalleled detail. The realization that relics of the primeval Universe may still be identifiable in such stars, has fostered the development of what we now know as "near-field cosmology".

This has been accompanied by technological evolution in the telescopes and detectors which have provided higher and higher quality data: precise wide-field photometry, and more recently, individual spectra of tens or even hundreds of stars in these galaxies. Our understanding of the nearby Universe has progressed hand in hand with this technological development, having as a result large number of papers analysing the star formation history (SFH) and the chemodynamics of these galaxies (see Mateo 1998, McConnachie 2012; and references therein).

1.1 Cosmological Context

The standard cosmological model, "Big Bang", has been parametrised assuming several theoretical scenarios depending on the Universe matter distribution. These parametrizations account for the amount of the four types of matter known, or hypothesised: the cold, warm and hot dark matter and the baryonic matter. In the early 1990s, with the discovery of CMB anisotropy by COBE,

the so-called Lambda Cold Dark Matter (ΛCDM) model started to be under consideration as a possible scenario. This cosmological model, in which the Universe is dominated by dark energy and cold dark matter, is nowadays widely accepted and it has been supported by several measurements (WMAP, COBE among others). So far, ΛCDM appears to accurately describe the large-scale properties and evolution of Universe.

In a Universe dominated by Dark Matter and Dark Energy, galaxy formation is a complicated mixture of dark matter assembly, gas infall and secular evolution. The current model for the formation and evolution of the Universe predicts a hierarchical assembly of collapsed structures, with small, low mass dark matter haloes forming first and then subsequently merging to form more massive structures (White & Rees 1978; Blumenthal et al. 1984). Dwarfs would be the first galaxies ever formed, from which bigger structures would have formed via mergers (Blumenthal et al. 1985, Dekel & Silk 1986, Navarro et al. 1995, Moore et al. 1998). The dwarfs we observe today may be surviving systems that have not (yet) merged with larger galaxies and may contain the fossil record of the early evolution of galaxies and their building blocks. In such a picture, the baryonic component (i.e. the gas) will initially fall into the potential wells created by the dark matter haloes; then it will begin to efficiently cool in the centre of the overdensity, and eventually lead to the formation of stars and galaxies.

In the so-called standard model for cosmology, gravity is described by general relativity under the presence of a cosmological constant Λ (Riess et al. 1998; Perlmutter et al. 1999) and the matter component is dominated by Cold Dark Matter (Peebles 1984). While on large scales (>Mpc) this model is very successful in predicting the observed structure of the Universe, it has been often claimed to have some issues in reproducing observations concerning the low mass end of the galaxy population. Those challenges of the ΛCDM model on small scales became known as the missing satellites problem (Klypin et al. 1999; Moore 1994), the cusp-core tension (Flores & Primack 1994; Moore 1994 ; Oh et al. 2015) and the too-big-to-fail problem (Boylan-Kolchin et al. 2011). Several of these issues arise in local galaxies and mostly in the satellites around the Milky Way, so investigating the low mass end (the edge) of galaxy formation, i.e. galaxies with stellar masses below $\approx 10^7 M_{\odot}$, can provide very important insights on the validity of our current cosmological model.

However the physics involved in the process of structure formation becomes more and more complicated when going from large scales, that can be well described just by gravity, to small scales where baryonic effects like gas cooling, star formation and feedback play major roles. It has been pointed out that most if not all of the failures of ΛCDM can be alleviated when pure N-body simu-

lations are replaced by more sophisticated hydrodynamical simulations which include all baryonic effects mentioned above (Dutton et al. 2016).

1.1.1 Missing satellite problem

The cosmological paradigm based on cold dark matter (CDM) and dark energy (λ) has been extremely successful in describing the observed evolution and large-scale structure of our universe. At small scales, however, a number of observations seem to be at odds with the predictions of λCDM cosmology. In particular, over a decade ago, it was pointed out by Moore et al. (1999) and Klypin et al. (1999) that the number of high-mass subhalos predicted by high-resolution CDM simulations exceeds the observed number of luminous satellites of the Milky Way (MW) by at least an order of magnitude. This has become known as the "missing satellites problem"(MSP). Although this problem has been mitigated to a degree by the discovery of a number of additional faint satellite galaxies (Willman et al. 2005; Irwin et al. 2007; Liu et al. 2008; Martin et al. 2008b; Simon & Geha 2007; Grebel & Chu 2000; van den Bergh 2000; Belokurov et al. 2008; Watkins et al. 2009; Belokurov et al. 2010), there remains a considerable discrepancy between the number of observed MW satellites and the number predicted in CDM simulations. Efforts to resolve this issue have fallen into two broad categories. First, there are proposals in which the star formation rate in satellite galaxies is suppressed, leading to large numbers of low-mass subhalos which are simply unobservable. Possible means for such suppression include photoevaporation resulting from ionizing radiation, e.g., at reionization (Quinn et al. 1996; Thoul & Weinberg 1996; Navarro & Steinmetz 1997; Klypin et al. 1999; Barkana & Loeb 1999; Gnedin 2000; Hoeft et al. 2006; Madau et al. 2008; Alvarez et al. 2009) or lower z due to blazars (Pfrommer et al. 2012), or due to cosmic ray heating (Wadepuhl & Springel 2011). Photoionization is expected to suppress star formation in halos below $\sim 10^9 M_\odot$ (Okamoto et al. 2008b). In more massive halos where gas is retained and star formation can begin, further suppression is expected from supernova feedback (Dekel & Silk 1986; Benson et al. 2002; Dekel & Woo 2003; Governato et al. 2007). It is also important to consider the number of faint satellites that remain undetected due to observational incompleteness (Willman et al. 2004; Simon & Geha 2007; Tollerud et al. 2008; Walsh et al. 2009; Koposov et al. 2009; Rashkov et al. 2012). Taken together, it is possible that observational incompleteness combined with suppression of star formation can bring the number of luminous satellites into line with the number of predicted satellites around an MW-mass galaxy.

In the last decade, the incorporation of baryons to hydrodynamic simulations seems to have solved the MSP, although the required fraction of baryons to dark

matter has to be carefully controlled (Peñarrubia et al. 2012).

A second class of possible solutions to the MSP considers departures from the standard assumptions of cold and collisionless DM. Whereas typical particle DM models predict that weakly interacting massive particles (WIMPs) will form halos with masses as small as $10^6 M_\odot$ or so (depending on the temperature at which the WIMPs undergo kinetic decoupling with the cosmic neutrino background), the formation of small-scale structure can be strongly suppressed if the DM particles are not entirely cold (Colín et al. 2000; Macciò & Fontanot 2010; Lovell et al. 2012). DM in the form of sterile neutrinos with masses of $\sim$ 1–10 keV have received attention within this context (Dodelson & Widrow 1994), although many other warm dark matter (WDM) scenarios could potentially accommodate a similar suppression of small-scale power (Pagels & Primack 1982; Hooper et al. 2007). WDM primarily addresses the low-mass end of the MSP by suppressing the formation of small-scale structure. It can also help at the high-mass end, however, because the delayed halo collapse times in a WDM cosmology result in lower concentrations and hence reduced central densities (Lovell et al. 2012).

1.1.2 Cusp-core problem

In the early 1990s, the first results of numerical N-body simulations of dark matter halos based on the collisionless cold dark matter (CDM) prescription became available. These did not show the observed core-like behaviour in their inner parts, but were better described by a steep power-law mass-density distribution, the so-called *cusp*. Fits to the mass-distributions as derived from these early simulations (Dubinski & Carlberg 1991; Navarro et al. 1996, 1997) indicated an inner distribution $\rho \sim r^\alpha$ with $\alpha = -1$. (In the following we will use α to indicate the inner mass density power-law slope.)

The results from these and later simulations are based on the (λ)CDM paradigm, where most of the mass-energy of our universe consists of collisionless CDM in combination with a cosmological constant λ. This λCDM paradigm provides a comprehensive description of the universe at large scales (as shown most recently by the Wilkinson Microwave Anisotropy Probe (WMAP) results; see Spergel et al. 2007). However, despite these great successes, it should be kept in mind that the cusp and the central dark matter distribution are not predicted from first principles by λCDM. Rather, these properties are derived from analytical fits made to dark-matter-only numerical simulations. While the quality and quantity of these simulations has improved by orders of magnitude over the years, there is as yet no "cosmological theory" that explains and correctly predicts the distribution of dark matter in galaxies from first principles.

The value $\alpha = -1$ found in the early CDM simulations is very different from that expected in the *pseudo-isothermal* (PI) model, where the constant density core ($\rho \sim r^0$) implies $\alpha = 0$. These two cases thus lead to two very different descriptions of the dark matter distribution in galaxies. The "cusp" ($\alpha = -1$) models gives rise to a rapidly increasing "spiky" dark matter density towards the center, while the "core" model ($\alpha = 0$) has an approximately constant dark matter density. The cusp model therefore has a rotation curve that will rise as the square-root of the radius, while the core model rotation curve rises in a linear fashion. The difference in shapes between the rotation curves of both models is quite pronounced, and, in principle, it should therefore be possible to identify CDM haloes in real galaxies by measuring their rotation curves.

Over the last 15 years or so, much effort has been put into determining the central mass distribution in galaxies using their rotation curves, and comparing them with the outcomes of ever more sophisticated numerical simulations. To first order, one can summarize this work as observational determinations yielding slopes $\alpha = 0$, while simulations produce $\alpha = -1$ slopes. This persistent difference is known as the "core/cusp controversy", sometimes also described as "the small-scale crisis in cosmology".

1.1.3 Too-Big-to-Fail

Even though λCDM is extremely successful at reproducing the large-scale characteristics of our Universe (e.g., Planck Collaboration et al. 2014; Samushia et al. 2013), there remain a number of observational challenges to the model at the small scales associated with the formation of dwarf galaxies. One of the most pressing issues is the "too big to fail" (TBTF) problem, first identified in the population of bright Milky Way (MW) satellites by Boylan-Kolchin et al. (2011, 2012). In simple terms, the TBTF problem refers to the fact that the observed kinematics of bright MW satellites imply that they are hosted by low-mass dark matter (DM) subhalos. However, a MW-sized halo is expected to have many more such subhalos in λCDM than the number of bright satellites actually orbiting our galaxy.

Several possible solutions to the TBTF problem in the MW context have been put forward, related for example to the uncertainty in the mass of the halo hosting our Galaxy or pointing out the statistical weakness of this "sample of one" challenge (e.g., Wang et al. 2012; Vera-Ciro et al. 2013; Purcell & Zentner 2012). However, subsequent observational results have cast these specific solutions into doubt. In particular, the TBTF problem seems to be present not only in the satellite system of the MW, but also in that of Andromeda (Tollerud et al. 2014). In addition, the TBTF problem does not only concern satellites but

also field dwarf galaxies in the Local Group and Local Volume (Ferrero et al. 2012; Garrison-Kimmel et al. 2014; Brook & Di Cintio 2015; Papastergis et al. 2015). Just as in the case of the bright MW satellites, the observed kinematics of field dwarfs imply that they are hosted by low-mass halos. These halos are produced in large enough numbers in a λCDM Universe, that we would expect to detect significantly more dwarfs than we actually do. In the case of the field, the observational census of dwarfs usually comes from the measurement of the velocity function of galaxies (Zwaan et al. 2010; Papastergis et al. 2011; Klypin et al. 2015). Reliable measurements of the galactic velocity function (VF) can be carried out either using wide area surveys in the 21 cm emission line of atomic hydrogen (HI surveys; Barnes et al. 2001; Giovanelli et al. 2005) or systematic searches of galaxies in the Local Volume (Karachentsev & Kaisina 2013).

Given the universality of the TBTF problem among dwarf galaxies, a solution can be plausible only if it is similarly universal. Perhaps the most promising one is a "baryonic" solution, i.e., related to the effects that baryonic feedback processes have on low-mass halos. First, baryonic feedback can lower the number of halos that are expected to host detectable galaxies, compared to the naive expectation based on cosmological DM-only simulations (e.g., Sawala et al. 2015). The dominant process in this case is reionization feedback, which inhibits the formation of galaxies in the lowest mass halos (Okamoto et al. 2008b). A second important baryonic effect involves the modification of the mass profile of a DM halo by star formation feedback. In particular, a number of studies based on hydrodynamic simulations have observed the creation of a "core" in the central DM density profile of low-mass halos (Mashchenko et al. 2008; Governato et al. 2010; Brooks et al. 2013; Madau et al. 2014; Trujillo-Gomez et al. 2015; Oñorbe et al. 2015, to name a few). This profile is different from the "cuspy" NFW profile observed for halos in DM-only simulations (Navarro & Steinmetz 1997). Theoretically, core creation is attributed to repeated episodes of gas blow-out during bursts of star formation (Pontzen & Governato 2012; Governato et al. 2012). The energetics of star formation makes such that the efficiency of core creation differs among different galaxies, having a characteristic dependence on the stellar-to-halo mass ratio (Di Cintio et al. 2014; Chan et al. 2015) and possibly also on star formation history (Oñorbe et al. 2015). Profile modification can have an important impact on the study of the TBTF problem, because the analysis of dwarf kinematics is dependent on the assumed DM profile.

1.2 Dwarf Galaxies in the Local Group

The Local Group has a physical radius of ∼1.2 Mpc (van den Bergh 1999) and is located at the outskirts of the large Virgo cluster. The actual LG is dominated by three spiral galaxies: M 31(NGC 224, the Andromeda galaxy), the Milky Way (MW), and M 33 (NGC 598, the Triangulum galaxy), in decreasing order of mass. There are no giant or intermediate-mass ellipticals in the LG. The remaining galaxies are dwarf galaxies (DG), and their number has been increasing over the years, since fainter and fainter objects are being discovered (e.g. Crater, Belokurov et al. 2014) out of deep and wide area sky surveys (2MASS, SDSS, etc.). The exact number of DG in the LG is unknown. As of today, they would be ∼100 (McConnachie, 2012). The structure of the LG is shown in Fig. 1.1.

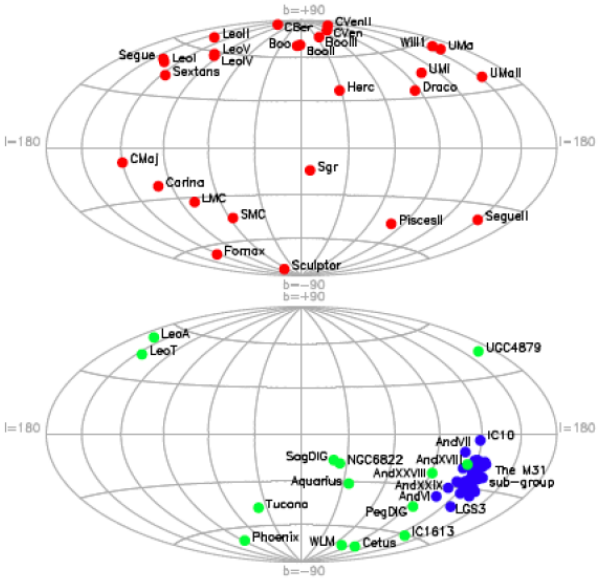

Figure 1.1. Distribution of dwarf galaxies in the LG following McConnachie 2012: The red, blue, and green dots identify the galaxies belonging to the MW sub-group, Andromeda sub-group, and LGC.

The study of the smallest stellar systems in the Universe and, in particular, those which can be resolved into stars, play a major role in understanding how galaxies form and evolve. In this framework, the analysis of the dwarf galaxies of the Local Group (LG) can provide fundamental insights into this subject. Tolstoy et al. (2009) suggest that the term dwarf galaxy should be used to refer to low luminosity galaxies, typically fainter than $M_B \leq -16$ ($M_V \leq -17$) and more spatially extended than globular clusters. This is broadly consistent with the limit of mass at which outflows tend to significantly affect the baryonic mass of a galaxy.

According to van den Bergh et al. (2000), dwarfs in the LG can be divided in three sub-groups:

- the MW sub-group;
- the Andromeda sub-group;
- a third group of dwarf galaxies of mainly irregulars, which appears rather isolated. This last group is called Local Group Cloud (LGC).

Although they were initially considered simple stellar systems, dwarf galaxies show a great variety of SFHs, morphologies, sizes and properties. They can be classified into five main types: Dwarf Elliptical galaxies (dE), Dwarf Spheroidal galaxies (dSph), Dwarf Irregular galaxies (dIrr), Ultra-faint dwarf galaxies (UFD), and Ultra-compact dwarf galaxies (uCd). This diversity has raised an interesting barrage of theories about the possible processes implied in their formation and evolution. For the time being, dSphs galaxies are the dominant type of dwarf galaxies in the LG, although many undiscovered UFD may exist.

Observations reveal striking differences: dIrr are rich in HI and show still ongoing star formation activity, at odds with dSphs whose star formation history appears much more episodic and quiescent during the last Gyrs (Tolstoy 2010). Thus, dIrrs and dSphs are often called late- and early-type galaxies. It is noticeable that dSphs are generally found near (<130 kpc) the two giant galaxies and constitute a system of satellites for these. This is not true for dIrrs whose location appears sparse and at distances larger than 400 kpc from the MW and M31. An exception to the rule are the two irregulars SMC and LMC, which are located at a distance less than 100 kpc from the MW.

Fig. 1.2 shows where different stellar systems in the LG lie if we consider the central surface brightness and the half-light radius as a function of the absolute V magnitude. When the central surface brightness is considered as a function of the absolute V magnitude, it is clear that all dwarf galaxies, despite

of their morphological type, lie in a well defined sequence. This sequence is separated from those of the GGC. These two sequences overlap where the so-called UFDs lie. From this plot it appears that UFDs are the natural extension of the sequence associated to dwarf galaxies. Hence, they should belong to the same class of objects. On the contrary, when we consider the half-light radius as a function of the absolute V magnitude, dwarf galaxies and GGC sequences are well separated. At a first view the UFD sequence appears separated from that of the dwarf galaxies. However, this might be due to the errors in the measurement of the size of these systems, which is particularly difficult because of their low luminosity.

Due to their very low luminosity dwarf galaxies are really arduous to detect. However, with the advent of new techniques of deep field imaging recently it has been possible to identify an increasingly large number of dwarfs (McConnachie 2012; Belokurov et al. 2007). On the other hand, it remains a challenge to detect dwarf members of external groups of galaxies. The census of dwarf galaxies belonging to the LG is still growing as new instruments are developed, and, consequently, extremely faint objects are continuously identified (Koposov et al. 2015a).

Because of their low masses, dwarfs are recognized as relatively fragile systems. Present day dwarfs have been strongly influenced by both external processes (e.g., tidal effects, ram pressure, intense ultra-violet radiation from the epoch of cosmic reionization, star formation in nearby massive galaxies) and internal mechanisms (e.g., star formation, stellar feedback from supernovae, galactic scale winds, turbulence). These processes have re-shaped their dark and baryonic components throughout the galaxies' lifetimes (e.g., Dekel & Silk 1986; Efstathiou 1992; Mac Low & Ferrara 1999; Bullock et al. 2000; Mayer et al. 2001; Governato et al. 2010; Brooks et al. 2013; Kazantzidis et al. 2013). Disentangling the relative contribution of each physical process is key to understanding a wide range of astrophysics including star formation in extremely low metallicity environments, galaxy morphological transformations, the coupling of dark and baryonic matter, the mechanisms by which galaxies' gas supplies are depleted, interactions between host and satellite systems, and the mass assembly history of the LG, all of which have broader implications for how galaxies and groups of galaxies evolve.

At present, all known dwarf galaxies in the LG have been observed with space- and/or ground-based imaging. These data reveal the galaxies' resolved stellar populations (e.g., Hodge 1989; Mateo 1998; Martin et al. 2008b; Tolstoy et al. 2009; McConnachie 2012; Brown et al. 2012; Belokurov 2013; Martin et al. 2013 and references therein), allowing us to infer their stellar age distributions.

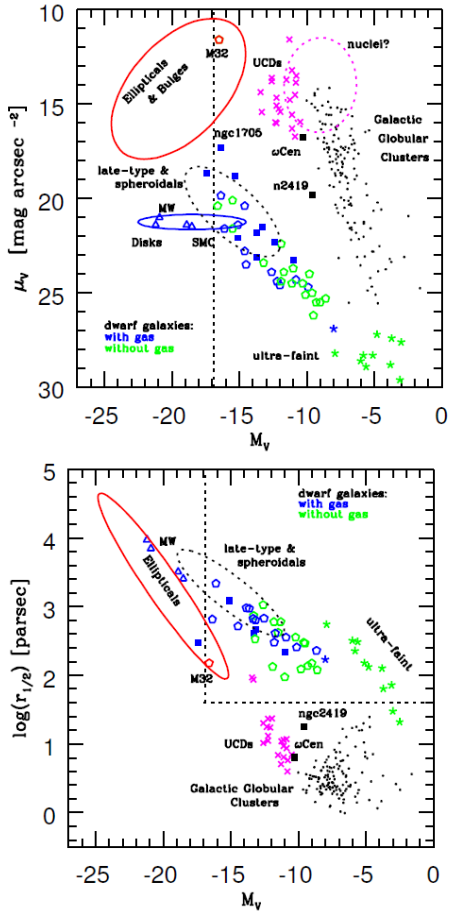

Figure 1.2. Figure from Tolstoy et al. (2009). Dotted lines indicate the classical limits of the dwarf galaxy class as defined by Tammann (1994). The central surface brightness, μ_V as a function of the absolute magnitude, M_V, and the half light radius, $r_{1/2}$, as a function of the absolute magnitude, M_V are shown respectively in the upper and lower panel. Marked with colored ellipses are the typical locations of Elliptical galaxies & bulges (red), spiral galaxy disks (blue), galactic nuclei (dashed magenta) and large early (spheroidals) and late-type systems (dashed black). GGCs are plotted individually as small black points. M 31, the Milky Way (MW), M 33 and LMC are shown as blue open triangles. LG dwarf galaxies are plotted as open pentagons, blue for systems with gas and green for systems without gas. The recently discovered UFDs are given star symbols, and the same color code. Blue- and ultra-compact dwarfs are marked respectively as blue solid squares and as magenta crosses. For references and a complete discussion see Tolstoy et al. (2009).

The colors and luminosities of individual stars can be directly compared to stellar evolution models, yielding the galaxy's star formation rate (SFR) as a function of lookback time and metallicity, i.e., a star formation history (SFH).

1.3 Ultra Faint Dwarf Galaxies

The very faint lowest-mass ($L < 10^5 L_\odot$ and $10^2 M_\odot < M_* < 10^5 M_\odot, z = 0$) and most metal-poor ([Fe/H] < -2) dwarfs of the Local Group, known as ultrafaint dwarfs (UFDs), have been proposed as possible descendants of the dwarf galaxies at high redshift and are thus the best place to look for the metal-poor stars that hold clues to the nature of the first generation of stars. Studying such systems enables an approach often termed "galactic archaeology", wherein local galaxies are used as fossil records of the early assembly history of the Milky Way (e.g., Salvadori & Ferrara 2009; Frebel et al. 2010; Boylan-Kolchin et al. 2015; Ricotti et al. 2016; Lapi et al. 2017; Weisz & Boylan-Kolchin 2017).

Concurrent with searches for faint galaxies at high redshifts, there has been a renaissance in the discovery of extremely faint, lowmass galaxies in the Local Group (e.g. Willman et al. 2005; Belokurov et al. 2006; Zucker et al. 2006; Irwin et al. 2007; Koposov et al. 2007; Bechtol et al. 2015; Kim & Jerjen 2015; Koposov et al. 2015b; Laevens et al. 2015a; Martin et al. 2015). Deep, wide-field photometric surveys (e.g. Sloan Digital Sky Survey, Dark Energy Survey) have identified dozens of faint galaxies surrounding the Milky Way with luminosities as low as $M_V \sim -2$ ($M_* \sim 10^2 M_\odot$), and these detections likely represent only a fraction of the low-mass galaxy population in the LG owing to various observational biases (e.g. Koposov et al. 2008; Tollerud et al. 2008; Walsh et al. 2009).

As shown in Fig. 1.2, UFDs appear to be the natural extension of the dSph, but for the faintest of them the properties are very similar to that of GGC, with the distinction of the presence of dark matter. UFD kinematics are clearly dark-matter-dominated, with M/L_V >100 (e.g., Kleyna et al. 2005; Simon & Geha 2007; Muñoz et al. 2006), even where velocity dispersions have been revised downward (e.g., Koposov et al. 2011). As the dSph these systems are mainly dominated by an old population and they do not show any sign of ongoing star formation. The CMD analysis of UFDs is particularly arduous, because of Galactic contamination.

Many UFDs show a high ellipticity, which can be possibly ascribed to tidal disruption by the MW. Fundamental evidence comes from stellar kinematics of the single stars in UFDs (Tolstoy et al. 2009). Simon & Geha (2007) showed that these systems are more DM dominated than all the other systems known,

with mass-to-light ratio between 140 and 1700 $M_{\odot}/L_{\odot}$. Their metallicities are lower than those found in classical dSphs, with a scatter higher than that of GGC (Kirby et al., 2013). Figure 1.3 show the luminosity-metallicity relation (LZR) and the mass-metallicity relation (MZR) obtened by Kirby et al. 2013 for Local Group dwarf galaxies.

These UFDs host predominantly ancient (>10 Gyr), extremely metal poor ([Fe/H] < -2) stellar populations (e.g. Frebel & Norris 2015). They are thus consistent with being 'fossils of reionization' (e.g. Ricotti & Gnedin 2005; Okamoto et al. 2012; Brown et al. 2014; Weisz et al. 2014b): UFDs were star-forming galaxies in the early Universe until UV radiation from reionization stunted their formation (e.g. Bovill & Ricotti 2009).

1.4 The Star Formation History of Dwarf Galaxies

The study of the SFH of resolved stellar populations was first initiated by Baade in the 1940s. The derivations of the SFH is based on the study of color-magnitude diagrams (CMD), accompanied by highly reliable stellar evolutionary models (e.g. Pietrinferni et al. 2004; Girardi et al. 2000). Stars at different evolutionary stages occupy different regions of the diagram.

A fundamental assumption in this method is that all the stars belonging to the same system have within the errors the same distance and the same reddening. The CMDs of stellar systems allow the detailed study of stellar populations, which means collecting details about the age, metal content, and initial mass function (IMF) of a given system. In the last decades the introduction of new technologies, as CCDs, and space-based telescopes, as the HST, have significantly improved the power of the study of resolved stellar populations using CMDs (e.g. Hidalgo et al. 2013; Weisz et al. 2014a). Moreover, due to the improvement in computational power, the comparison of an observed CMD to a synthetic CMD has been introduced. A number of codes able to perform this comparison have been developed in the last years (Tolstoy et al. 2009; Hidalgo et al. 2011).

The synthetic CMD is created by selecting a library of evolutionary models, and assuming an IMF, a binary fraction, and a distribution in age and metallicity. Then the accurate simulation of photometric errors, through artificial star tests, is used to reproduce the observational effects on the synthetic CMD. A full description of the method is given in Appendix D.

The dwarf galaxy satellites of the MW exhibit a great diversity in stellar age, metallicity, and sizes, indicating that they have experienced different star formation histories (SFHs). Specifically, more massive dwarfs ($M_* > 10^6 M_{\odot}, z = 0$)

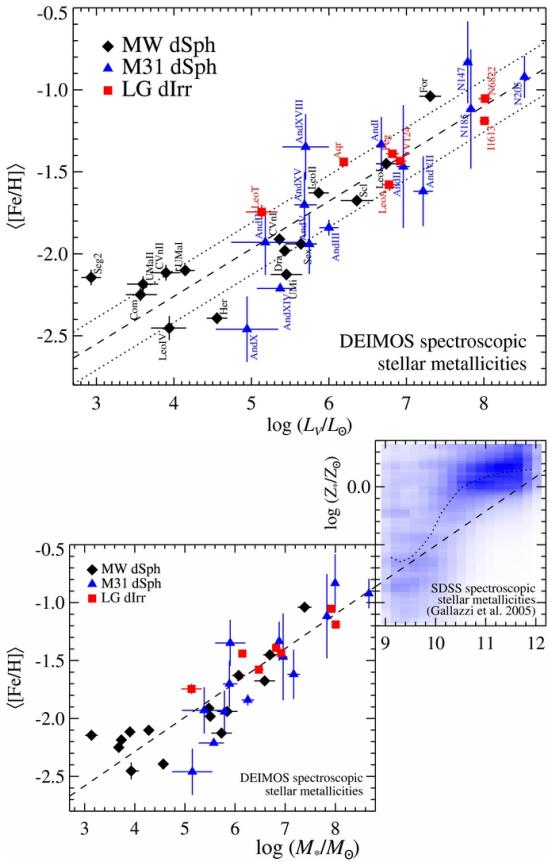

Figure 1.3. Figure from Kirby et al. 2013. *Top panel:* Luminosity–stellar metallicity relation for Local Group dwarf galaxies. The black diamonds (MW dSphs) and red squares (dIrrs) are the average stellar iron abundances from spectroscopy of individual stars. The blue triangles (M31 dSphs) are the average stellar iron abundances from coadded spectroscopy of groups of similar stars within each dwarf galaxy. The dashed line shows the least-squares line, where the intercept is calculated at $10^6 L_\odot$), excluding the M31 data points and Segue 2, which may be a heavily tidally stripped galaxy (Kirby et al., 2013). The dotted line shows the rms about the best fit. *Bottom panel:* Stellar mass–stellar metallicity relation for Local Group dwarf galaxies (left) and more massive SDSS galaxies (right, Gallazzi et al. 2005). The Local Group metallicities ($< [Fe/H] >$) were measured from iron lines, and the SDSS metallicities ($\log Z_*$) were measured from a combination of absorption lines, mostly Mg and Fe. The conversion between $< [Fe/H] >$ and $\log Z_*$ depends on [Mg/Fe]. The Local Group data is the same as in the top panel. The dashed line is the least-squares fit to the Local Group galaxies, where the intercept is calculated at $10^6 M_\odot$), and the dotted line in the right panel is the moving median for the SDSS galaxies.

are characterized by extended SFHs and show large metallicity spreads, whereas the lower-mass UFDs appear to have experienced a truncated SFH, yielding uniformly ancient stellar populations, older than $\sim$ 11-12 Gyr (e.g., Bullock et al. 2000; Grebel & Gallagher 2004; Brown et al. 2012, 2014; Weisz et al. 2014b).

A plausible mechanism responsible for such early suppression of star formation in UFDs could be reionization, referring to the global phase transition from a neutral universe to an ionized one at z = 10 - 6 (Planck Collaboration et al. 2016). During this period of time, the radiation from stars heated the gas in the interstellar medium (ISM) and intergalactic medium (IGM), thus boosting the Jeans mass, i.e., the minimum mass to trigger gravitational instability, which in turn made it difficult for gas to collapse into halos (see, e.g., Tolstoy et al. 2009, for a review; see also Gnedin & Kravtsov 2006; Bovill & Ricotti 2009, 2011; Brown et al. 2012).

Ricotti & Gnedin (2005) classify dwarf galaxies based on their SFHs into three categories: galaxies in which the bulk of stars were formed prior to reionization are classified as "true fossils", whereas "polluted fossils" refer to galaxies that have continuously formed stars beyond reionization, and "survivors" mean galaxies that formed the majority of their stars after reionization. By following the evolution of the first galaxies until the present, we will be able to establish the expected degree of "pollution" in UFDs and furthermore quantify the significance of late-time accretion events to their present-day chemical properties. True fossils, in particular, could offer more stringent insight on the nature of the first generation of stars, preserving their chemical signatures since these galaxies are not likely to undergo significant star formation after reionization. UFDs were star-forming galaxies in the early Universe until UV radiation from reionization stunted their formation (e.g. Bovill & Ricotti 2009).

1.5 Thesis aims

In this thesis our aim is to obtain a homogeneous study of the star formation history of three UFDs of the Local Group: Boötes I, Canes Venatici II and Leo IV. The data come from ground-based (Subaru) in the case of Boötes I and from space (HST) in the case of the other two dwarfs. The main tools will be the color-magnitude diagrams (CMD) in combination with a set of codes developed by our group: IAC-star (Aparicio & Gallart, 2004), IAC-pop (Aparicio & Hidalgo, 2009), and MinnIAC (Hidalgo et al., 2011).

Through the analysis of the SFH we want to try to understand the effect of several physical processes in the formation and evolution of dwarf galaxies, such as the reionization, feedback by supernovas or tidal interactions. To understand

the importance that these processes have in the formation of dwarf galaxies is essential to know how massive galaxies (e.g. the Milky Way) are formed.

Specifically, we can cite the following objectives:

- Obtaining deep CMD reaching the oldest main sequence turn-off (oMSTO) of a set of UFDs.
- Obtaining a detailed SFH up to the oldest ages for all the galaxies named before.
- In the case of Canes Venatici II, looking for traces of multipopulations in this galaxy in order to shed light on the possible link between ultra-faint dwarfs and Galactic Globular Clusters (GGCs).
- Analyze whether the quenching of the star formation in these galaxies is concurrent with the end of the Epoch of Reionization (EoR).
- Determine whether these galaxies are "true fossils", "polluted fossils" or "survivors" of the EoR.

The thesis is structured as follows. In Chapter 2 is given a description of the ESPIGA project. Chapter **??** describes the results obtained with data from the Isaac Newton Telescope (INT) for Segue II. In the three upcoming chapters, 3, 4, 5, are described the stellar population analysis and the SFH of each dwarf. In Chapter 6 we analyze some global features of Boötes I, Canes Venatici II and Leo IV. Finally, in Chapter 7 the conclusions are given.

2

The ESPIGA Project

In this chapter we will describe the ESPIGA project, the data we have collected from the different telescopes and the process of analysis that leads to obtaining the final scientific images.

2.1 ESPIGA: Early Stellar Populations In GAlaxies

ESPIGA(Early Stellar Populations In GAlaxies) is a project focused on to derive homogeneously accurate star formation histories of all resolved galaxies of the Local Group within $\sim$ 250 Kpc of distance. The aim is to obtain deep CMDs reaching the oldest main sequence turn-off (oMSTO) with good accuracy to derive the SFH up to the oldest ages. The ESPIGA project will analyze homogeneously all the galaxies (about 23, see Table 2.1) for which the oMSTO can be observed from ground-based telescopes (e.g. INT or Subaru in the North, and Clay or Blanco telescopes in the South). The observations will be made using broadband filters (SLOAN *ugri*, Johnson-Cousins *UBVRI* and ACS@HST filters). It has been demonstrated that the use of a combination of different filters is very effective for identifying multiple sequences along the red giant branch (RGB). Using the photometric index (U-B)-(B-I), (Monelli et al., 2013) have found multimodal RGBs in Globular Clusters (GCs) with the present of two or more components, not detected using other filters. This might be connected with different abundances of light elements (O, Na, C, N, and Al). For the ESPIGA project, we expect that the use of similar combination of *ugri* filters or equivalent combination in other photometric systems will show, if exist, multimodal RGBs. This analysis combined with the new set of stellar evolution models (BaSTI) will favor the interpretation of the results.

If the photometry is accurate at the oMSTO, the age and metallicity of the ever formed stars can be obtained for the entire life of a galaxy with an age precision of $\leq$ 1 Gyr for the oldest stellar populations (Aparicio & Hidalgo, 2009; Hidalgo et al., 2011). This method is based on the comparison of the observed CMDs with synthetic CMDs. Members of our team have developed a suite of software: IAC-star (Aparicio & Gallart, 2004), IAC-pop (Aparicio & Hidalgo, 2009), and MinnIAC (Hidalgo et al., 2011) which have been proven in retrieving a detailed SFH of LG dwarf galaxies. Specifically our methodological approach has been applied to ACS@HST data of six galaxies (Cetus, Tucana, LGS-3, Phoenix, Leo-A, and IC1613) in order to trace the possible effects of the physical mechanisms on the star formation and evolution of LG dwarf galaxies (Hidalgo et al. 2009, Hidalgo et al. 2011, Monelli et al. 2010a, 2010b).

This project is willing to address the following subjects:

- the effects of cosmic and local processes in the formation and evolution of the dwarf galaxies of the LG;
- whether all dwarf galaxies had a common ancestor, despite their different morphological types;
- the role of the Milky Way in shaping their structure.

Particularly, this thesis is focused on those galaxies of the sample that can be observed with the Isaac Newton Telescope (INT), on Boötes I observed with the Subaru Telescope and on Canes Venatici II and Leo IV observed with the Hubble Space Telescope (HST).

2.2 The Data

A sub-sample of 8 galaxies of the ESPIGA project was observed with the Wide Field Camera (WFC) of the Isaac Newton Telescope (INT) using deep broad-band *ugri* photometry. In 2013, this project was granted with two nights to observe Segue II and Ursa Major II (scheduled for September and January). In 2014 we obtained time to observe the rest of the sub-sample (four nights scheduled for February and two nights scheduled for March).

We used i, g and r Sloan Gunn filters, whereas for the case of u photometry we used the RGO U filter, which is quite similar to the u sloan filter (WFC@INT has not u filter). Our observations will be complemented by INT archivial data, whenever they are available. Table 2.2 lists the eight galaxies proposed to be observed at WFC@INT. Except for Boötes I and Boötes III, the integration time (in seconds) allow us to reach the oMSTO in all bands.

Galaxy	$(m-M)_0$	Data
Segue I	16.8	INT
Ursa Major II	17.5	INT
Segue II	17.7	INT
Willman 1	17.9	INT
Boötes II	18.1	INT
Coma Berenices	18.2	INT
Boötes III	18.3	INT
Boötes I	19.1	INT/Subaru
Draco	19.4	Subaru
Ursa Minor	19.4	Subaru
Sculptor	19.7	Blanco/Clay
Sextans I	19.6	Subaru
Ursa Major I	19.9	Subaru
Carina	20.1	Blanco/Clay
Hercules	20.6	Subaru
Fornax	20.8	Blanco/Clay
Leo IV	20.9	HST
Canes Venatici II	21.0	HST
Leo V	21.2	Subaru
Pisces II	21.3	Subaru
Canes Venatici I	21.6	Subaru
Leo II	21.8	Subaru
Leo I	22.0	Subaru

Table 2.1. Full ESPIGA galaxy sample. Columns 2: Distance modulus, 3: Telescope used or requested.

Regarding Boötes I, Canes Venatici II and Leo IV, Table 2.3 and Table 2.4 show the integration times (in seconds) for each filter of Boötes I and HST data respectively.

Galaxy	RA (hhmmss)	Dec (^{o} ' ")	U	g	r	i
Segue I	10 07 04	+16 04 55	920	3240	3450	1410
Ursa Major II	08 51 30	+63 07 48	3080	3130	4330	8330
Segue II	02 19 16	+20 10 31	2640	2650	3310	7020
Willman 1	10 49 21	+51 03 00	2920	2450	15145	11330
Boötes II	13 58 00	+12 51 00	2700	8050	5540	15530
Coma Berenices	12 26 59	+23 54 15	5480	5000	6600	14830
Boötes III	13 57 12	+26 48 00	210	100	100	100
Boötes I	14 00 06	+14 30 00	210	100	100	100

Table 2.2. Summary of the observations and archive INT data. We give the galaxy name, coordinates and the integration times (in seconds) for each filter.

Filter	Short Exposure		Long Exposure	
	s×shots	FWHM	s×shots	FWHM
I	10.0 s ×3	0".94	200.0 s × 15	0".90
V	10.0 s ×3	0".98	120.0 s × 5	1".00

Table 2.3. Log of the observations of Boötes I (Subaru).

Galaxy	RA (hhmmss)	Dec (^{o} ' ")	F606W	F814W
Canes Venatici II	12 57 10	+34 19 15	20860	20860
Leo IV	11 32 57	-00 32 00	20540	20540

Table 2.4. Summary of CvnII and LeoIV data(HST). We give the galaxy name and the integration times (in seconds) for each filter.

2.3 Pre-reduction and PSF Photometry

Due to strong sky background and instrumental noises/effects, we often need to take a few steps to remove these unwanted signals in the raw data to generate

images that are suitable for doing science. While nowadays most telescopes have their own automated pipelines to reduce raw images, it is still very useful to know its basic concepts.

In Appendix B are described the details of data reduction to obtain scientific images with IRAF. The INT data have been reduced following this process, whereas the Subaru and HST data are delivered calibrated.

After obtaining scientific images, the following step is to obtain the photometry. When doing photometry on crowded star fields, such as globular clusters or open clusters, aperture photometry will not yield reliable results. It is better to use a Point Spread Function: a gaussian that can be fitted to all of the stars in the field in order to find their magnitudes. The datails to obtain photometry are described in Appendix C. The photometry of INT and Subaru data has been done using DAOPHOT (Stetson, 1987) and its companion packages ALLSTAR and ALLFRAME (Stetson, 1994) (see Section C.2). Instead in the case of HST data the photometry was obtained using DOLPHOT (Dolphin, 2000) (see Section C.3).

2.4 Photometric Calibration of Data

Photometric calibration is fundamental for converting instrumental magnitudes to calibrated apparent magnitudes in a standard system. If the science goal requires a calibrated measurement of a flux or surface brightness, then you must observe photometric standard stars. There is no other way to convert your instrumental counts to a physically meaningful scale. The effects that photometric calibration must remove are atmospheric extinction and the mismatch between the instrumental and standard systems. The user have to define the transformation between the instrumental and standard system for the standard stars and apply this transformation to calibrate the instrumental magnitudes of the programme objects into the standard system. In general, the calibration equation can be written as

$$M_{1,2} = m_{1,2} + Z_{1,2} + C_{1,2}(M_1 - M_2) \tag{2.1}$$

where 1 and 2 denote the filter, *uppercase letters* are calibrated magnitudes and *lowercase letters* represent instrumental magnitudes corrected for time exposition and extinction. C shows the color coeffcient and Z is the zero-point.

There are many catalogues of photometric standard stars. These standard stars have a known brightness in your target photometric system. For the UBVRI filter system, the "standard" lists of standards are those devised by Arlo Landolt. A list of fainter standards with V magnitudes between 8.9 and 16.3,

and the color index range $-0.35 < (B - V) < +2.30$ is published in Landolt (2009). For the *u'g'r'i'z'* filter system (see Fukugita et al., 1996), the standard-star network was developed at the US Naval Observatory (USNO), Flagstaff Station (Smith et al., 2002). These stars form the basis for the photometric calibration of the Sloan Digital Sky Survey (SDSS). In the case of INT data, the photometric observations were carried out in the *g'r'i'* Sloan filters and in U Johnson-Cousins filter. For the case of Subaru the photometric observations were carried out in the V and I Johnson-Cousins filters, whereas for the HST they were in *F606W* and *F814W* filters.

The desirable properties for a set of standard stars include the following:

- a range of zenith distances (and hence air masses) similar to, but slightly larger than, those of the programme objects. Also the range in air mass should be at least 1.0. A reasonable upper limit to the air mass for observing standards is about 2.5 (though this will depend on the site),
- a range of celestial coordinates similar to those of the programme objects (this criterion is, of course, related to the previous one),
- a range of colors and magnitudes which are similar to (or slightly larger than) those of the programme objects.

Five standard star fields were observed throughout the observational campaign. These are: G163, SA97, SA98, SA101 and SA105.

2.4.1 Process to obtain calibrate magnitudes

The first step is implement the pre-reduction process described in Appendix B to the images of standard stars. Then the instrumental magnitudes are measured for these stars by using aperture photometry. This consists in the sum of the counts within a circle centered around the star (see Section C.1) and radius equal to 25 (generally equal to 3 times the Full Width Half Maximum). The instrumental magnitudes are

$$m_{instr} = m_{ap} + 2.5 \log(t_{exp}) \tag{2.2}$$

where t_{exp} represents the time exposure.

After derivation of instrumental magnitudes of standard stars, extinction coefficients are calculated as following: a least-squares linear fit is performed to the equation $\Delta m = K \times \chi$; where $\Delta m = m - M$ is the difference between the instrumental and calibrated magnitudes of standard stars and χ is the airmass. The linear fit provides the extinction coefficient K, for each filter.

After correcting the instrumental magnitudes for extinction, Eq. 2.1 is used to obtain the photometric zero points (Z) and the color coefficient (C). These coefficients where applied to the observations.

2.5 The INT data: Segue II

From INT data, only Segue II shows quality images to obtain a deep CMD. For other galaxies this has not been possible due to the bad seeing (> 1.5 arcsec) during the nights of observations.

Segue II, was initially identified by Belokurov et al. (2009) as a stellar overdensity on the sky in images obtained as part of the Sloan Extension for Galactic Understanding and Exploration (SEGUE) and by using matched filters in color–magnitude space. Deeper imaging and followup spectroscopy confirmed this detection, identified the presence of a cold velocity structure with a non-zero velocity dispersion, and indicated a mean metallicity of approximately 1/100th solar. They found that Segue II has a luminosity of $M_V = -2.5$ (900 $L_\odot$). From the individual radial velocities of five red giants, they measured a velocity dispersion of $3.4^{+2.5}_{-1.2}$ km s^{-1}. The expected velocity dispersion in the absence of dark matter is 0.5 km s^{-1}.

Kirby et al. (2013) used the DEIMOS spectrograph to obtain red and near-infrared spectra of 25 probable members of Segue II. They confirmed that stars in Segue II span a range in metallicity of more than 1.5 dex. The [α/Fe] ratios in Segue II generally decrease with increasing [Fe/H], as seen in classical dwarf galaxies (e.g. Shetrone et al. 2003; Kirby et al. 2011) but not all of the ultra-faint dwarf galaxies (Frebel et al. 2010; Vargas et al. 2013). Segue II is the least-massive galaxy currently known based on its inferred dynamical mass. Yet with a mean metallicity of $[Fe/H] = -2.2$ it does not obey the mass-metallicity relationship established by Kirby et al. (2011) for classical and ultra-faint dwarf galaxies. Segue II, along with Segue I and Willman 1, may reveal the existence of a metallicity floor in galaxy formation. Alternatively, Segue II may have been substantially more massive before being tidally stripped down – by a factor of several hundred in stellar mass - to the remnant observed today.

To summarize, the fundamental parameters of Segue II are listed in Table 2.5.

2.6 Dataset

The data of Segue II was obtained with the Wide Field Camera (WFC) of the Isaac Newton Telescope (INT) during the nights of September 2013 and

Parameter	Value	References[a]
RA (hhmmss)	02 19 16	(1)
Dec (^{o} ' ")	+20 10 31	(1)
Galactic longitude, l	149.4^o	(1)
Galactic latitude, b	-38.1^o	(1)
Position angle	$182^o \pm 17^o$	(1)
Ellipticity ϵ	0.15±0.10	(1)
E(B - V)	0.185	(1)
$(m-M)_0$	17.70±0.10	(1)
Heliocentric distance (kpc)	35±2	(1)
Heliocentric velocity (km s^{-1})	-39.2±2.5	(1)
Apparent magnitude V	15.2±0.3	(1)
Half-light radius r_h (pc)	35±3	(1)
Absolute magnitude M_V	-2.5±0.3	(1)
Half-light radius r_h (arcmin)	3.40±0.20	(1)
Barionic mass $M_\star$ ($10^6 M_\odot$)	0.00086	(1)
$[Fe/H]$	-2.00±0.25	(1)

[a] References: (1) Belokurov et al., 2009.
Notes. The baryonic mass is computed from the integrated V-band luminosity and assumes $M_\odot/L_\odot = 1$.

Table 2.5. Fundamental parameters of Segue II.

January 2014. We used i, g and r Sloan Gunn filters, whereas for the case of u photometry we used the RGO U filter, which is quite similar to the u sloan filter (WFC@INT has not u filter). The field of view of WFC is 34 ×34 arcmin. Table 2.2 shows the coordinates and the integration time (in seconds) for each filter for Segue II.

2.7 Calibration

The images of Segue II have been reduced following the process described in Appendix B. After obtaining scientific images, the following step is to obtain the photometry. The photometry of Segue II has been done using DAOPHOT (Stetson, 1987) and its companion packages ALLSTAR and ALLFRAME (Stetson, 1994) (see Section C.2).

During the observational campaign we have observed five standard star fields to perform the photometric calibration. These are: G163, SA97, SA98, SA101 and SA105. To obtain the calibrated magnitudes of Segue II we have used the *u'g'r'i'z'* standard-star network developed by Smith et al. 2002 and the Equations 2.1 and 2.2 described in Section 2.4. The values that we have obtained for each filters are summarize in Table 2.6.

Filter	Extinction coefficient (K)	Zero point (Z)	color term (C)
g	0.205 ± 0.049	0.825 ± 0.004	0.049 ± 0.005
r	0.078 ± 0.032	0.430 ± 0.004	-0.023 ± 0.007
i	0.044 ± 0.017	0.033 ± 0.002	0.017 ± 0.007
U	0.474 ± 0.079	-0.700 ± 0.027	0.053 ± 0.013

Table 2.6. Parameters to calculate calibrated magnitudes in each filter. Columns 2: Extinction coefficient (K), 3: Zero point (ZP), 4: Color term (C).

2.8 CMD of Segue II

The CMD show the relation between the absolute magnitudes (brightnesses) of stars and their colors, which are closely related to their temperatures and spectral types. The calibrated CMDs of Segue II in different filters combination are shown in Fig. 2.1. Only objects with $\sigma \leq 0.1$, $chi \leq 1.2$ and $|sharp| \leq 0.25$ were considered stars. A distance modulus of $(m - M)_0 = 17.7$ mag has been used (Belokurov et al., 2009). The main features of the CMD like TO, RGB and

HB are not well defined in both the diagram of Fig. 2.1 and this makes difficult to study the stellar populations in Segue II. The total number of stars in the g-r versus r diagram is 1258 stars, while it is of 836 stars in the r-i versus i diagram. Anyway a comparison with theoretical isochrones belong to the BaSTI library (Pietrinferni et al., 2004) is shown in 2.1. Two isochrones of metallicity Z=0.0001 (corrisponding to [Fe/H]= -2.28) are overlapped: 13.5 Gyr (red) and 11 Gyr (blue). The metallicity selected for the isochrones was chosen based on the results of the photometric and spectroscopic studies presented by Belokurov et al. (2009) which suggest that the metallicity of Segue II is [Fe/H]$\sim$ -2. The preliminary results obtained by the comparison with the isochrones show that the MS TO are well reproduced by the oldest isochrone. This is indicative of the evidence of a very old and metal poor population in Segue II.

To derive the SFH up to the oldest ages is necessary to obtain deep CMDs reaching the oMSTO with good accuracy and this is unfortunately not the case of Segue II.

For this reason we have decided not to perform the SFH for Segue II and to use a new set of data from the Subaru Telescope and from the public archive of the Hubble Space Telescope. In particular, the following ultra-faint dwarf galaxies will be analyzed: Boötes I (Subaru), Canes Venatici II and Leo IV (Hubble). The analysis of these data will be discussed respectively in chapters 3, 4 and 5.

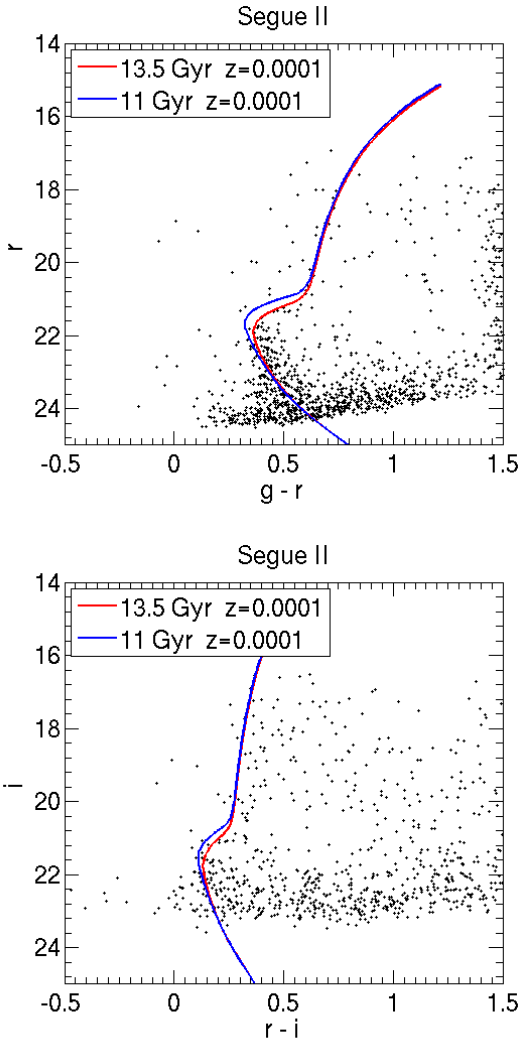

Figure 2.1. Color-magnitude diagrams of Segue II (*Top panel: g-r* versus r diagram; *Bottom panel: r-i* versus i diagram). A distance modulus of $(m-M)_0 = 17.7$ mag has been used (Belokurov et al., 2009). Two isochrones of metallicity Z=0.0001 from the BaSTI library (Pietrinferni et al., 2004) are overlapped: 13.5 Gyr (red) and 11 Gyr (blue). The oldest isochrone shows evidence of a very old population in Segue II.

3

Boötes I

In this chapter we will focus on the analysis of the ultra-faint dwarf galaxy Boötes I. The data comes from Suprime-Cam at the Subaru Telescope. The calibration of the data, the resulting CMD and the estimate of age and metallicity using isochrone fitting are discussed in Sections 3.3 and 3.4. Hence, the SFH and the stellar populations in Boötes I are considered in Sections 3.6 and 3.7.

3.1 Introduction

Boötes I was one of the first new dwarf spheroidal galaxies (dSphs) discovered using the SDSS photometric survey, by Belokurov et al. (2006). Since its recent discovery the Boötes I ultrafaint dwarf spheroidal galaxy (UFD) has been the subject of a number of investigations, aiming at providing insight into the formation and evolution of this system. Boötes I has a number of interesting properties, but seems representative of the group of newly discovered intrinsically faint dSph galaxies which are (reasonably) far from the Galactic center. Located at 66 ± 2 kpc distance from the Sun and with an absolute visual magnitude of $M_V = -6.3 \pm 0.2$ mag (McConnachie, 2012), Boötes I is one of the brightest UFDs found lurking around the Milky Way, and one of its closest satellites. It is a metal-poor ([Fe/H] $= -2.59 \pm 0.43$; Lai et al., 2011) system, and is one of the most gas-poor dwarfs known (Bailin & Ford, 2007). Whichever mechanisms are responsible for gas removal from Boötes I, the absence of gas streams or outflowing gas suggests that they have completed long ago. It shows an elongated stellar distribution (Belokurov et al. 2006; Okamoto et al. 2012), which indicates that it is undergoing tidal disruption, and has a high mass-to-light ratio (>100; Muñoz et al. 2006; Martin et al. 2007; Koposov et al. 2011).

Results from N-body simulations, using a number of models of Boötes I, have led to the conclusion that its progenitor must have been dark matter-dominated, since a purely baryonic star cluster could not reproduce the observed velocity dispersion (Fellhauer et al. 2008). However, more recent work by Koposov et al. (2011) has demonstrated that Boötes I has two kinematically distinct stellar components: a dominant, 'cold' component, that encompasses 70 per cent of the member stars and has a low projected radial velocity dispersion of $2.4^{+0.9}_{-0.5}$ km s^{-1}, and a minority, 'hot' component, that encompasses 30 per cent of the member stars and has a projected radial velocity dispersion of about 9 km s^{-1}. They speculate that this may arise from the velocity anisotropy of the stellar population. Study of the stellar population of Boötes I has shown it to be old (>13 Gyr; Okamoto et al. 2012), and consistent with a single epoch, short period burst of star formation (Belokurov et al. 2006; Okamoto et al. 2012). Boötes I has a population of variable stars (Dall'Ora et al. 2006; Siegel 2006), and blue straggler stars (BSS; Santana et al. 2013), and shows chemical properties consistent with essentially primordial initial abundances (Gilmore et al. 2013).

To summarize, the fundamental parameters of Boötes I are listed in Table 3.1.

3.2 Dataset

The Subaru/Suprimecam data of Boötes I come from the SMOKA science archive, which archives the public data of the Subaru Telescope. We retrieved the deep V and I imaging observed by Okamoto and collaborators during the night of 2008 April 5 (PI: S. Okamoto; Proposal ID: S08A-022). The field of view of all the Subaru images is $34' \times 27'$, which allows to cover a significant fraction of the galaxy (see Fig. 3.1). To avoid saturation of bright stars, they took short and long exposure images. The combination of short and long exposures allowed to construct CMDs from the bright red giant branch (RGB) to below the old MSTO. The seeing, the number of images and the exposure time of each image are listed in Table 2.3.

The images of Boötes I are delivered calibrated therefore, in this case, there was no need to apply the pre-reduction process described in the Appendix B, whereas the PSF photometry has been obtained with DAOPHOT (see Section C.2).

Parameter	Value	References[a]
RA (hhmmss)	14 00 06	(1)
Dec (^{o} ' ")	+14 30 00	(1)
Galactic longitude, l	358.1^o	(1)
Galactic latitude, b	69.6^o	(1)
Position angle	$14^o \pm 6^o$	(5)
Ellipticity ϵ	0.39±0.06	(5)
E(B - V)	0.017	(2)
$(m-M)_0$	19.11±0.08	(3)
Heliocentric distance (kpc)	66±2	(3)
Heliocentric velocity (km s^{-1})	99.0±2.1	(4)
Apparent magnitude V	12.8±0.2	(5)
Half-light radius r_h (pc)	242±21	(5)
Absolute magnitude M_V	-6.3±0.2	(5)
Half-light radius r_h (arcmin)	12.60±1.00	(5)
Barionic mass $M_\star$ ($10^6 M_\odot$)	0.029	(2)
$[Fe/H]$	-2.59±0.43	(6)

[a] References: (1) Belokurov et al., 2006; (2) McConnachie, 2012; (3) Dall'Ora et al., 2006; (4) Martin et al., 2007; (5) Martin et al., 2008a; (6) Lai et al., 2011.

Notes. The baryonic mass is computed from the integrated V-band luminosity and assumes $M_\odot/L_\odot = 1$.

Table 3.1. Fundamental parameters of Boötes I.

Figure 3.1. An image of Boötes I with a field of view of Subaru/Suprime-Cam ($34' \times 27'$). The ellipse is centered in the galaxy and has the measured ellipticity.

3.3 Calibration

The first step in the analysis is to calibrate the instrumental magnitudes obtained by the photometry to a standard photometric system. In the case of Boötes I, the photometric observations were carried out in the Johnson-Cousins filters.

To calibrate Boötes I we used standard fields observed with IAC80, the 82 cm Ritchey-Chretien Cassegrain telescope, located at the Teide Observatory in Tenerife. The telescope is equipped with CAMELOT[1] (Zurita, 2011), a wide field camera with 2048×2048 pixels of 13.5×13.5 microns/pixel and 0.304 arcsec/pixel corrisponding to a 10.4×10.4 arcmin field of view. Thanks to the large field of view, this camera is particularly suitable in performing observations of standard fields. The observations were performed on the night of January 30th, 2015 and were planned in order to have a huge amount of standards, spanning a wide range in airmass, color, and magnitude. The IAC80 data were pre-reduced during the same night of the observation by the support astronomer, using a pipeline specifically developed for this telescope. The pipeline at first subtracts

[1]All available information about the telescope and instrument can be found at http://www.iac.es/OOCC/instrumentation/iac80/ and http://vivaldi.ll.iac.es/OOCC/iac-managed-telescopes/iac80/camelot/

overscan and bias from all the images, and then it created a master flat for every filter. Finally, the images with the objects are corrected for the associated flat field, to obtain the scientific images. The list of the observations is presented in Table 3.2. All the standard fields observed belong to the Landolt (1992, 2009) sample, and are accordingly labelled. The fields observed in Boötes I are labelled as BOO1 and BOO2.

Table 3.2. Summary of the observations performed at the IAC80, with the name of the field, α and δ, filter, exposure time, and airmass.

Field	α [hh:mm:ss]	δ [deg:mm:ss]	Filter	Exp. time	Aimrass
SA95	3:55:39	+00:08:24	I	45.000	1.185
SA95	3:55:40	+00:08:24	I	45.000	1.193
SA95	3:55:40	+00:08:24	I	120.000	1.198
SA95	3:55:40	+00:08:25	V	50.000	1.205
SA95	3:55:40	+00:08:25	V	100.000	1.208
SA95	3:56:01	+00:08:25	V	150.000	1.213
SA98	6:53:01	-00:23:26	V	5.000	1.188
SA98	6:53:01	-00:23:26	V	10.000	1.186
SA98	6:53:01	-00:23:26	V	50.000	1.185
SA98	6:53:22	-00:23:26	I	5.000	1.183
SA98	6:53:01	-00:23:25	I	10.000	1.182
SA98	6:53:01	-00:23:25	I	50.000	1.181
SA100	8:54:40	-00:39:51	I	20.000	1.554
SA100	8:54:19	-00:39:50	I	60.000	1.542
SA100	8:54:19	-00:39:52	V	5.000	1.528
SA100	8:54:40	-00:39:52	V	50.000	1.522
SA100	8:54:19	-00:39:52	V	75.000	1.511
SA95	3:55:20	+00:08:28	I	45.000	1.451
SA95	3:56:02	+00:08:30	I	45.000	1.485
SA95	3:55:41	+00:08:30	I	120.000	1.498
SA95	3:55:42	+00:08:32	V	100.000	1.517
SA95	3:55:42	+00:08:32	V	150.000	1.533
SA100	8:54:20	-00:40:02	V	50.000	1.262
SA100	8:54:20	-00:40:01	V	75.000	1.258
SA100	8:54:21	-00:40:01	I	20.000	1.251
SA100	8:54:20	-00:40:01	I	60.000	1.248

Continued on next page

Table 3.2 – continued from previous page

Field	α [hh:mm:ss]	δ [deg:mm:ss]	Filter	Exp. time	Aimrass
SA98	6:53:03	-00:23:23	I	5.000	1.153
SA98	6:53:03	-00:23:23	I	10.000	1.153
SA98	6:53:03	-00:23:23	I	50.000	1.154
SA98	6:53:24	-00:23:23	V	5.000	1.155
SA98	6:53:24	-00:23:22	V	10.000	1.156
SA98	6:53:03	-00:23:22	V	50.000	1.157
SA100	8:54:22	-00:39:58	I	20.000	1.147
SA100	8:54:21	-00:39:57	I	60.000	1.146
SA100	8:54:21	-00:39:57	V	50.000	1.146
SA100	8:54:21	-00:39:57	V	75.000	1.145
SA103	11:57:36	-00:31:40	I	10.000	1.638
SA103	11:57:35	-00:31:39	I	30.000	1.629
SA103	11:57:36	-00:31:39	V	15.000	1.615
SA103	11:57:36	-00:31:41	V	45.000	1.606
PG1047	10:50:49	-00:05:02	V	30.000	1.248
PG1047	10:50:49	-00:05:04	V	30.000	1.240
PG1047	10:50:50	-00:05:04	V	90.000	1.236
PG1047	10:50:50	-00:05:03	I	30.000	1.230
PG1047	10:50:50	-00:05:03	I	120.000	1.225
SA100	8:54:22	-00:40:06	I	20.000	1.158
SA100	8:54:44	-00:40:06	I	60.000	1.158
SA100	8:54:23	-00:40:06	V	50.000	1.160
SA100	8:54:23	-00:40:06	V	75.000	1.162
SA98	6:53:06	-00:23:14	V	5.000	1.640
SA98	6:53:27	-00:23:14	V	10.000	1.643
SA98	6:53:27	-00:23:14	V	50.000	1.650
SA98	6:53:06	-00:23:14	I	5.000	1.662
SA98	6:53:06	-00:23:14	I	10.000	1.668
SA98	6:53:06	-00:23:14	I	50.000	1.674
PG1047	10:50:49	-00:05:04	I	120.000	1.155
PG1047	10:50:50	-00:05:04	V	90.000	1.152
SA103	11:57:16	-00:31:50	V	30.000	1.258
SA103	11:57:51	-00:31:57	V	30.000	1.252
SA103	11:57:30	-00:31:59	V	45.000	1.249
SA103	11:57:30	-00:31:58	I	15.000	1.245
SA103	11:57:30	-00:31:58	I	30.000	1.243

Continued on next page

Table 3.2 – continued from previous page

Field	α [hh:mm:ss]	δ [deg:mm:ss]	Filter	Exp. time	Aimrass
SA100	8:54:23	-00:39:59	V	75.000	1.299
SA100	8:54:24	-00:39:59	V	50.000	1.305
SA100	8:54:45	-00:39:59	I	20.000	1.309
SA100	8:54:24	-00:39:59	I	60.000	1.313
PG1323	13:26:59	-08:54:29	I	20.000	1.372
PG1323	13:26:39	-08:54:29	I	40.000	1.368
PG1323	13:26:39	-08:54:28	V	60.000	1.363
PG1323	13:26:39	-08:55:08	V	60.000	1.264
PG1323	13:26:39	-08:55:08	I	40.000	1.266
BOO1	14:01:37	+14:32:42	I	60.000	1.386
BOO1	14:01:16	+14:32:43	I	60.000	1.365
BOO1	14:01:16	+14:32:44	I	300.000	1.353
BOO1	14:01:16	+14:32:40	V	300.000	1.321
BOO2	14:00:08	+14:19:06	V	60.000	1.260
BOO2	14:00:08	+14:19:07	V	300.000	1.253
BOO2	14:00:08	+14:19:05	I	300.000	1.233
BOO2	14:00:30	+14:19:07	I	60.000	1.213

We have applied the photometry and the aperture correction (see Appendix C) on the fields listed in Table 3.2 to obtain the instrumental magnitudes.

The calibrated magnitudes of Boötes I were obtained following the steps described in Section 2.4. In this case we have used the catalogue of photometric standard stars developed by Landolt (2009).

Figure 3.2 shows the derivation of the extinction and of the calibration coefficients for the standard stars, obtained doing a linear fit. These values were then used in the Equations 2.1 and 2.2 to obtain calibrate magnitudes of Boötes I observations performed with the IAC80. Hence, these stars are used as local standard stars to calibrate the images of Boötes I observed with the Subaru Telescope.

The transformation equations between the images of Boötes I observed with IAC80 (local standard starsand) and those observed with Subaru Telescope have given as final values of the zero point (Z) and the color term (C) those presented in Table 3.3. This calibration performed with IAC80 has however given questionable values of the color terms: this is too large (in terms of absolute value) in the filter I while the associated error in the filter V is bigger than the term

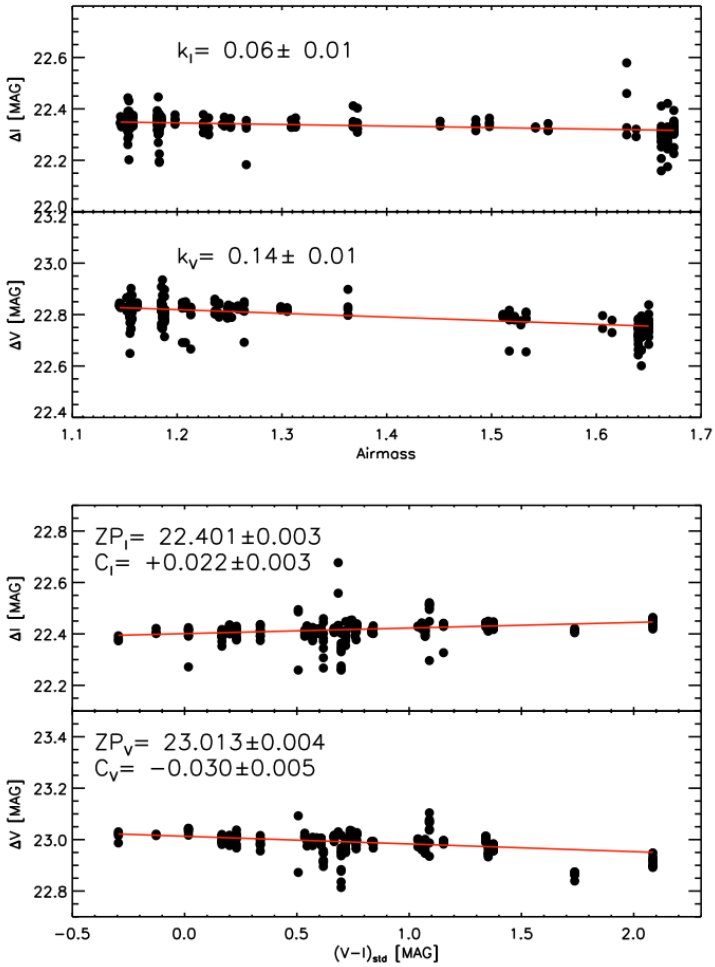

Figure 3.2. Calibration equation for the IAC80 data. *Top panels:* Δm as a function of the airmass for both the I (upper panel) and V band (lower panel). $\Delta m = m_{std} - m_{instr}$, where m_{std} is the standard magnitude and m_{instr} is the instrumental magnitude, for V and I. The best fit is shown in red. The resulting extinction coefficients are indicated in the figures, with the associated errors. *Bottom panels:* Calibration equations for the two photometric bands obtained by using the extinction coefficients derived. The best fit is indicated in red and the resulting coefficients are shown in the figure with their uncertainties.

itself. For this reason we have decided to fine_tuning the calibration by the comparison with the Okamoto CMD published in Okamoto et al. (2012).

Figure 3.3 show our final calibrated CMD of Boötes (in red) with CMD published by Okamoto et al. 2012 (in black). The new values of Z and C calculated through the comparison with Okamoto CMD are listed in Table 3.3.

Filter	IAC80		Okamoto CMD	
	Zero point (Z)	Color term (C)	Zero point (Z)	Color term (C)
V	7.488±0.357	0.025±0.026	7.510±0.015	0.047±0.016
I	7.819±0.086	-0.165±0.061	7.845±0.019	-0.01±0.005

Table 3.3. Transformation equations between IAC80 and Subaru: final values of the zero point (Z) and the color term (C) for the filters V and I.

3.4 CMD of Boötes I

The calibrated CMD is show in Figure 3.4. Only objects with $\sigma \leq 0.1$, $chi \leq 1.2$ and $|sharp| \leq 0.25$ were considered stars. The magnitudes have been corrected for distance modulos ($(m - M)_0 = 19.11$) and extinctions ($A_V = 0.047$ and $A_I = 0.026$).

Two isochrones with Z = 0.0001 and 12.6 and 13.7 Gyr belong to the BaSTI library (Pietrinferni et al., 2004) are overlaid. These metallicity and ages are the same used in Okamoto et al. 2012, with the difference that they use Padova isochrones (Marigo et al., 2008). The fiducial sequence of MS is best reproduced by the isochrone of 13.7 Gyr, consistent with the age roughly estimated from the comparison with M92 in Okamoto et al. 2012. The metallicity of M92 is [Fe/H] = -2.28 (Harris, 1996), and its age is estimated as 14.2 ± 1.2 Gyr (Paust et al., 2007).

A first analysis of the CMD of Boötes immediately reveals that this closely resembles that of a Galactic Globular Cluster (GGC) even if more massive and concentrated. The presence of the old MSTO and of the HB indicates that this galaxy is dominated by an old population. Furthermore, we can note the presence of blue stragglers (BS) in the left part of the diagram, at the height of the base of the TO. BS stars are universally found in Galactic globular clusters, open clusters, the halo field, and in several Galactic dSphs (e.g., Bailyn 1995; Piotto et al. 2004; Mapelli et al. 2007). They can form from stellar collisions in high-density regions, or through mass transfer in isolated primordial binaries. The distribution of BS candidates in UFDs implies that these stars are not young

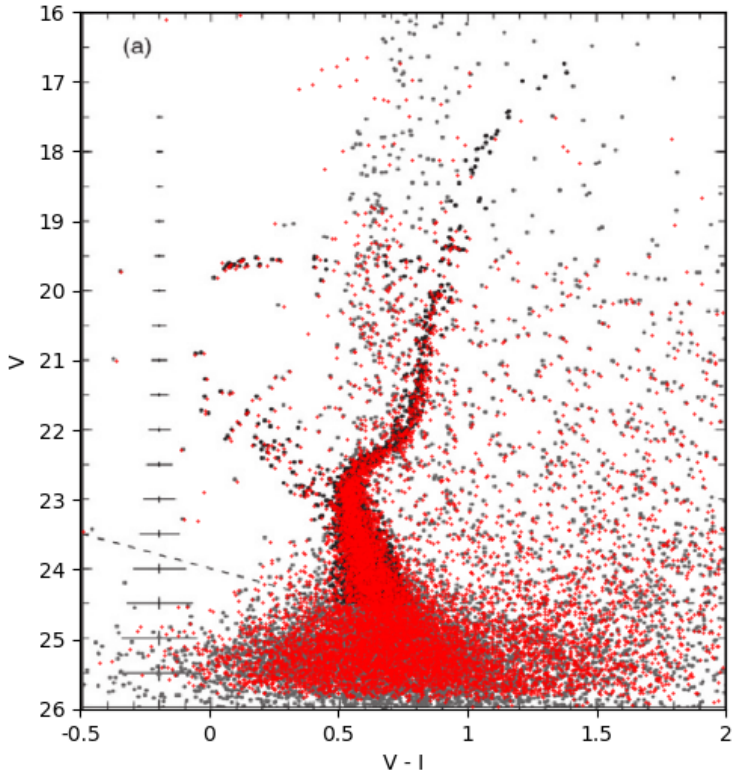

Figure 3.3. Comparison between our final calibrated CMD of Boötes (in red) with CMD published by Okamoto et al. 2012 (in black).

MS stars, but mass-transfer BS stars that evolved from primordial binaries, as found in other dSphs (e.g., Mapelli et al. 2007; Okamoto et al. 2008a).

3.5 Completeness Tests

To estimate the completeness and errors affecting our photometry, we adopted a standard method of artificial-star tests. The completeness tests were performed by adding synthetic stars to the individual images and repeating the photometric analysis identically as for the real data. A detailed description of this procedure is provide in Section D.2.

In the case of Boötes, 26,000,000 stars were simulated in the chip. We injected artificial stars with random colors and magnitudes selected to cover the whole observed CMD. This is important in order of properly simulate observational effects on other synthetic CMDs. Once the artificial stars were injected, the new synthetic frames were photometrically processed in the same way and with the same parameters as the original images. The same photometric calibration corrections were applied to the magnitudes of the fake recovered stars, with the exception of the aperture correction, since the PSF injects stars with all the flux within the selected PSF radius.

Figure 3.5 show the $\Delta mag = mag_{in} - mag_{out}$ of the artificial stars for the two bands, as a function of the input magnitude. The completeness of Boötes I is shown in Figure 3.6.

3.6 The SFH of Boötes I

Using the IAC method described in Appendix D we derived the SFH of Boötes I. The accuracy of the result depends on the depth of the CMD of the studied galaxy. To obtain the SFH, the regions of the CMD more sensitive to the age, as the MS TO, are used.

3.6.1 CMD model

The synthetic CMD (sCMD) was created using IAC-star (Aparicio & Gallart, 2004). In this case, the synthetic CMD contains 10^7 stars with a constant SFR between 2 and 13.5 Gyr and a uniform metallicity distribution between Z = 0.00001 and Z = 0.001, corresponding to [Fe/H] = -3.28 and -1.27, respectively. The range in metallicity was selected in order to cover the expected metallicity of the stars in this galaxy. We chose the BaSTI evolutionary library (Pietrinferni et al., 2006), a Kroupa IMF (Kroupa, 2001), and a binary fraction of 30%.

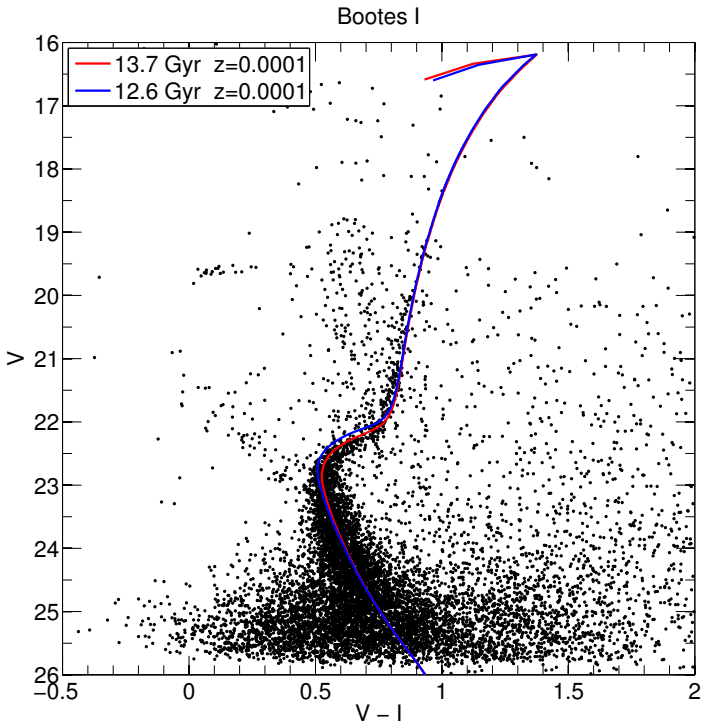

Figure 3.4. Calibrated CMD of Boötes I. Two isochrones with Z = 0.0001 and 12.6 and 13.7 Gyr belonging to the BaSTI library (Pietrinferni et al., 2004) are overlaid.

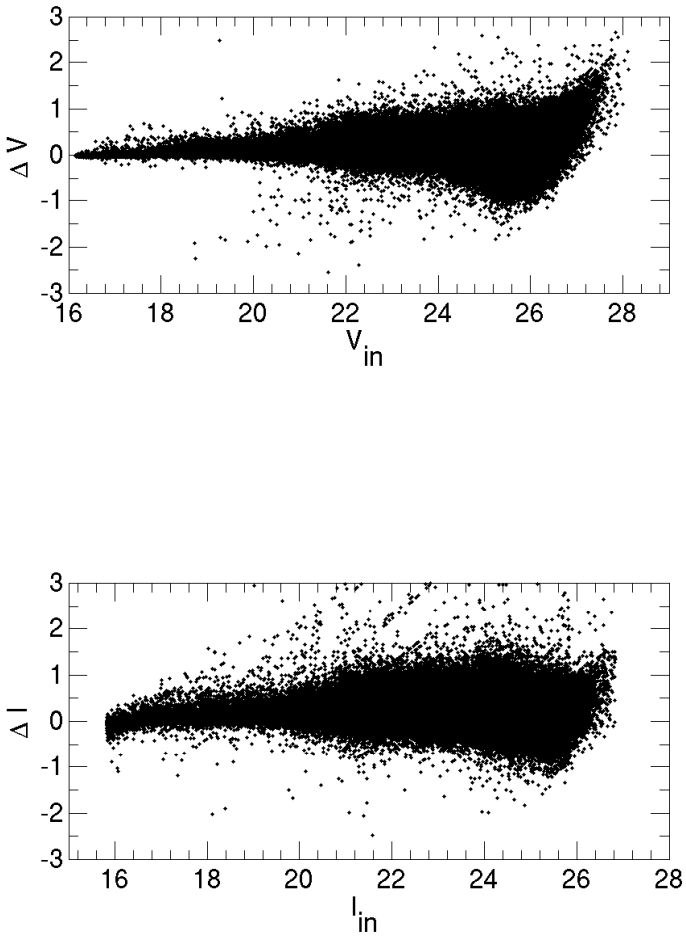

Figure 3.5. Difference $\Delta mag = mag_{in} - mag_{out}$ for synthetic stars as a function of the input magnitude.

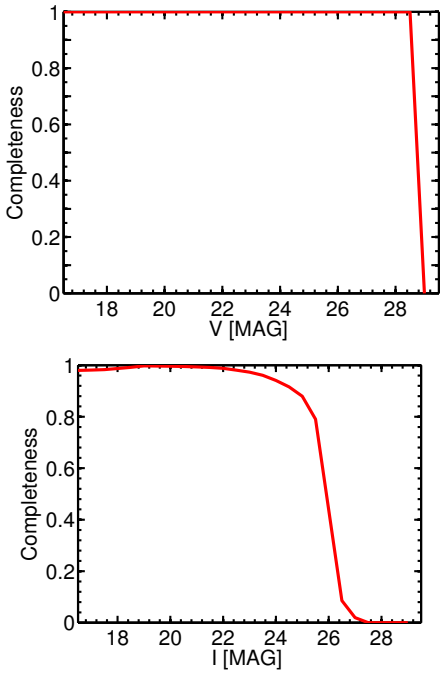

Figure 3.6. Result of the false star tests for Boötes I, in the V *(upper panel)* and I *(lower panel)* filters.

The observational effects were simulated in the synthetic CMD with the routine *obersin*, as described in Section D.2. Thus, the IAC-pop/MinnIAC (Aparicio & Hidalgo 2009; Hidalgo et al. 2011) were applied to derive the accurate SFH for Boötes I.

As mentioned in Section D.1, several bundles have been defined onto the sCMD. Each one has been sampled by grids of different box sizes, which depend on the CMD region or bundle. Grids are thinner in regions where age and metallicity resolution are better, like the main sequence (MS), and coarser in regions in which the distribution of stars strongly depends on poorly known parameters, like the RGB or the horizontal branch (HB). The number of boxes in a grid ranges from one to several hundreds depending on the CMD region.

The parameterization of the CMD relies on the concept of bundles (see Aparicio & Hidalgo 2009 and Figure 10), that is, macro-regions on the CMD that can be sub-divided into boxes using different appropriate samplings. The number of boxes in the bundle determines the weight that the region has for the derived SFH. This is an efficient and flexible approach for two reasons. First, it allows a finer sampling in those regions of the CMD where the models are less affected by the uncertainties in the input physics (MS and SGB). Second, the dimensions of the boxes can be increased, and the impact on the solution decreased, in those regions where the small number of observed stars could introduce noise due to small number statistics or where we are less confident in the stellar evolution predictions. The basic age and metallicity bins defining the simple stellar populations (SSPs) used are as follows:

- Age: $[2\ 5\ 7\ 9\ 10{:}0.25{:}13.5]\times10^9$ years
- Metallicity: [0.00001 0.00003 0.00005 0.0001].

These numbers define the boundaries of the bins, not their centers. Therefore, they fix $18 \times 3 = 54$ simple populations. These values were selected according to the age and metallicity resolution tests presented in Section 3.6.2.
Figure 3.7 shows the bundles used, overplotted on the sCMD. No bundles include the stars in evolved evolutionary phases, and in particular we excluded both the RGB and the HB from our analysis. The reasons are many. First, the physics governing these evolutionary phases is more uncertain than that describing the MS, and differences between stellar libraries are more important in these evolved phases (Gallart et al., 2005). Moreover, the details of the HB morphology also depend on highly unknown factors like the mass loss during the RGB phase. However, despite not including the RGB stars, we routinely adopt a bundle that is redder than the RGB (magenta bundle in Figure 3.7). In order to aid in setting a mild constraint on the upper limit of the metallicity of the RGB Boötes

stars, this was drawn at the red edge of the RGB. It includes metal-rich stars present in the model, but very few objects of the observed CMD. Extensive tests have shown that including a bundle on the RGB neither improves the solution, nor produces a solution significantly different. Rather, the χ^2 of the solution increases substantially and likely spurious populations appear, such as old and metal-rich stars.

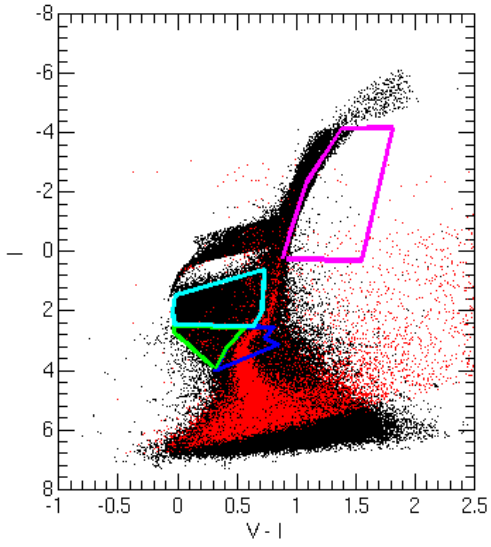

Figure 3.7. Regions of the CMD (bundles) used for gridding. Bundles are shown overplotted on the observed CMD (in red) and on the synthetic CMD (in black) used as an input model for the SFH derivation.

To minimize the uncertainties of external parameters (distance, reddening and photometry zero point), the SFH is derived for different offsets in color and magnitude applied to the observed CMD (oCMD). The offset giving the minimum χ^2 is assumed as the best. The minimum was confirmed at the position $(\Delta\text{col}; \Delta\text{mag}) = (0; 0)$.

3.6.2 Estimating time resolution in the SFH

Observational uncertainties as well as the uncertainties inherent to the SFH computation procedure result in a smoothing of the derived SFH and a decrease of the age resolution. Having an accurate estimate of the latter is fundamental to ascertain the reliability of the solutions and to better characterize the properties of the galaxy. We have calculated the age resolution as a function of time by recovering the SFH of a set of mock stellar populations corresponding to very narrow bursts (10^6 years) occurring at different times. Four mock populations have been computed, each one with a single burst at ages of 10, 11, 12 and 13.5 Gyr. We used IAC-star to create the CMDs associated with each mock stellar population. Observational uncertainties were simulated in the CMDs by using the results of the DAOPHOT completeness tests. The SFHs of the mock stellar populations were then obtained using identical procedure as for the real data. In all cases, the recovered SFH is well fitted by a Gaussian profile with σ depending on the burst age. Figure 3.8 shows the input bursts and the corresponding Gaussian profile fits to the solutions, including their peak age and σ. From these fits we estimate an intrinsic age resolution (σ) of $\sim$ 1.1 Gyr at the oldest ages which improves to $\sim$ 0.8 Gyr at an age of 10 Gyr. Also, a shift toward younger ages is observed between the input and solution ages. We can note that at 10 Gyr the SFH is recovered worse than at 12 Gyr probably due to the age-metallicity degeneracy.

We performed several tests on the mocks changing the side of MS bundle and the age and metallicity bins. The solutions giving the minimum χ^2 are assumed as the best and those we chose to get the SFH of the galaxy (see Section 3.6.1).

3.6.3 Results

In Figure 3.9 we show the SFR, the age–metallicity relation (AMR) and the cumulative mass fraction of Boötes I as a function of time with their associated errors. The bulk of the star formation of Boötes occurred at old epochs and appears to be characterised by one burst of star formation, which took place $\sim$ 13.5 Gyr ago. The initial episode of star formation lasted until roughly 12.5 Gyr ago, so the width of the burst is $\sim$ 1 Gyr. Boötes I is a very metal poor system. The mean metallicity of the solution is [Fe/H] = -2.53 $\pm$ 0.14. This value is in very good agreement with that measured spectroscopically [Fe/H] = -2.59 $\pm$ 0.43 (Lai et al., 2011).

Figure 3.10 presents a comparison between the observed CMD and a best-fit CMD (left and central panels). The latter has been built using IAC-star with the solution SFH of Boötes I as input. The right panel show the residual

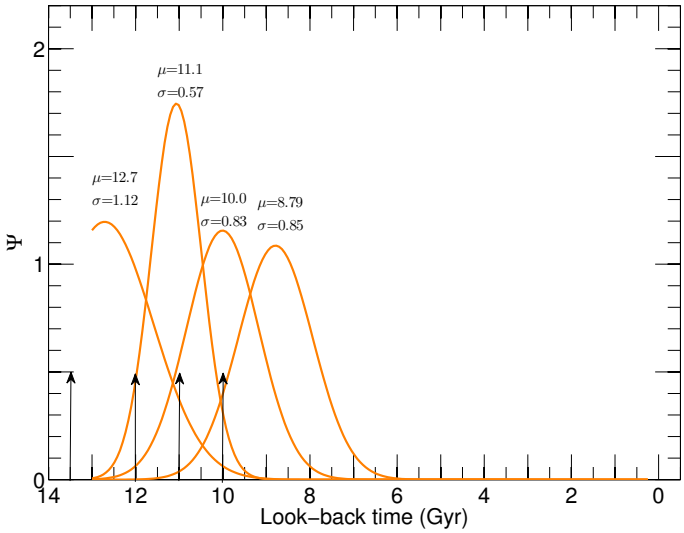

Figure 3.8. Age resolution tests of Boötes for four different burst ages, namely 13.5; 12; 11 y 10 Gyr. Arrows indicate the burst age of the simulated populations. The heights of the arrows are not indicative of burst intensity. Curves show the Gaussian profile fits to the solutions. The solution peaks (μ) and standard deviations (σ) are given.

Hess diagram, shown in unit of Poisson errors. Two bundles used to derive the solution have been superimposed on the CMDs. The right panel shows the residual Hess diagram, in units of Poisson error, which supports the good agreement between the observed and the best-fit CMD.

3.7 Spatial Distribution of Stellar Populations

To study the distribution of stellar populations in Boötes I as a function of radius, we selected two regions in the field observed: an inner region delimited by an ellipse with ellipticity $\epsilon = 0.39$ that is the same mesured for the galaxy (Martin et al., 2008a) with radius $r \leq 6$ arcmin and an outer one with radius $r > 10$ arcmin. We have selected a similar number of stars within each bundles, for the inner and outer regions. Table 3.4 show the number of stars in each bundle, while Figure 3.11 show the spatial distribuition and the CMDs of the inner and outer regions of the galaxy.

	Inner	Outer
Bundle 1	367	285
Bundle 2	23	30
Bundle 3	26	68
Bundle 4	0	0
Total	416	383

Table 3.4. Summary of the number of stars in each bundles.

We derived the SFH of the inner and outer separately, following the steps described in Section 3.6. The same sCMD, SSPs and bundles were used as in the case of global SFH. The main features of the SFH of inner (left panels) and outer (right panels) regions of Boötes I can be observed in Figure 3.12. In both cases the bulk of the star formation occurred at $\sim$ 13.5 Gyr ago and the width of the burst is $\sim$ 1 Gyr, as before. Even the mean metallicity is unchanged. The mean metallicity is [Fe/H] = -2.52 $\pm$ 0.15 for the inner region and [Fe/H] = -2.54 $\pm$ 0.14 for the outer one.

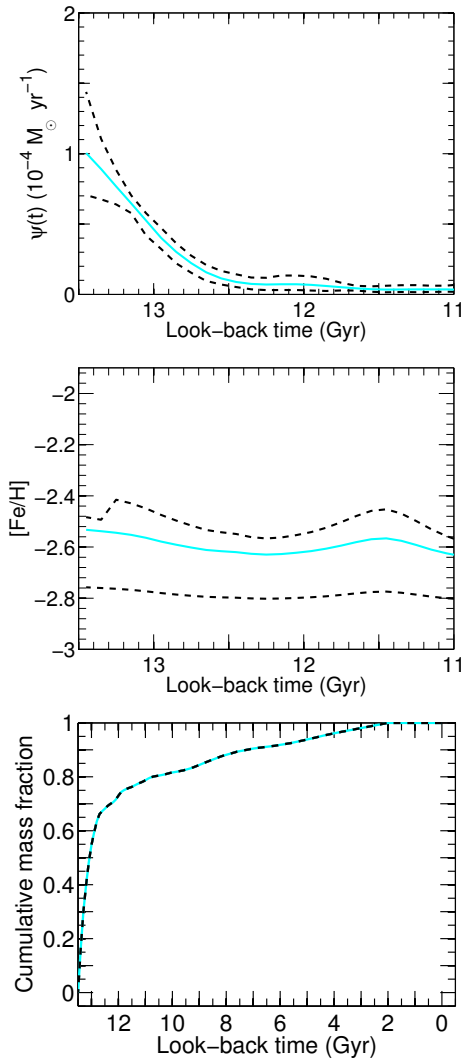

Figure 3.9. *From top to the bottom:* the SFH, metallicity and cumulative mass function as a function of look-back time. Continuos line shows the solution, dashed lines show 1σ error bar.

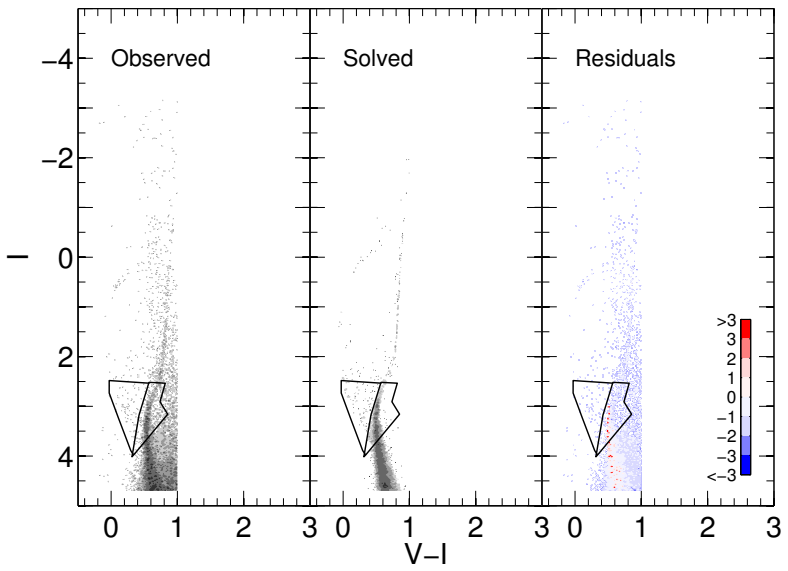

Figure 3.10. Observed *(left panel)*, calculated *(central panel)*, and residual Hess diagram*(right panel)* CMDs. The calculated CMD has been built using IAC-star with the solution SFH of Boötes I as input. The black lines mark the position of two of the bundles (those containing more stars) adopted to derive the solution. The residuals are in units of Poisson uncertainties. The observed CMD shows a background of field stars.

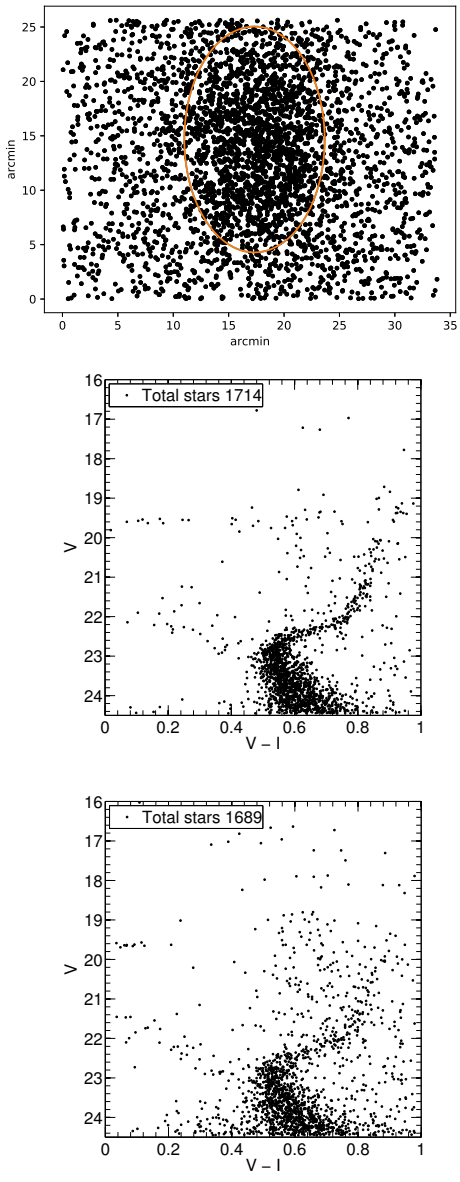

Figure 3.11. *Top panel:* Spatial distribuition of Boötes I. The ellipse mark the inner region of the galaxy. The CMDs of inner (*middle panel*) and outer (*bottom panel*) regions of Boötes I.

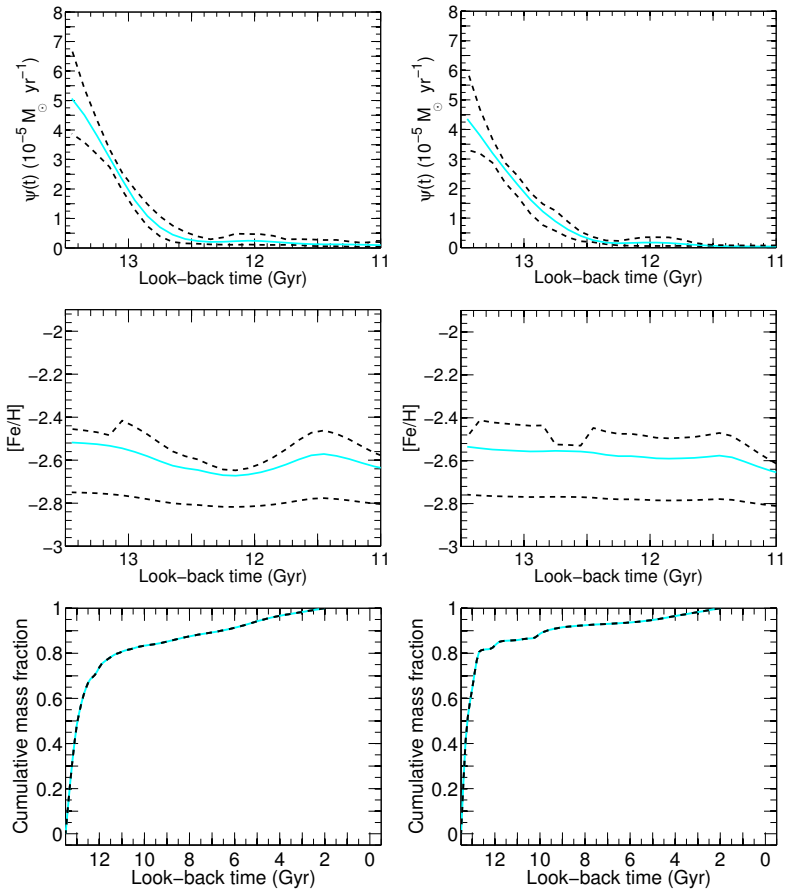

Figure 3.12. Summary of inner and outer SFH result of Boötes I. SFR, AMR and cumulative mass fraction of inner *(first column)* and outer *(second column)* regions.

3.8 Duration of the Main Star Formation Episode of Boötes I

It is particularly important to determine the oldest age at which star formation occurred in each of our galaxies and the real duration of the first, main star formation episode. It is important for several reasons: firstly to determine if the energy released by the SNe were enough to remove the gas from the potential well and stop the star formation. The amount of energy put in the intergalactic medium (IGM) by the SNe is not changed since it is determine by the integral of the SFH, but to inject this energy in an shorter time formation would produce a different scenario. Secondly, to determine if this galaxy have been affected by the Epoch of Reionization (EoR), being true fossil records of the EoR.

We used IAC-star to create a set of mock stellar populations with a single burst centered at 13.5 Gyr (the peak of the SFH of Boötes I), metallicity equal to the mean metallicity obtained in the SFH and with the same numbers of stars as the observed CMD. The mocks have been created with SFHs defined as Gaussian profile shaped bursts of different σ: 10 Myr, 20 Myr, 50 Myr, 100 Myr, 200 Myr, 500 Myr, 750 Myr, 1 Gyr, 1.5 Gyr and 2 Gyr. For the mock populations, five simulations have been done with different random number seeds in order minimize stochastic effects. Observational uncertainties were simulated in the associated CMDs and the SFHs were recovered following the same process as for the galaxy. In all cases, the recovered SFHs are well fitted by Gaussian profiles where the relationship between FWHM and the standard deviation is $FWHM = 2\sqrt{2\,ln2}\,\sigma \approx 2.355\,\sigma$.

Figure 3.13 shows a cubic fit to the FWHM of the solutions, $FWHM_{rec}^{mock}$, as a function of the input ones, $FWHM_{in}^{mock}$ for Boötes I. If the actual SFH of the galaxy was well described as a Gaussian profile, its FWHM could be inferred by interpolating in this fit, which gives $FWHM_{in}^{obs} = 1.45$ Gyr for Boötes I.

3.9 Discussion and Conclusions

We have presented an analysis of the SFH of the ultra-faint dwarf galaxy Boötes I, based on deep photometry obtained with the Subaru/Suprime-Cam.

A deep CMD reaching the oldest main-sequence turnoffs has been obtained. Exhaustive crowding tests have been performed in order to properly characterize the observational effects.

The SFH for the entire lifetime of the galaxy has been obtained. The solution shows that the SFH of Boötes is dominated by an old, main episode with a peak occurring $\sim$ 13.5 Gyr ago and a duration estimated in 1.45 Gyr (FWHM, see

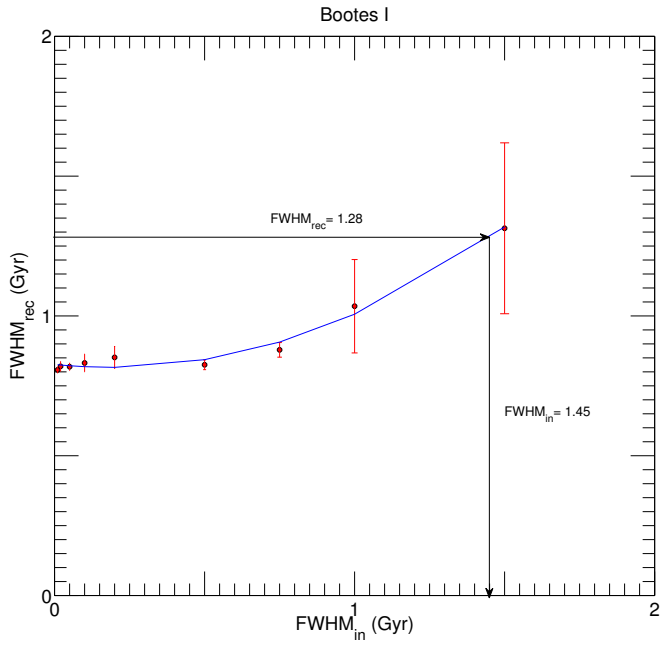

Figure 3.13. A cubic fit to the data is shown, together with the FWHM value measured in the real data solution ($FWHM_{rec}^{obs}$) and the corresponding real value inferred using the fit ($FWHM_{in}^{obs}$). The error bar are calculated as a 1σ error.

Section 3.8). This means that the star formation ended close to $\sim$ 12 Gyr ago. Boötes stopped early to form stars and it is of great interest to investigate if this phenomenon is linked in any way to the ultraviolet (UV) cosmic reionization, or if it is mainly due to local causes, such as intense galactic winds and SNe feedback (Hidalgo et al. 2011, Aparicio et al. 2016, Lanfranchi & Matteucci 2004).

Evidence from quasar spectra indicates that the Universe was fully reionized by z $\sim$ 6, corresponding to a look-back time of $\sim$12.7 Gyr (Becker et al., 2001). Observing the cumulative mass fraction from Figure 3.9 it is clear that $\sim$ 66% of the stellar mass of Boötes I has been formed before reionization (z $>$ 6, 12.7-13 Gyr ago). This scenario is compatible with the hypothesis that reionization by the UV background may have contributed to the suppression of star formation in Boötes I.

Another possibility is that the star formation in Boötes was stopped by the removal of the gas by purely internal processes, such as the explosion of SNe. If the mechanical energy produced by SNe had significantly blown away the gas in Boötes, star formation would have strongly declined or even stopped after the main peak, as it can be observed in Cetus or Tucana dwarf galaxies (Monelli et al. 2010a, 2010b).

Boötes I is a very metal poor system. The mean metallicity of the solution is [Fe/H] = -2.53 $\pm$ 0.14. This value falls within the errors of the calculated value measured spectroscopically by Lai et al. (2011) that is [Fe/H] = -2.59 $\pm$ 0.43.

We have also studied the distribution of stellar populations in Boötes as a function of radius, selecting two regions in the field observed. The SFH obtained for the inner and outer regions does not differ substantially from that obtained for the entire galaxy. In both regions the bulk of the star formation occurred at $\sim$ 13.5 Gyr ago and the width of the burst is $\sim$ 1 Gyr, as before. Even the mean metallicity is unchanged. The mean metallicity is [Fe/H] = -2.52 $\pm$ 0.15 for the inner region and [Fe/H] = -2.54 $\pm$ 0.14 for the outer one. So we can say that the galaxy, within the observed field (34$\times$27 arcmin) does not shows an stellar population gradient.

4

Canes Venatici II

In this chapter we will focus on the analysis of the ultra-faint dwarf galaxy Canes Venatici II. The data comes from WFC@ACS at the Hubble Space Telescope. The resulting CMD and the estimate of age and metallicity using isochrone fitting are discussed in Section 4.3. The SFH of Canes Venatici II is considered in Section 4.5 and the study of the presence of multiple stellar populations using the RGB region with GTC data is presented in Section 4.7.

4.1 Introduction

CANES Venatici II (Cvn II) is one of the faintest of the newly discovered SDSS galaxies (Sakamoto & Hasegawa, 2006), with M_V = -4.9±0.5 mag and surface brightness ∼26.1 mag $arcsec^{-2}$ (Martin et al., 2008a). It is a low-mass [(2.4±1.1)×$10^6 M_\odot$; Simon & Geha, 2007], compact dSph with half-light radii of r_h (Plummer) = 158 pc and r_h (exponential) = 149 pc (Greco et al., 2008), at a distance d = 160 kpc (Martin et al., 2008a). Based on spectroscopic results, CVn II appears to be dark matter dominated with an $M/L_V = 360^{+380}_{-180}$ (Wolf et al., 2010) and is metal-poor, with $\langle [Fe/H] \rangle$ = -2.21 (Kirby et al., 2011).

A summary of the fundamental parameters of CvnII is show in Table 4.1.

4.2 Dataset

The data of Canes Venatici II were taken in 2012 May using the F606W and F814W filters on ACS (GO-12549; PI: Brown). We got the images from the *Hubble Space Telescope*. The field of view of ACS images is 202″ × 202″, which

Parameter	Value	References[a]
RA (hhmmss)	12 57 10	(1) (2)
Dec (^{o} ' ")	+34 19 15	(1) (2)
Galactic longitude, l	113.6^o	(1) (2)
Galactic latitude, b	82.7^o	(1) (2)
Position angle	$177^o \pm 9^o$	(5)
Ellipticity ϵ	0.52±0.11	(5)
E(B - V)	0.010	(3)
$(m-M)_0$	21.02±0.06	(3)
Heliocentric distance (kpc)	160±4	(5)
Heliocentric velocity (km s^{-1})	-128.9±1.2	(4)
Apparent magnitude V	16.1±0.5	(5)
Half-light radius r_h (pc)	74±14	(5)
Absolute magnitude M_V	-4.9±0.5	(5)
Half-light radius r_h (arcmin)	1.6±0.30	(5)
Barionic mass $M_\star$ ($10^6 M_\odot$)	0.0079	(3)
$[Fe/H]$	-2.21±0.05	(6) (7)

[a] References: (1) Belokurov et al., 2007; (2) Greco et al., 2008; (3) McConnachie, 2012; (4) Simon & Geha, 2007; (5) Martin et al., 2008a; (6) Kirby et al., 2008; (7) Kirby et al., 2011.

Notes. The stellar mass is computed from the integrated V-band luminosity and assumes $M \odot / L \odot = 1$.

Table 4.1. Fundamental parameters of Canes Venatici II.

corresponds to $3.37' \times 3.37'$. Table 2.4 list the coordinates and the total exposure time in each filter.

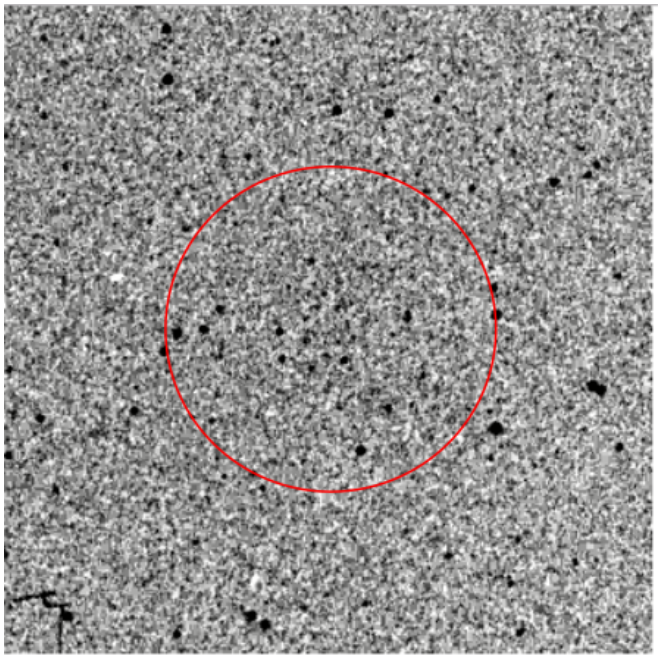

Figure 4.1. Field of view ($10' \times 10'$) of CvnII. The galaxy is located at the center of the red circle. Because of the low surface brightness of the galaxy, it cannot be distinguished from the foreground stars.

The HST images were pre-reduced by the HST team, using a specific calibration pipeline (Lucas, 2016). The ACS calibration pipeline assembles data received from HST into datasets, applies standard calibrations (so that calibrated image header keyword values can be entered in the Archive database), and stores uncalibrated datasets in the HST Data Archive. When a user requests data, the OTFR (On-The-Fly-Reprocessing) system delivers freshly-calibrated data, processed by **calacs** and **AstroDrizzle**, as multi-extension FITS files. Therefore, the pipeline processing is carried out by two separate image pro-

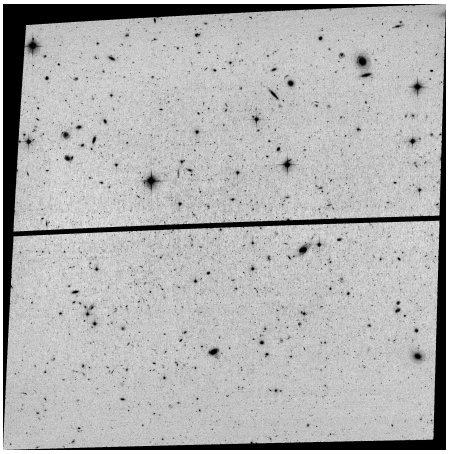

Figure 4.2. The WFC@ACS field of CvnII in F814W filter. The field of view is $202'' \times 202''$, the pixel scale is $\sim$0.05"/pixel and the surface brightness of the galaxy is 26.1 mag $arcsec^{-2}$ (Martin et al., 2008a).

cessing packages: **calacs** corrects for instrumental effects to produce calibrated products. **AstroDrizzle** corrects for geometric distortion, performs cosmic ray rejection on combined images, and for dithered images, also removes hot pixels.

The **calacs** pipeline consists of five individual calibration tasks: *acsccd*, *acscte*, *acsrej*, *acs2d*, and *acssum*. Each single-exposure raw image undergoes standard detector calibrations in calacs, such as bias subtraction, dark subtraction, and flat-fielding to create a `flt.fits` image. For WFC images, calacs produces counterpart data files that have undergone pixel-based CTE corrections. The CTE-corrected final data products have suffixes `flc.fits`. Later in the pipeline, after **calacs** processing is completed, `flt.fits/flc.fits` images will be corrected for geometric distortion and drizzle-combined, with cosmic ray and hot pixel removal, by **AstroDrizzle**. The resulting drizzled image, in units of electrons/second, is written to a file with the suffix `drz.fits/drc.fits` (for WFC, data from the two chips are mosaicked together as one image.). Figure 4.3 show a flow diagram of the ACS calibration pipeline.

We used `flc.fits/drc.fits` images to perform the photometry of CvnII. In this case the photometry was obtained using DOLPHOT. Section C.3 presents the details for obtaining photometry with DOLPHOT.

4.3 CMD of Canes Venatici II

The CMD of CVNII is show in Figure 4.4. Only objects with $\sigma \leq 0.1$, $chi \leq 1.2$ and $|sharp| \leq 0.25$ were considered stars. The magnitudes have been corrected for distance modulus ($(m-M)_0 = 21.01$; Okamoto et al. 2012) and extinctions ($A_{F606W} = 0.024$ and $A_{F814W} = 0.015$; Schlafly & Finkbeiner 2011). We got a deep CMD reaching 28 mag in the F814W filter, that is ∼4 mag below the old MSTO. The MS and RGB are well defined, while the HB is just sketched. Two isochrones with Z = 0.0001 and 12.5 and 13.5 Gyr belong to the BaSTI library (Pietrinferni et al., 2004) are overlaid. The fiducial sequence of MS, TO and SGB is quite well reproduced by the isochrones, but it is not the same for the RGB.

4.4 Completeness Tests

Our analysis of the photometry completeness follows the procedure proposed by Aparicio & Gallart (1995). The procedure is the same as for Boötes and described in Section D.2. In short, a list of artificial stars is made. A total of 2.387.634 artificial star were injected in the images with a range of magnitude and colors to cover the complete range of observed stars in the CMD of CvnII.

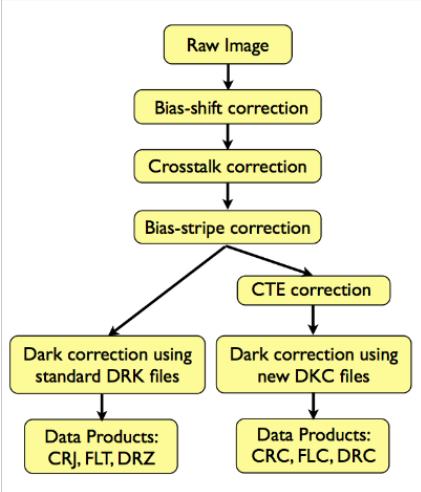

Figure 4.3. Flow diagram of the ACS calibration pipeline. The first branch contains traditional CALACS processing using standard darks (_DRK reference files) to produce standard data products: _CRJ, _FLT and _DRZ.fits files. The second branch will correct for CTE degradation, perform dark correction using new CTE-corrected darks (_DKC files), and then standard processing to produce new data products, called _CRC, _FLC and _DRC.fits files. The user will be able to choose whether to use the CTE-corrected or standard data products.

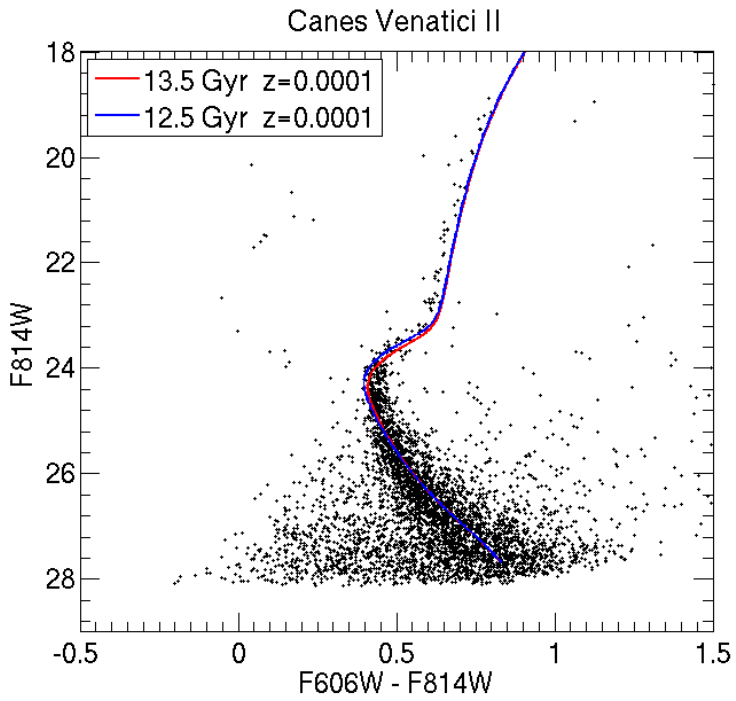

Figure 4.4. CMD of Canes Venatici II. This CMD has been decontaminated using the procedure described in the text. Two isochrones with Z = 0.0001 and 12.5 and 13.5 Gyr belong to the BaSTI library (Pietrinferni et al., 2004) are overlaid.

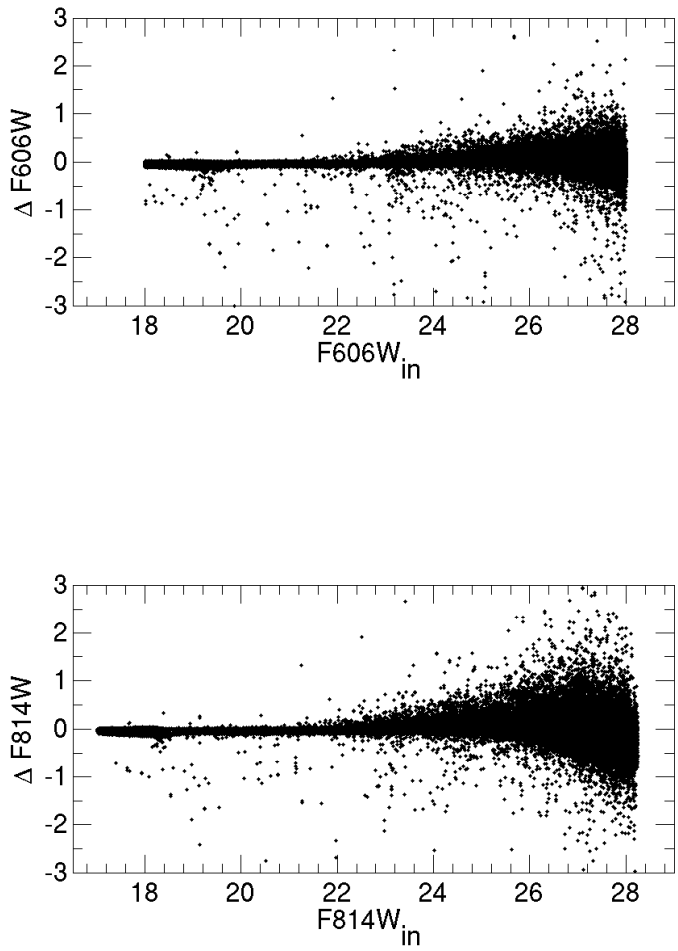

Figure 4.5. Difference $\Delta mag = mag_{in} - mag_{out}$ for synthetic stars as a function of the input magnitude.

Figure 4.5 show the $\Delta mag = mag_{in} - mag_{out}$ of the artificial stars for the two bands, as a function of the input magnitude. The completeness of CvnII is shown in Figure 4.6.

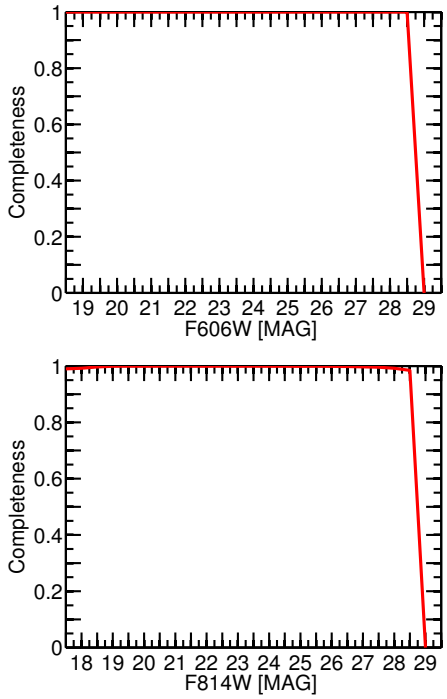

Figure 4.6. Result of the false star tests for Canes Venatici II, in the F606W *(upper panel)* and F814W *(lower panel)* filters.

4.5 The SFH of Canes Venatici II

As for Boötes, the SFH of CvnII has been obtained using the IAC method described in Appendix D.

4.5.1 CMD model

The synthetic CMD (sCMD) was created using IAC-star (Aparicio & Gallart, 2004). It contains 10^7 stars with a constant SFR between 2 and 13.5 Gyr and a uniform metallicity distribution between Z = 0.00001 and Z = 0.001, corresponding to [Fe/H] = -3.28 and -1.27, respectively. The range in metallicity was selected in order to cover all the metallicities of the stars in this galaxy (Kirby et al. 2008, 2011). We chose the BaSTI evolutionary library (Pietrinferni et al., 2006), a Kroupa IMF (Kroupa, 2001), and a binary fraction of 30%. The observational effects were simulated in the synthetic CMD with the routine *obsersin*, as described in Section D.2. Thus, the IAC-pop/MinnIAC (Aparicio & Hidalgo 2009; Hidalgo et al. 2011) were applied to derive the accurate SFH for CvnII.

As mentioned in Section D.1, several bundles have been defined onto the sCMD (Figure 4.7).

The basic age and metallicity bins defining the simple populations used are:

- Age: [2 5 7 9 10:0.25:13.5]$\times 10^9$ years
- Metallicity: [0.00001 0.00003 0.00005 0.0001 0.0003].

They fix $18 \times 4 = 72$ SSPs. These values were selected according to the age and metallicity resolution tests presented in Section 3.6.2.

To minimize the effects of external parameters (distance, reddening and photometry zero point), the SFH is derived for different offsets in color and magnitude applied to the observed CMD (oCMD). The offset giving the minimum χ^2 is assumed as the best. The minimum was confirmed at the position (Δcol; Δmag) = (0; 0).

4.5.2 Results

In Figure 4.8 we show the SFR, the the age–metallicity relation (AMR) and the cumulative mass fraction of Canes Venatici II as a function of time with their associated errors. The bulk of the star formation of Canes Venatici II occurred at old epochs and appears to be characterised by one burst of SFH, which took place $\sim$ 13.5 Gyr ago. The initial episode of star formation lasted until roughly 13 Gyr ago, so the width of the burst is $\sim$ 0.5 Gyr. CvnII is a metal poor system, like Boötes I. The mean metallicity of the solution is [Fe/H] = -2.00 $\pm$ 0.2. This value appears to be in agreement with that measured spectroscopically [Fe/H] = -2.21 $\pm$ 0.05 (Kirby et al., 2011).

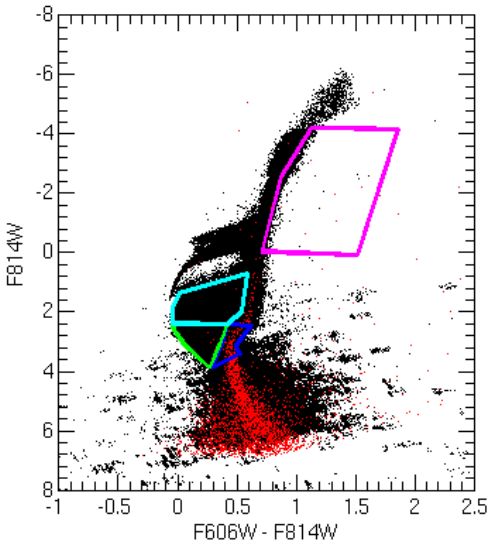

Figure 4.7. Regions of the CMD (bundles) used for gridding. Bundles are shown overplotted on the observed CMD (in red) and on the synthetic CMD (in black) used as an input model for the SFH derivation.

Figure 4.9 presents a comparison between the observed CMD and a best-fit CMD (left and central panels). The latter was derived by extracting random stars from the model CMD used to derive the solution, in such a way that each simple population contributes proportionally to the calculated SFR. Two bundles used to derive the solution have been superimposed on the CMDs. The right panel shows the residual Hess diagram, in units of Poisson error, which supports the good agreement between the observed and the best-fit CMD.

4.6 Duration of the Main Star Formation Episode of Canes Venatici II

As well as for Boötes I we tried to determine the oldest age at which star formation occurred in CvnII and the real duration of the first, main star formation episode. The process is the same as described in section 3.8 for Boötes I.

Figure 4.10 shows a cubic fit to the FWHM of the solutions, $FWHM_{rec}^{mock}$, as a function of the input ones, $FWHM_{in}^{mock}$ for Canes Venatici II.
If the actual SFH of the galaxy were well described as a Gaussian profile, its FWHM could be inferred by interpolating in this fit.
The case of Canes Venatici II is a bit more complicated because its $FWHM_{rec}^{obs}$ does not interpolate the fit, even if it is inside the error bars. We can therefore estimate a value of $FWHM_{in}^{obs} = 100$ Myr for CvnII.
We will adopt this value for the forthcoming discussion.

4.7 The Globular Clusters – Ultra-Faint Dwarfs connection: Canes Venatici II

For many decades, Globular Clusters (GCs) have been considered the simplest possible stellar populations, made up of stars located at the same distance, formed at the same epoch and sharing exactly the same chemical composition. For such a reason, Galactic GCs have been considered the prototype of Simple Stellar Populations (SSPs), and hence largely used as a benchmark for stellar models and for population synthesis tools lately used for studying far, unresolved galaxies. However, in this last decade our view of these stellar systems is drastically changed as a consequence of the discovery of a very complex chemical patterns among stars hosted by the same cluster. More in detail, multi-fibers spectroscopy has provided plain evidence of the fact that, within stars in a given GC, large star-to-star variations in the light elements (such as C, N, O, Na, Al, and Mg) do exist (e.g. Carretta et al. 2009, and Gratton et al. 2012

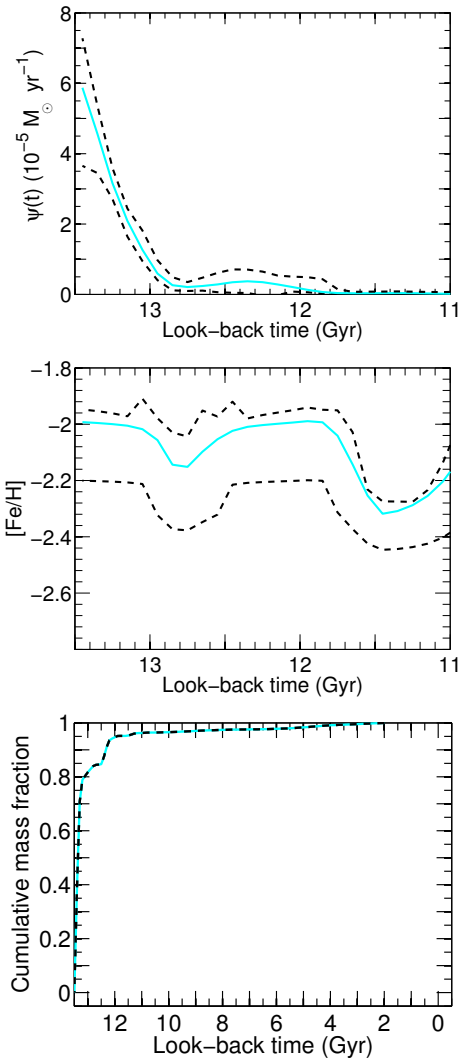

Figure 4.8. *From top to the bottom:* the SFH, metallicity and cumulative mass function as a function of look-back time. Continuos line shows the solution, dashed lines show 1σ error bar.

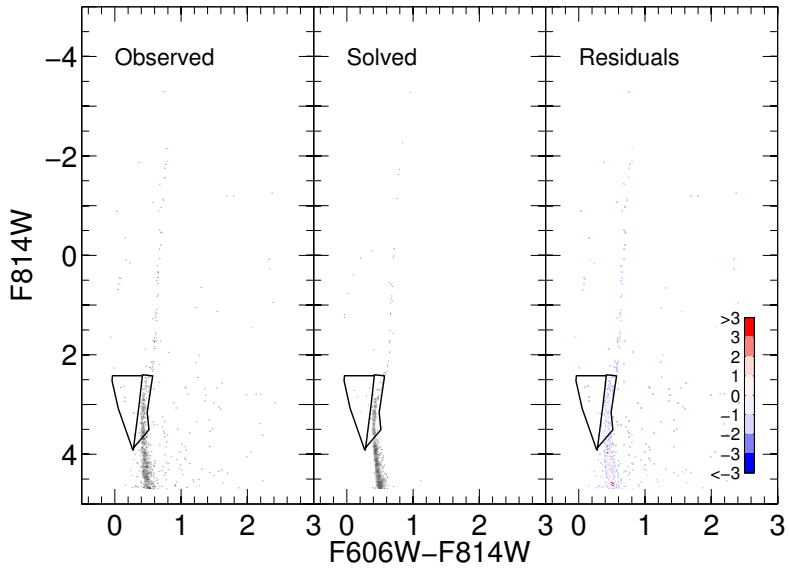

Figure 4.9. Observed *(left panel)*, calculated *(central panel)*, and residual Hess diagram*(right panel)* CMDs. The calculated CMD has been built using IAC-star with the solution SFH of CvnII as input. The black lines mark the position of two bundles adopted to derive the solution. The residuals are in units of Poisson uncertainties.

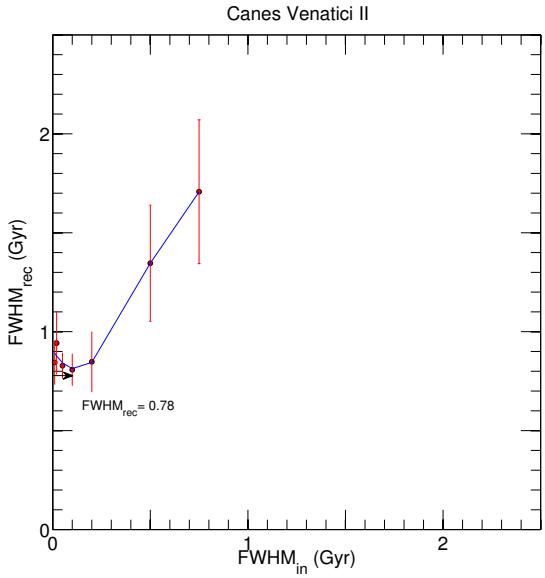

Figure 4.10. A cubic fit to the data is shown, together with the FWHM value measured in the real data solution ($FWHM_{rec}^{obs}$) and the corresponding real value inferred using the fit ($FWHM_{in}^{obs}$). The error bar are calculated as a 1σ error.

and reference therein). The most important signature of the presence of distinct sub-populations is the existence of the O-Na anti-correlation, as well as C-N and N-O anti-correlations.

These peculiar chemical patterns can not be due to evolutionary effects or to surface pollution being observed with the same properties in both giants and dwarf stars. Therefore, these spectroscopic evidence points out that a significant fraction of the stars presently evolving in these Galactic GCs actually formed from matter that has been processed via high-temperature proton captures (Cassisi & Salaris 2014 and references therein). Our current view of Galactic GCs is that they host a population of stars characterized by standard light-elements abundance (i.e. O- and C-rich, Na- and N-poor) the so called first generation (FG), and by a second generation(s) (SG) of stars showing peculiar chemical patterns (i.e. O-, C-depletion, and Na-, N-enhancement).

From a photometric point of view, recent photometric analyses have shown that the colour-magnitude diagram of an increasing number of GCs shows the presence of well-defined, distinct sequences of stars, running from the bottom of the main sequence (MS) up to the red giant branch (RGB); which, once cross-correlated with the spectroscopical measurements appear to correspond to stellar populations with different light elements abundances and helium enhancements (Milone et al. 2012a; Piotto et al. 2007, and references therein). Accurate UV/optical photometric surveys of Galactic GCs have provided a sound evidence of the fact that UV photometry allows to trace the various sub-populations much better than the traditional optical photometric bands (Bellini et al. 2010, 2013; Milone et al. 2010, 2012b, 2013 ; Piotto et al. 2012, 2013) and do so across the whole color-magnitude diagram, from the main sequence (MS) all the way to the horizontal branch (HB). As demonstrated by Sbordone et al. (2011) and Cassisi et al. (2013), this occurrence is due to the fact that the UV photometric bands properly sample the UV portion of the spectral energy distribution (SED) that is hugely affected by the absorption features related to the presence of CN and NH molecules whose abundance is obviously related to the peculiar chemical patterns observed in second generation stars. The definition of a suitable pseudo color such as the photometric index, $c_{U,B,I} = (U - B) - (B - I)$ (Monelli et al. 2013; Milone et al. 2015), appear a quite powerful tool for tracing the presence of distinct sub-populations by using a photometric dataset. This methodological approach has been already extensively used in many investigations on Galactic GCs, and it is at the basis of the "The Hubble Space Telescope UV Legacy Survey of Galactic Globular Clusters" (Piotto et al., 2015) to which some members of our group participate.

We decided to apply - for the first time - this technique to eventually trace

the presence of distinct sub-population in an ultra-faint dwarf galaxy. Ultra-faint dwarf galaxies are considered the fossils of the building blocks which in the past contributed to the build up of massive galaxies such as the Milky Way. So, to probe the existence of multiple stellar populations in these ancient stellar systems would be extremely important in order to shed light on the possible link between ultra-faint dwarfs and Galactic GCs. For instance, this would help in understanding if (and eventually to what extent) many Galactic GCs have an extragalactic origin. UFD galaxies appears to be dark-matter dominated, whereas all observational measurements consistently reveal that Galactic GCs are - at least at present - dark-matter free. Since, we have no clear clues on how, actually, the distinct sub-populations form in the early phase of the life of a GC, the discovery of multiple populations in a UFD could indicate that the presence of a diffuse dark matter halo could play a role in the multiple population phenomenon.

We have collected deep observations in F606W and F814W of Canes Venatici II (see Table 2.4) with the ACS@HST, but they are not enough to define a photometric index capable to disentangle the multiple stellar populations. For this reason, we propose to complete the existing F606W and F814W data with photometry in the Sloan *u'* filter at Gran Telescopio CANARIAS (GTC13-17A; IP: Sara Murabito) and define a new photometric index $c_{u',F606W,F814W}$. The resulting pseudo-CMD would show broadened or multimodal red giant branches (RGBs) in the case of presence of two or several distinct sub-populations in the UFD under scrutiny.

4.7.1 Data reduction

The GTC data consist in a total of 17100 seconds in the Sloan *u'* filter obtained with OSIRIS. In order to have a good sampling of stars for multi-population detection is necessary to reach the base of RGB located at 23 mag in the F814W filter. This corresponds to mag 24.5 in the *u'* band (obtained using a synthetic CMD composed by a stellar population of 13.5 Gyr and [Fe/H]= -2.27).

The pre-reduction was done using IRAF and essentially consists in overscan and bias subtraction and in flat field correction (see Appendix B). The PSF photometry has been obtained with DAOPHOT following the steps described in Section C.2. Figure 4.11 show the combined image of ccd2 in which we performed the photometry. During the observations we placed the center of the galaxy in the center of ccd 2, so we are sure the whole galaxy lie in this ccd.

From the OSIRIS manual (Cabrera-Lavers, 2014), the photometric transfor-

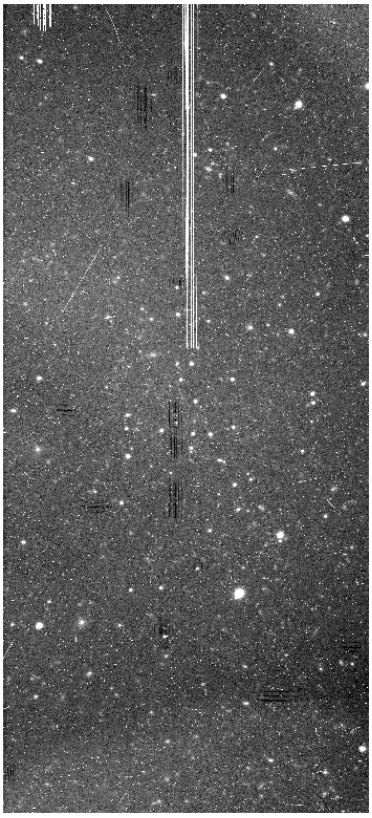

Figure 4.11. Combinated image of ccd 2 of OSIRIS in which we performed the photometry.

mation equation (with an arbitrary zeropoint of 25 magnitudes) for u' is:

$$u'-u'_0 = -0.797(\pm 0.053) - 0.071(\pm 0.023)(u_0-g_0) \tag{4.1}$$

in which we change the g Sloan filter with F606W filter. Figure 4.12 shows the transmission curve of Sloan g filter with OSIRIS@GTC and F606W filter with ACS@HST. The Sloan g filter (λ_{cen}= 4814.95 Å) is bluer than the F606W ACS filter (λ_{cen}= 5947.37 Å) but this does not affect the calibration because what we are interested in seeing is the structure of the RGB.

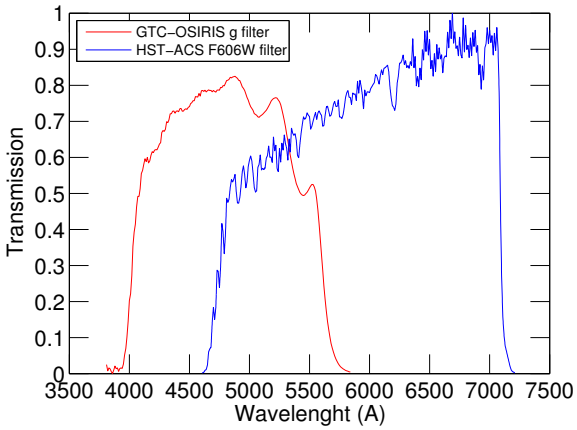

Figure 4.12. Transmission curve of Sloan g filter at GTC and F606W filter at HST.

We have matched the ACS photometry with the OSIRIS photometry using DAOMATCH and DAOMASTER. We focused only in the RGB stars ($0.4 < (F606W - F814W) < 0.8$ and $19 < F814W < 24.2$), since the GTC data reach to the base of RGB. Figure 4.13 show a zoom in the RGB region of CMD. The stars in red (only 46) represent the RGB stars in common between the two photometries. The total number of RGB stars observed with the ACS is 165 so the stars in common represent $\sim 27,9\%$ of the total. The other 119 stars have not been identified with OSIRIS. Maybe the problem is that those stars not observed with OSIRIS might be much dimmer in u' than expected.

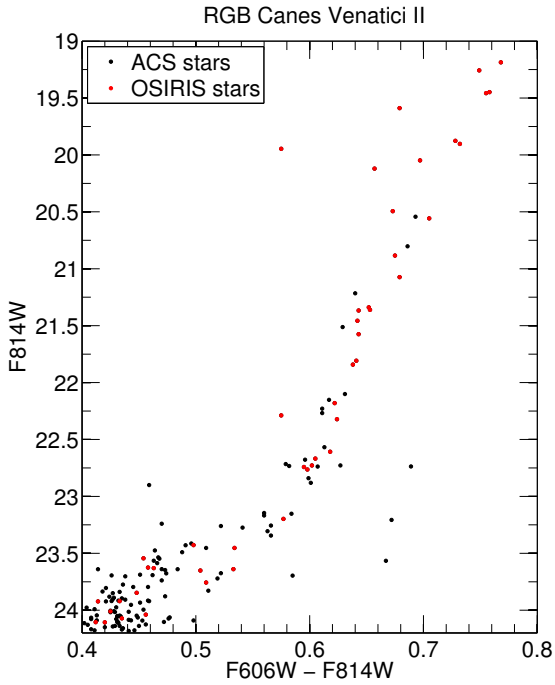

Figure 4.13. Comparison between ACS and OSIRIS photometry in the RGB region. The stars in red (only 46) represent the RGB stars in common between the two photometries.

To identify visually this missing stars we have selected their coordinates from the file obtained from the match and we have displayed them on Figure 4.11. Figure 4.14 shows a zoom of the central region of Figure 4.11 where most of the missing stars are located. We can note that the problem of these stars not observed with OSIRIS not depends on the region where they are located (e.g. are not near a saturated or very large cosmetic failure of the CCD).

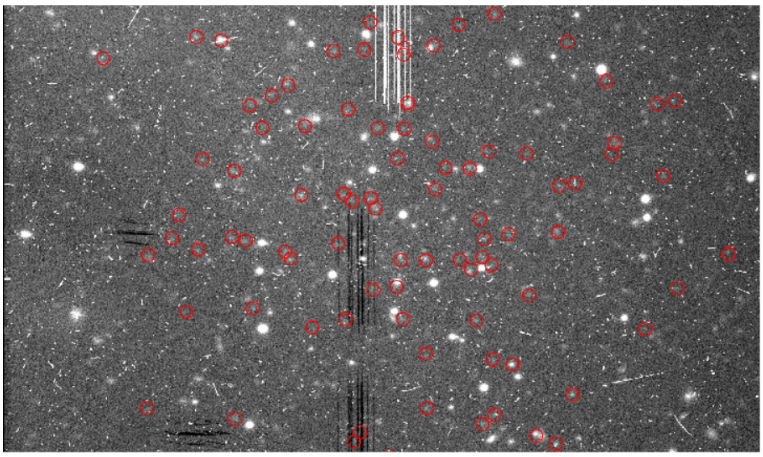

Figure 4.14. A zoom of the region where "missing stars" are located.

We defined a new photometric index, $c_{u',F606W,F814W} = (u' - F606W) - (F606W - F814W)$ which could be useful for tracing the presence of distinct sub-populations. In fact, we have tested this new index in a combination of HST and ground data observation of the GC NGC288 with positive detection of multiple populations in the RGB.

Figure 4.15 shows the zooms in the RGB regions of the pseudo-CMDs. The RGBs appear to have a color spread, but the presence of multiple sequences is not evident. Probably this is due to the presence of few stars in this region. Obtaining deep observations in the u' filter is quite difficult with ground based telescopes because good atmospheric conditions and enough integration time are required. This is the deepest observation in u' filter made to date with OSIRIS. We required a seeing of 1.2 arcsec in u' which means a seeing of 1.0 arcsec in r and it was difficult to reach this limit due to weather conditions during observation nights. Furthermore the last block of data has been observed with

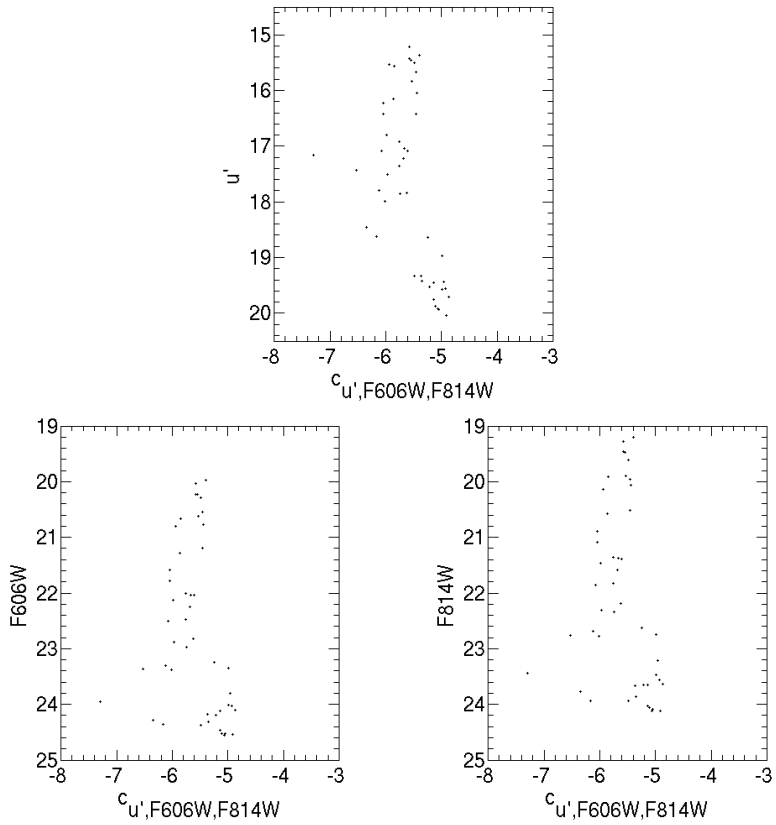

Figure 4.15. Zooms in the RGB regions of the pseudo-CMDs.

haze, which has affected the photometry of GTC data.

As we said before, the reason why some stars are not observed with OSIRIS is that they might be much dimmer in u' than expected. This could be an indicator that we have a group of stars in CvnII with a different pattern in metallicity than the rest of the stars. So, we can not confirm or deny the existence of multiple stellar populations in CvnII or in others UFDs galaxies. What is certain is that further studies are needed in this direction.

4.8 Discussion and Conclusions

We have presented an analysis of the SFH of the ultra-faint dwarf galaxy Canes Venatici II, based on high-precision photometry obtained with the Advanced Camera for Surveys on the *Hubble Space Telescope*.

A deep CMD reaching the oldest main-sequence turnoffs has been obtained. The overlap of isochrones shows that it is an old and metal-poor system. Ground-based photometry suggests that CVn II is composed exclusively of an old ($>$ 10 Gyr) stellar population (Sand et al. 2012; Okamoto et al. 2012).

Recent work has made progress in determining the star formation history (Brown et al. 2014; Weisz et al. 2014a) and chemical abundances (Kirby et al. 2011; Vargas et al. 2013) of this system.

Deep HST/ACS data have allowed us to derive the lifetime SFH of this ultra-faint dwarf galaxy. We have shown that the galaxy experienced a event of star formation at $\sim$ 13.5 Gyr and decreased until stopping $\sim$ 13 Gyr ago, so the width of the burst is $\sim$ 0.78 Gyr.

Based on spectroscopic results, CVn II appears to be dark matter dominated with an $M/L_V = 360^{+380}_{-180}$ (Wolf et al., 2010) and is metal-poor, with $\langle [Fe/H] \rangle$ = -2.21 $\pm$ 0.5 (Kirby et al., 2011). Our results are in agreement with those obtained spectroscopically since the mean metallicity of the solution is [Fe/H] = -2.00 $\pm$ 0.2.

Photometric and spectroscopic observations of the UFD galaxies have shown that they have characteristics similar to Globular Clusters in terms of age and metallicity but not in the number of stars they contain and their surface brightness.

Accurate UV/optical photometric surveys of Galactic GCs have provided a sound evidence of the fact that UV photometry allows to trace the various sub-populations much better than the traditional optical photometric bands (Bellini et al. 2010, 2013; Milone et al. 2010, 2012b, 2013 ; Piotto et al. 2012, 2013) and do so across the whole color-magnitude diagram, from the main sequence (MS) all the way to the horizontal branch (HB).

We decided to apply - for the first time - this technique to eventually trace the presence of distinct sub-population in CvnII. We have matched the ACS photometry with the OSIRIS photometry and we have define a new photometric index $c_{u',F606W,F814W}$. The resulting pseudo-CMD seems to show a color spread in the RGB, but the presence of multiple sequences is not evident.

5

Leo IV

In this chapter we will focus on the analysis of the ultra-faint dwarf galaxy Leo IV. The data comes from WFC@ACS at the Hubble Space Telescope. The resulting CMD and the estimate of age and metallicity using isochrone fitting are discussed in Section 5.3. The SFH of Leo IV is considered in Section 5.5.

5.1 Introduction

Of the newly discovered MW satellites, Leo IV ($M_V = -5.8 \pm 0.4$ mag, $r_h \sim$ 206 pc; de Jong et al. 2010) is among the least studied, despite several signs that it is an intriguing object. Leo IV appears to be dominated by an old and metal-poor stellar population (de Jong et al., 2008). There are few age estimates for Leo IV. Brown et al. 2012, using synthetic CMDs, found that Leo IV's main population is 13.7 Gyr old, approximately as old as M92, though they could not rule out a younger population that is up to 2 Gyr younger than the main population. Okamoto et al. 2012 derived an age of 13.7 Gyr based on fits of Padova isochrones to Leo IV's CMD. By overlaying M92 CMD fiducials onto Leo IV's CMD, they found the two to be approximately the same age. Sand et al. 2010, using a synthetic CMD method, derived an age of 14 Gyr for the main population of Leo IV, while also finding "some latitude" for a mixture of populations.

A search for variable stars was recently performed by Moretti et al. (2009), who used the average magnitude of three RR Lyrae stars to find a distance modulus of (m - M) = 20.94 ± 0.07 mag, corresponding to 154±5 kpc.

Based on Keck/DEIMOS spectroscopy of 18 member stars, Leo IV has one of the smallest velocity dispersions of any of the new MW satellites, with $\sigma =$

3.3 ± 1.7 km s^{-1} (Simon & Geha, 2007). They performed medium resolution spectroscopy identifying 18 red giants and horizontal branch stars as Leo IV members based on radial velocity. The mean metallicity was found to be [Fe/H] = -2.31 ± 0.10. Kirby et al. 2008 reanalyzed that study's data to produce a much lower value of -2.58 ± 0.08 using 12 of the original 18 stars. Finally, Kirby, employing an updated methodology (Kirby et al., 2009), once more reanalyzed all twelve of the stars reanalyzed in Kirby et al. 2008, excepting one whose measurements fall short of the S/N requirements for the updated method. The reanalysis yields [Fe/H] = -2.54 ± 0.07 for Leo IV.

Recently, the MW satellite Leo V ($M_V = -4.3 \pm 0.3$) has been discovered, separated by only ∼2.8^o on the sky and ∼40 km s^{-1} from Leo IV (Belokurov et al., 2008). With a Leo V distance of ∼180 kpc, this close separation in phase space led Belokurov et al. (2008) to suggest that the Leo IV/Leo V system may be physically associated. This argument was bolstered by Walker et al. (2009) who spectroscopically identified two possible Leo V members 13 arcmin from the satellite's center (Leo V's r_h is ∼0.8 arcmin) along the line connecting Leo IV and Leo V, suggesting that Leo V is losing mass. A recent analysis by de Jong et al. (2010) of two 1 deg^2 fields situated between Leo IV and Leo V shows tentative evidence for a stellar "bridge" between the two systems with a surface brightness of ∼32 mag arcsec^{-2}.

A summary of the fundamental parameters of LeoIV is show in Table 5.1.

5.2 Dataset

The data of Leo IV come from MAST archive and distribution center for HST data, which distributes scientific data, calibration and engineering to HST users and to the astronomical community in general. The data were taken in 2012 January using the F606W and F814W filters on ACS (GO-12549; PI: Brown). Table 2.4 list the coordinates and the total exposure time in each filter.

As well as for CvnII the data has been pre-reduced using a specific calibration pipeline by the HST team. The details of the two packages **calacs** and **AstroDrizzle** are described in Section 4.2.

The photometry of Leo IV was obtained with DOLPHOT (see Section C.3) using the `flc.fits/drc.fits` images.

5.3 CMD of Leo IV

We present the CMD of Leo IV in Figure 5.3. Only objects with $\sigma \leq 0.1$, $chi \leq 1.2$ and $|sharp| \leq 0.25$ were considered stars. The magnitudes have been

Parameter	Value	References[a]
RA (hhmmss)	11 32 57	(1)
Dec (^{o} ' ")	-00 32 00	(1)
Galactic longitude, l	256.4^o	(1)
Galactic latitude, b	56.5^o	(1)
Position angle	$121^o \pm 9^o$	(2)
Ellipticity ϵ	0.49±0.11	(2)
E(B - V)	0.026	(3)
$(m-M)_0$	20.94±0.07	(4)
Heliocentric distance (kpc)	154±5	(4)
Heliocentric velocity (km s^{-1})	132.3±1.3	(5)
Apparent magnitude V	15.1±0.4	(3)
Half-light radius r_h (pc)	206±37	(2)
Absolute magnitude M_V	-5.8±0.4	(2)
Half-light radius r_h (arcmin)	4.6±0.80	(2)
Barionic mass $M_\star$ ($10^6 M_\odot$)	0.019	(5)
$[Fe/H]$	-2.54±0.07	(6) (7)

[a] References: (1) Belokurov et al., 2007; (2) de Jong et al., 2010 ; (3) McConnachie, 2012; (4) Moretti et al., 2009; (5) Simon & Geha, 2007; (6) Kirby et al., 2008; (7) Kirby et al., 2011.

Notes. The stellar mass is computed from the integrated V-band luminosity and assumes $M \odot / L \odot = 1$.

Table 5.1. Fundamental parameters of Leo IV.

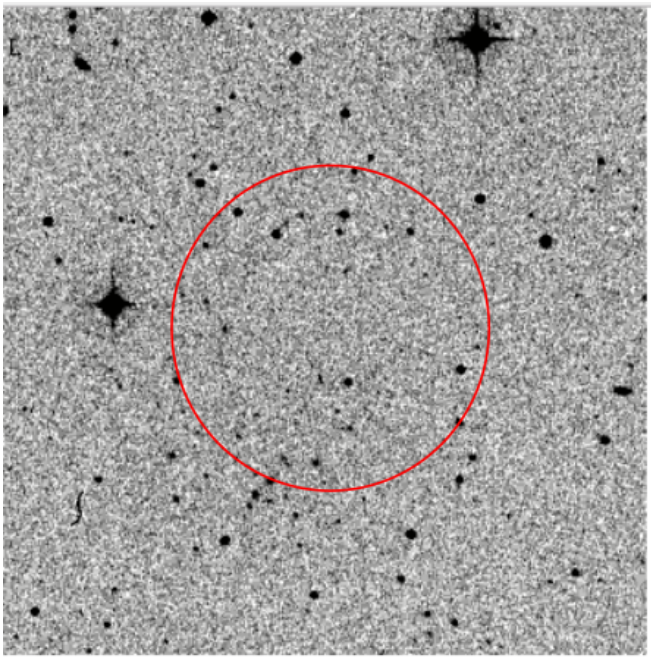

Figure 5.1. Field of view ($10' \times 10'$) of Leo IV. The galaxy is located at the center of the red circle. Because of the low surface brightness of the galaxy, it cannot be distinguished from the foreground stars.

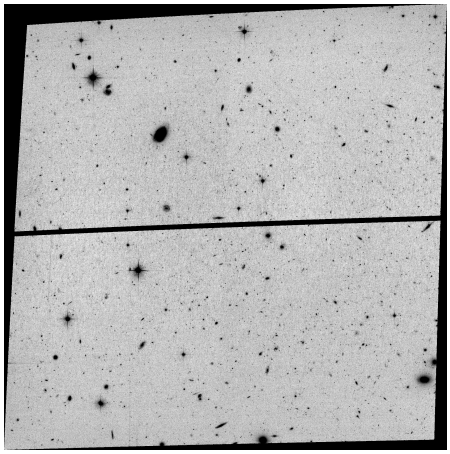

Figure 5.2. The WFC@ACS field of Leo IV in the F814W filter. The field of view is $202'' \times 202''$, the pixel scale is $\sim$0.05"/pixel and the surface brightness of the galaxy is 27.5 mag $arcsec^{-2}$ (de Jong et al., 2010).

corrected for distance modulos ($(m-M)_0 = 20.94$) and extinctions ($A_{F606W} = 0.024$ and $A_{F814W} = 0.015$). It is possible to note that the CMD of Leo IV is very similar to the CvnII one. Two isochrones with Z = 0.0001 and 12.5 and 13.5 Gyr belong to the BaSTI library (Pietrinferni et al., 2004) are overlaid. The fiducial sequence of MS and RGB is quite well reproduced by the isochrones, but it is not the same for the TO and SGB.

5.4 Completeness Tests

The completeness tests were performed using the procedure described in Section D.2 and it consists in adding synthetic stars to the individual images and repeating the photometric analysis identically as for the real data.
In the case of Leo IV, 2,386,130 stars were simulated in the chip. We injected artificial stars with random colors and magnitudes selected to cover the whole observed CMD.

Figure 5.4 show the $\Delta mag = mag_{in} - mag_{out}$ of the artificial stars for the two bands, as a function of the input magnitude. The completeness of Leo IV is shown in Figure 5.5.

5.5 The SFH of Leo IV

We derived the SFH of Leo IV using the IAC method described in Appendix D. The accuracy of the result depends on the depth of the CMD of the studied galaxy. To obtain the SFH, the regions of the CMD more sensitive to the age, as the MS TO, are used.

5.5.1 CMD model

The synthetic CMD was created using IAC-star (Aparicio & Gallart, 2004) and was built with the same inputs of Boötes I and CvnII. The sCMD contains 10^7 stars with a constant SFR between 2 and 13.5 Gyr and a uniform metallicity distribution between Z = 0.00001 and Z = 0.001, corresponding to [Fe/H] = -3.28 and -1.27, respectively. The range in metallicity was selected in order to cover all the metallicities of the stars in this galaxy (Kirby et al. 2008, 2011). We chose the BaSTI evolutionary library (Pietrinferni et al., 2006), a Kroupa IMF (Kroupa, 2001), and a binary fraction of 30%. The observational effects were simulated in the synthetic CMD with the routine *obsersin*, as described in Section D.2. Thus, the IAC-pop/MinnIAC (Aparicio & Hidalgo 2009; Hidalgo et al. 2011) were applied to derive the accurate SFH for Leo IV.

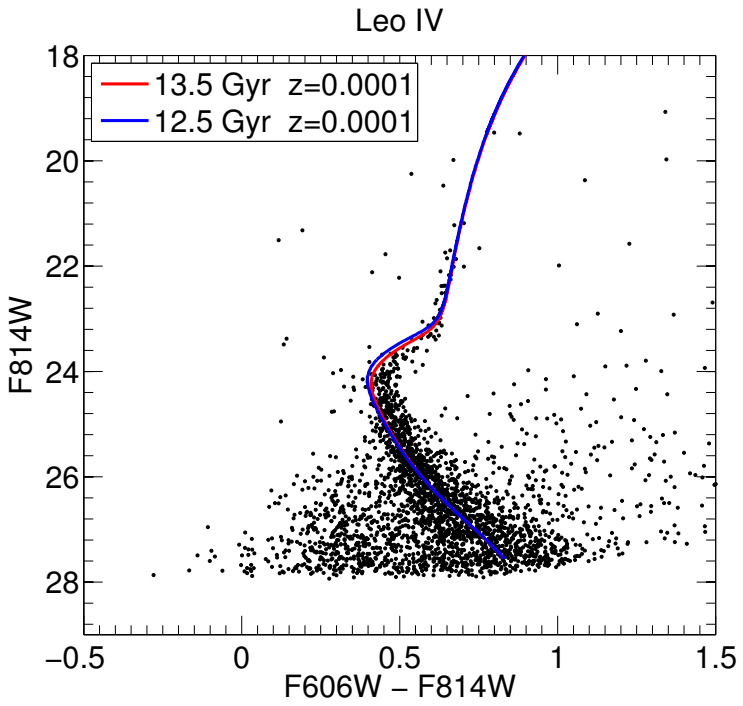

Figure 5.3. CMD of Leo IV. This CMD has been decontaminated using the procedure described in the text. Two isochrones with Z = 0.0001 and 12.5 and 13.5 Gyr belong to the BaSTI library (Pietrinferni et al., 2004) are overlaid.

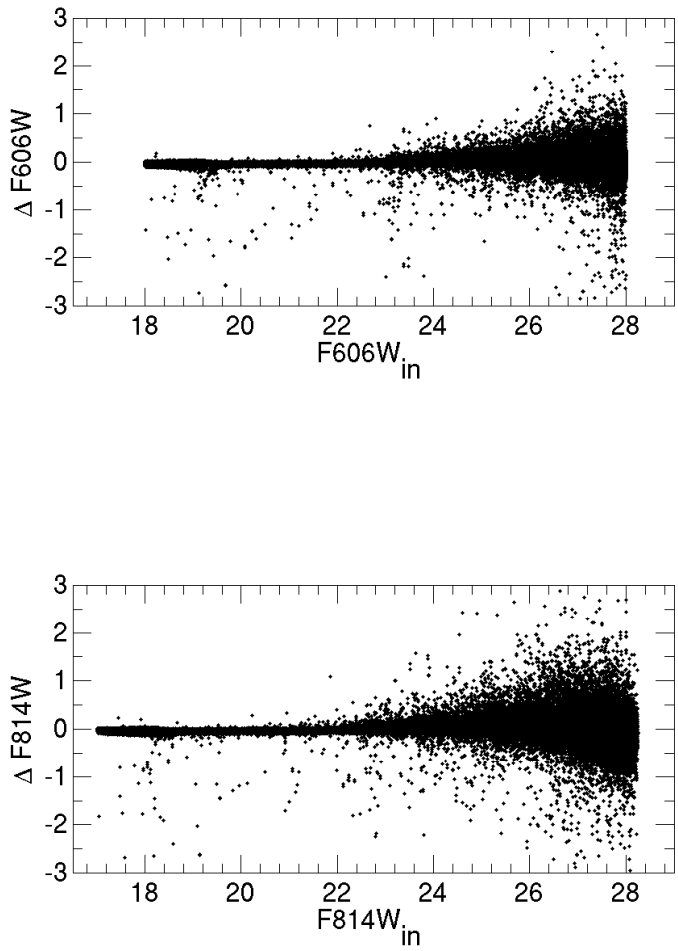

Figure 5.4. Difference $\Delta mag = mag_{in} - mag_{out}$ for synthetic stars as a function of the input magnitude.

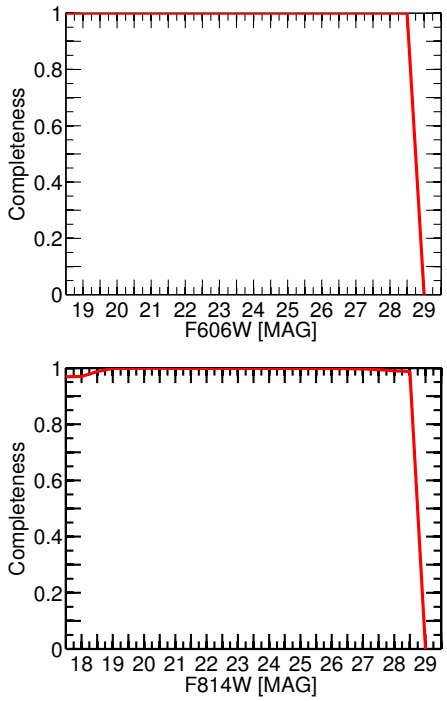

Figure 5.5. Result of the false star tests for Leo IV, in the F606W *(upper panel)* and F814W *(lower panel)* filters.

The basic age and metallicity bins defining the simple stellar populations (SSPs) used are as follows:

- Age: [2 5 7 9 10:0.25:13.5]$\times 10^9$ years
- Metallicity: [0.00001 0.00003 0.00005 0.0001].

These numbers define the boundaries of the bins, not their centers. Therefore, they fix $18 \times 3 = 54$ simple populations. These values were selected according to the age and metallicity resolution tests presented in Section 3.6.2.
Figure 5.6 shows the bundles used, overplotted on the sCMD.

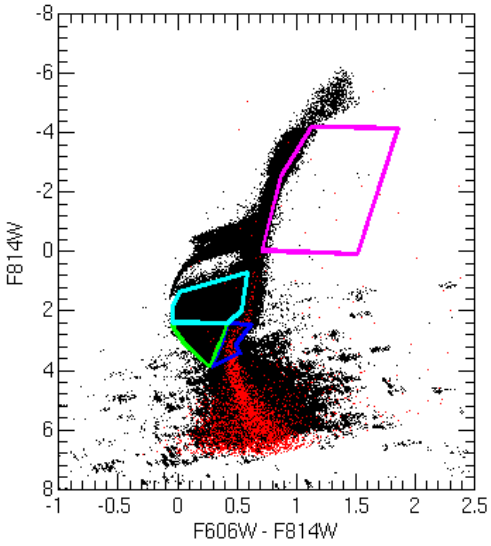

Figure 5.6. Regions of the CMD (bundles) used for gridding. Bundles are shown overplotted on the observed CMD (in red) and on the synthetic CMD (in black) used as an input model for the SFH derivation.

To minimize the uncertainties of external parameters (distance, reddening and photometry zero point), the SFH is derived for different offsets in color and magnitude applied to the observed CMD (oCMD). The offset giving the

minimum χ^2 is assumed as the best. The minimum was confirmed at the position (Δcol; Δmag) = (0; 0).

5.5.2 Results

Figure 5.7 summarizes the main results by comparing the SFR as a function of time (top), the age–metallicity relation (middle), and the cumulative mass function (bottom).

Figure 5.8 presents a comparison between the observed DAOPHOT CMD and a best-fit CMD (left and central panels), represented as Hess diagrams. The bundles used to derive the solution have been superimposed on the observed CMD. We find satisfactory agreement in all the main evolutionary phases.
The bulk of the star formation of Leo IV occurred at old epochs and appears to be characterised by one burst of SFH, which took place $\sim$ 13.5 Gyr ago. The initial episode of star formation lasted until roughly 12.5 Gyr ago, so the width of the burst is $\sim$ 1 Gyr.

Leo IV is a metal poor system, like Boötes I and CvnII. The mean metallicity of the solution is [Fe/H] = -2.52 $\pm$ 0.15. This value appears to be in agreement with that measured spectroscopically [Fe/H] = -2.54 $\pm$ 0.07 (Kirby et al., 2011).

5.6 Duration of the Main Star Formation Episode of Leo IV

As we have already said before it is particularly important to determine the oldest age at which star formation occurred in each of our galaxies and the real duration of the first, main star formation episode. The process we used is the same used for Boötes and CvnII and is described in section 3.8.

Figure 5.9 shows a cubic fit to the FWHM of the solutions, $FWHM_{rec}^{mock}$, as a function of the input ones, $FWHM_{in}^{mock}$ for Leo IV. If the actual SFH of the galaxy was well described as a Gaussian profile, its FWHM could be inferred by interpolating in this fit, which gives $FWHM_{in}^{obs}$ = 1.72 Gyr for Leo IV.

5.7 Discussion and Conclusions

We used HST/ACS observations to derive the SFH of the UFD galaxy Leo IV. A deep CMD reaching the oldest main-sequence turnoffs has been obtained. The overlap of isochrones shows that it is an old and metal-poor system. Exhaus-

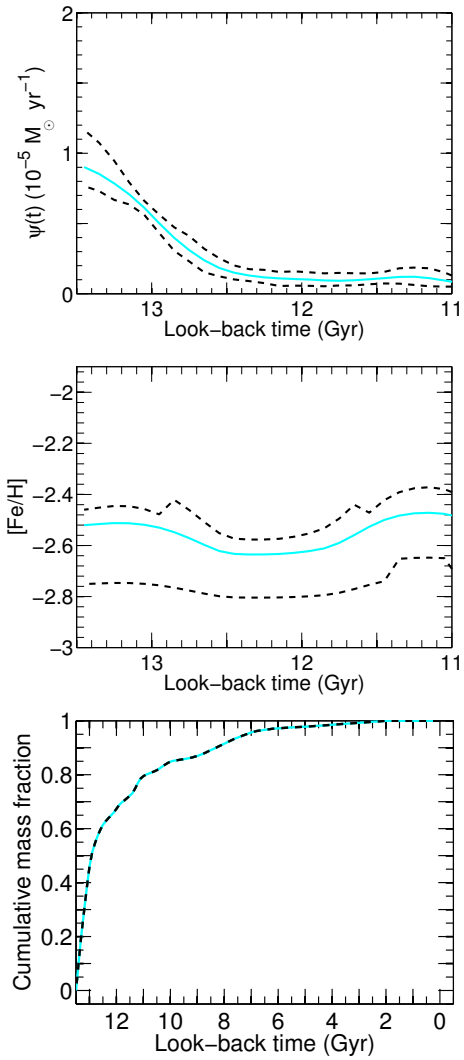

Figure 5.7. *From top to the bottom:* the SFH, metallicity and cumulative mass function as a function of look-back time. Continuos line shows the solution, dashed lines show 1σ error bar.

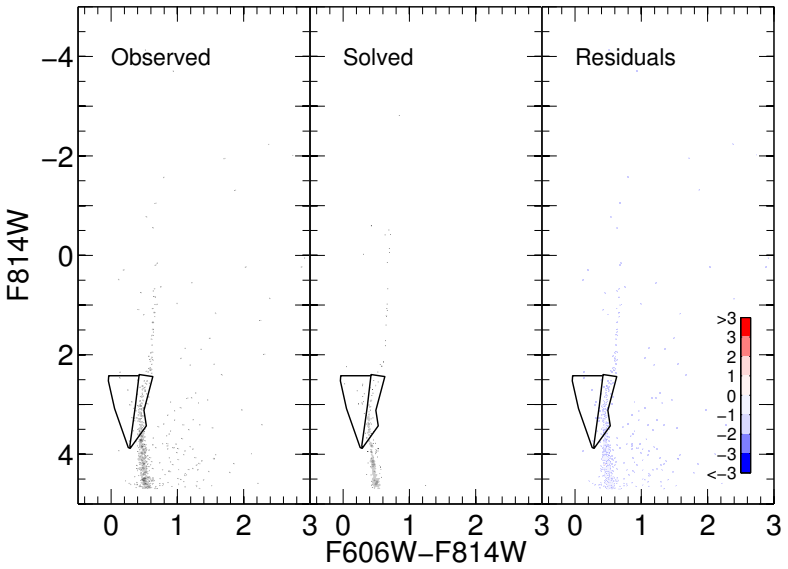

Figure 5.8. Observed *(left panel)*, calculated *(central panel)*, and residual Hess diagram *(right panel)* CMDs. The calculated CMD has been built using IAC-star with the solution SFH of Leo IV as input. The black lines mark the position of two bundles adopted to derive the solution. The residuals are in units of Poisson uncertainties.

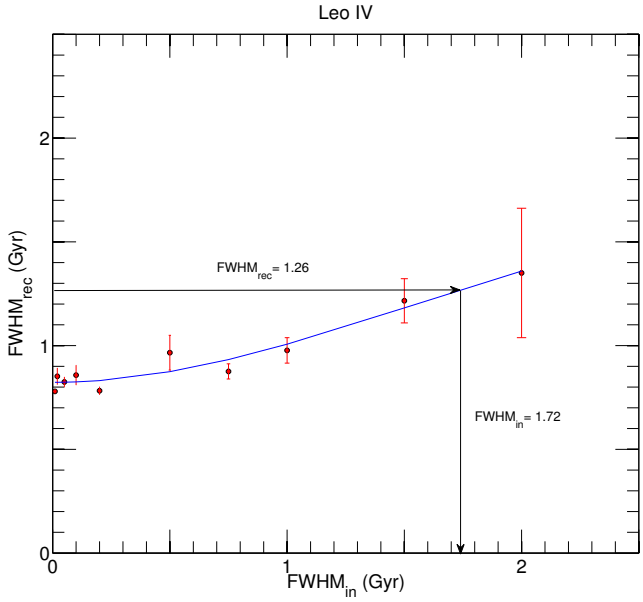

Figure 5.9. A cubic fit to the data is shown, together with the FWHM value measured in the real data solution ($FWHM_{rec}^{obs}$) and the corresponding real value inferred using the fit ($FWHM_{in}^{obs}$). The error bar are calculated as a 1σ error.

tive crowding tests have been performed in order to properly characterize the observational effects.

The SFH for the entire lifetime of the galaxy has been obtained. The solution shows that the SFH of Leo IV is dominated by an old, main episode with maximum occurring $\sim$ 13.5 Gyr ago and a duration estimated in 1.72 Gyr (FWHM, see Section 5.6). This means that the star formation ended close to $\sim$ 11.8 Gyr ago, after the end of the epoch of the reionization fixed at $\sim$ 12.77 Gyr (Becker et al. 2001). The ultraviolet (UV) cosmic reionization or others local causes, such as intense galactic winds and SNe feedback, could be the causes that led to the end of star formation in Leo IV.

Leo IV is a very metal poor system. The mean metallicity of the solution is [Fe/H] = -2.52 $\pm$ 0.15. This value falls within the errors of the calculated value measured spectroscopically by (Kirby et al., 2011) that is [Fe/H] = -2.54 $\pm$ 0.07.

Sand et al. (2010) presented MMT/Megacam imaging of the Leo IV dwarf galaxy in order to investigate its structure and star formation history, and to search for signs of association with the recently discovered Leo V satellite. They determined that Leo IV is consistent with a single age ($\sim$14 Gyr), single metallicity ([Fe/H] $\sim$ -2.3) stellar population, although they cannot rule out a significant spread in these values. Studying both the spatial distribution and frequency of Leo IV's "blue plume" stars reveals evidence for a young ($\sim$2 Gyr) stellar population which makes up $\sim$2% of its stellar mass. The old population is consistent with the emerging picture that the faintest MW satellites are "reionization fossils" (e.g., Ricotti & Gnedin 2005; Gnedin & Kravtsov 2006), who formed their stars before reionization and then lost most of their baryons due to photoevaporation. The apparent sprinkling of young stars begs the question of what has enabled Leo IV to continue forming stars at a low level. This sprinkling of star formation, only detectable in this deep study, highlights the need for further imaging of the new Milky Way satellites along with theoretical work on the expected, detailed properties of these possible "reionization fossils".

6

Analysis of Global Features of Boötes I, Canes Venatici II and Leo IV

In this chapter we will analize some global features of the three galaxies as if they can be considered true fossils of the Reionization Era (Section 6.1), the supernovae feedback (Section 6.2) and finally the mass-metallicity relationship (Section 6.3).

6.1 Fossils of the Reionization Era

It is possible that some galaxies form stars before reionization and then not evolve much in terms of their total and stellar mass, with their stellar populations evolving mostly passively. Such galaxies would then represent fossils of the reionization era, and studying their properties could provide a direct window into the early, pre-reionization stages of galaxy formation. As such, it would be extremely interesting to identify and study this population in the Local Group.

In 2005, Ricotti & Gnedin have proposed that dwarf galaxies of the Local Group (and, by implication, all other dwarf galaxies in the universe) formed in three different evolutionary paths:

1. *True fossils* formed most of their stars in the pre-reionization era and have had little (say, $< 30\%$) star formation since then.
2. *Polluted fossils* started as true fossils but had substantial episode(s) of subsequent star formation as they continued accreting mass and were tidally

shocked during the formation of the parent galaxy halo.

3. *Survivors* started forming stars mostly after reionization.

The best candidates for "fossil galaxies" are UFDs ($L < 10^5 L_\odot$) discovered in the past decade (Belokurov et al. 2007, 2010; Drlica-Wagner et al. 2015; Koposov et al. 2015a) and some old globular clusters (GCs) (Ricotti 2002; Katz & Ricotti 2013, 2014). Most UFDs contain only old, metal-poor stars and appear to have simple star formation histories (Brown et al. 2012, 2014), making them excellent candidates for probing chemical and dynamical signatures of the first generations of stars.

When considering the results of the retrieved SFHs as well as data in literature, the question arising is whether Boötes I, Cvn II and Leo IV are *true fossil* of the pre-reionization era in the sense introduced in Ricotti & Gnedin (2005): a dwarf that has experienced more than the 70% of its star formation before the end of the reionization and that has a luminosity $L_V < 10^6 L_\odot$. Boötes I, Cvn II and Leo IV satisfy the second condition, since they have respectively a luminosity $L_V = 3.0 \pm 0.6 \times 10^4 L_\odot$, $L_V = 7.9^{+3.4}_{-3.7} \times 10^3 L_\odot$ and $L_V = 8.7^{+4.4}_{-4.7} \times 10^3 L_\odot$ (Martin et al., 2008a). Regarding the first condition, the cumulative mass fraction shows that Boötes I and Leo IV formed 70% of their stellar mass $\sim$ 12 Gyr ago, while CvnII formed 70% of its stellar mass $\sim$ 13 Gyr ago as derived from the SFH (see Table 6.1).

Galaxy	Peak of the SFH (Gyr)	$M_\star$ ($10^6 M_\odot$)	Age for Ψ(t)=0.7 (Gyr)
Boötes I	13.5	0.029	12.3
Canes Venatici II	13.5	0.0079	13.3
Leo IV	13.5	0.019	11.8

Table 6.1. Properties of the galaxies. Column 1: name of the galaxy. Column 2: the peak of the SFH. Column 3: total stellar mass from McConnachie (2012). Column 4: age at which the cumulative SFH Ψ(t) reaches 70%.

In Sections 3.8, 4.6 and 5.6, we have been able to confine the initial event of star formation to 1.45 Gyr for Boötes I, to 0.78 Gyr for Cvn II and to 1.72 Gyr for Leo IV. This means that the star formation ended close to 12.05 Gyr for Boötes I, close to 12.72 Gyr for Cvn II and close to 11.72 Gyr for Leo IV. Keeping in mind that the end of the epoch of the reionization is fixed at $\sim$ 12.77 Gyr (Becker et al. 2001) we can say that the star formation in Cvn II was completed together to the end of the epoch of reionization, while for Boötes I and Leo IV the star formation continued even after the end of the epoch of reionization.

From these facts the three galaxies can anyway be classified a *true fossil* of the pre-reionization era. Moreover, the work by Ricotti & Gnedin (2005) corroborates the hypothesis according to which internal feedback, such as photoheating by the stars inside the galaxy and SNe explosions, have been the principal causes of suppression of star formation, since true fossils are the result of feedback processes in action prior to reionization. So that, they are expected to evolve passively after the end of the reionization era because of the exaustion of gas.

In order to investigate this hypothesis we will calculate, as outlined in Hidalgo et al. (2011), the mechanical luminosity of the SNe released during the main star formation episode.

6.2 Supernovae Feedback

The SFH obtained for our galaxies allows us to make a direct estimate of the importance of feedback in Boötes I, Canes Venatici II and Leo IV. To do so, the mechanical luminosity of the SNe produced in the main star formation episode and the mass of the galaxy can be compared with the results of Mac Low & Ferrara (1999). They used models to calculate the conditions for blow-away, partial mass loss, and no mass loss of dwarf galaxies as a function of the baryonic mass of the galaxy and the mechanical luminosity, L_w, of the SNe produced during a central, instantaneous star formation episode. In particulary, in a "blowout", the central SN explosions blow a hole through the galactic gas distribution, parallel to the steepest density gradient (usually along the rotation axis), accelerating some fraction of the gas and releasing the energy of subsequent explosions without major effects on the remaining gas. In a "blow-away", all (or nearly all) of the ambient interstellar medium (ISM) is accelerated above the escape velocity and is lost to the galactic potential well.
We can compute the mechanical luminosity from core collapse SNe (note that STARBURST99 includes all sources of mechanical luminosity).

First we have to calculate the total number of SNe produced in the onset of the star formation using the total stellar mass of each galaxy. This value is different if we assume a minimum progenitor mass for core collapse SNe of 6.5 $M_\odot$ (Salaris & Cassisi, 2005) or, accounting for stellar mass loss, we assume a minimum initial mass of 10 $M_\odot$ for SNe progenitors. Assuming an energy release per SN of 10^{51} erg (Leitherer et al., 1999) and a duration of the initial episode equal to the values of $FWHM_{in}^{obs}$ obtained for each galaxy in Sections 3.8, 4.6 and 5.6, we obtained a total mechanical luminosity released during the old, main episode.

Combining these values of mechanical luminosity with those of the baryonic mass obtained from the SFH solutions, the model results of Mac Low & Ferrara (1999) shown in Figure 6.1 place Boötes I and Canes Venatici II in the blow-away regime, while place Leo IV in the regime of mass loss, but fairly close to the blow-away regime.

Table 6.2 summarize the values calculated for the three galaxies and the regime in which they are placed according to the model of Mac Low & Ferrara (1999).

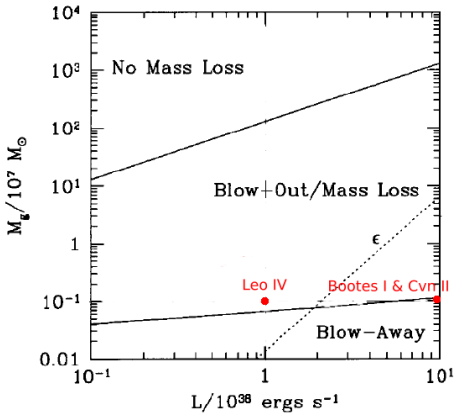

Figure 6.1. Figure from Mac Low & Ferrara (1999). Regions of the gas mass (M_g)-mechanical luminosity of the starburst (L) plane in which blowout or blow-away occurs.

In Boötes I and Cvn II the feedback of SNe would have created outflows that completely blow away the gas, whereas in Leo IV the mass loss by galactic winds is important, but not complete. In other words, Leo IV seems to be massive enough to conserve at least a fraction of its gas against SN feedback. Note that Leo IV has the more extended SFH of the galaxies of this sample, reaching $\sim$ 1.7 Gyr, and a lower total number of SNe. This slower evolution of Leo IV compared with the other galaxies of the sample would have allowed to Leo IV keep a gas reservoir to keep forming stars.

Silich & Tenorio-Tagle (2001) reexamine the efficiency of starbursts in ejecting their newly produced metals and in ejecting their whole ISM from dwarf and normal galaxies, taking into account the pressure caused by the environment in

Galaxy	Total mass	Number of SNe		L_w		Regime	
		6.5 $M_\odot$	10 $M_\odot$	6.5 $M_\odot$	10 $M_\odot$	6.5 $M_\odot$	10 $M_\odot$
Boötes I	0.074×10^6	1.14×10^4	7.42×10^3	2.50×10^{39}	1.62×10^{39}	Blow-away	Blow-away
Cvn II	0.021×10^6	3.29×10^3	2.14×10^3	1.04×10^{40}	6.77×10^{39}	Blow-away	Blow-away
Leo IV	0.009×10^6	1.39×10^3	906.64	2.57×10^{38}	1.67×10^{38}	Blow-out/Mass loss	Blow-out/Mass loss

Table 6.2. The table show the total mass of the galaxies obtained from SFH solution (*second column*), the number of SNe produced in the old episode using a minimum SNe progenitor mass of 6.5 $M_\odot$ (*third column*) or of 10 $M_\odot$ (*fourth column*), total mechanical luminosity released during the old, main episode (*fifth and sixth columns*), and the regime in which they are placed according to the model (*seventh and eighth columns*).

which a galaxy is situated, as well as to the intrinsic rotation of the gaseous component. Their results are in excellent agreement with the results of Mac Low & Ferrara (1999) for galaxies with a flattened, disklike ISM density distribution and a low intergalactic gas pressure ($P_{IGM}/k \leq 1cm^{-3}$ K). It should be underlined however that their sample of galaxies have a DM mass in the range of $6.8\times10^7 M_\odot$ to $9.1\times10^9 M_\odot$, therefore they have much greater mass than UFDs.

6.3 Mass-Metallicity Relationship

Stellar mass and metallicity are two of the most fundamental physical properties of galaxies. Both are metrics of the galaxy evolution process, the former reflecting the amount of gas locked up into stars, and the latter reflecting the gas reprocessed by stars and any exchange of gas between the galaxy and its environment. Understanding how these quantities evolve with time and in relation to one another is central to understanding the physical processes that govern the efficiency and timing of star formation in galaxies.

The average metal content of a galaxy correlates with its mass. More massive galaxies are more metal-rich than less massive galaxies. The relation can be explained by the retention of metals in the galaxies' gravitational potential wells (e.g., Dekel & Silk 1986). High-mass galaxies have deep potential wells that can resist some of the expulsion of gas and metals by supernova winds, stellar winds, and galaxy-scale feedback. Low-mass galaxies lack the gravity to resist these feedback mechanisms. The correlation between metallicity and mass can also be explained by a correlation between star formation efficiency and stellar mass (e.g., Matteucci 1994; Calura et al. 2009; Magrini et al. 2012; Pipino et al. 2013). If massive galaxies evolve quickly, then they can achieve high stellar masses and low gas mass fractions. Consequently, their metallicities will be high. On

the other hand, slowly evolving, low-mass galaxies can have high gas fractions, which dilute the metallicity of both the gas and the stars that form from the gas. Yet another explanation for the mass-metallicity relation is a stellar initial mass function (IMF) that changes with the rate of star formation (Köppen et al., 2007). Because that rate depends on galaxy mass and because the metal yield depends on the masses of stars, a galaxy's metallicity then depends on its stellar mass. Tremonti et al. (2004) showed that the average metallicities of star-forming galaxies in the Sloan Digital Sky Survey (SDSS; Abazajian et al. 2004) correlate strongly with their stellar masses or rotation speeds. As with previous studies, Tremonti et al. interpreted the relation as a progression of a larger effective yield for more massive galaxies. Expressed another way, more massive galaxies lose a smaller fraction of the metals that their stars produce.

The mass–metallicity relation (MZR)- where metallicity was measured in the gas phase- extends down to the mass range of dwarf galaxies as small as a few million solar masses. Mould et al. (1983) and Skillman et al. (1989) showed that dwarf elliptical (dE) and dwarf irregular galaxies (dIrrs) in and around the Local Group (LG) obey an luminosity-metallicity relation (LZR). Garnett (2002) extended the relation to more distant spiral galaxies. Irregular and spiral galaxies obey the same, unbroken relation over 4.5 orders of magnitude in luminosity.

Kirby et al. (2013) measured metallicities from spectra of individual red giants in 15 MW dSphs and seven LG dIrrs as well as from coadded spectra of red giants in 13 M31 dSphs. In contrast to metallicities measured from emission lines, their stellar metallicities were not affected by the instantaneous gas fraction in the galaxies. Instead, they are a chronicle of the galaxies' past star formation. Luminosity is a direct observable, but stellar mass is more closely related to chemical evolution. The mass-to-light ratio depends on the SFH.

The stellar mass-stellar metallicity relation is roughly continuous from the smallest galaxies ($M_* = 10^{3.5} M_\odot$) to the largest galaxies ($M_* = 10^{12} M_\odot$). The MZR measured from the galaxies in their sample ($M_* < 10^9 M_\odot$) is $Z_* \propto M_*^{0.30\pm0.02}$.

We have calculated the mass–metallicity relation for the UFD galaxies analyzed in this work and we have compared our results which those obtained by Kirby et al. (2013) for CvnII and Leo IV (Boötes I is not in the Kirby's sample). In order to scale the stellar mass obtained from the SFH to the whole galaxy, we have used the absolute magnitude of each galaxy from McConnachie (2012). In this way we have calculated the total stellar mass of each galaxy and compared it with the mean metallicity obtained previously.

Table 6.3 lists the values obtained to calculate the mass-metallicity relationship and those used by Kirby et al. (2013) for Canes Venatici II and Leo IV.

Figure 6.2 shows the MZR for Local Group dwarf galaxies studied in Kirby et al. (2013) (in black) and in this work (in red). The least-squares fit calculated by Kirby et al. (2013) excluding Segue 2 and the M31 satellites is

$$\langle [Fe/H] \rangle = (-1.69 \pm 0.04) + (0.30 \pm 0.02) \log(\frac{M_*}{10^6 M_\odot}) \quad (6.1)$$

The rms about the best-fit line is 0.17.

Galaxy	M_V [a]	This work		Kirby et al. (2013)	
		$\log(M_*/M_\odot)$	$\langle [Fe/H] \rangle$	$\log(M_*/M_\odot)$ [b]	$\langle [Fe/H] \rangle$
Boötes I	-6.3±0.2	4.31±0.10	-2.53±0.14	-	-
Cvn II	-4.9±0.5	4.00±0.11	-2.00±0.14	3.90±0.20	-2.12±0.05
Leo IV	-5.8±0.4	4.41±0.10	-2.52±0.15	$3.93^{\pm 0.15}_{\pm 0.11}$	-2.45±0.07

[a] McConnachie (2012).
[b] Martin et al. (2008a).

Table 6.3. Summary of values to calculate the mass-metallicity relationship.

Our results are in agreement with those obtained by Kirby et al. (2013) and, above all, we can note that the values of the mean metallicities obtained through photometry are very similar to those obtained spectroscopically for the three galaxies. Note that the mass-metallicity relation shown in Figure 6.2 spans more than six decades, involving galaxies that likely might have had different assembly histories. UFD galaxies show a single stellar, short burst with a considerable lost of gas mass enrichment of the galaxy, were able to reach the metal content expected for a galaxy of its stellar mass, following the universal mass-metallicity relationship. This points to the metallicity of a galaxy is driven by the gas mass present at its formation time that is converted into stars during the process.

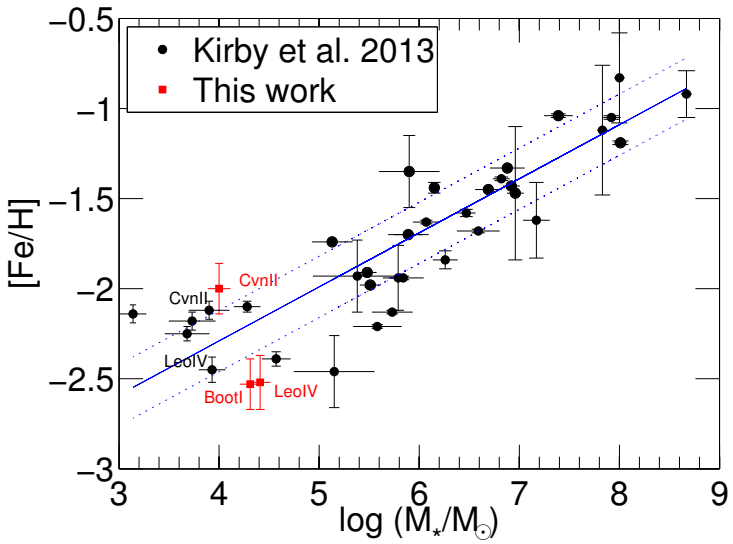

Figure 6.2. A comparison between the mass-metallicity relation for Local Group dwarf galaxies studied in Kirby et al. (2013) and in this work. The blue line is the least-squares fit to the Local Group galaxies (Equation 6.1), whereas the dotted line shows the rms about the best fit.

7

Conclusions and Future Work

7.1 Summary and Conclusions

In this thesis we have analyzed three UFDs galaxies in detail: Boötes I, Canes Venatici II and Leo IV. The data come from the Subaru Telescope in the case of Boötes I and from the Hubble Space Telescope (HST) in the case of the other two dwarfs. For all these galaxies we have obtained deep CMDs reaching the oMSTO necessary to derive a detailed SFH up to the oldest ages. We also analyzed the Segue II data obtained with the Isaac Newton Telescope (INT) but for this galaxy we have not been able to obtain a deep CMD.

The PSF photometry of Boötes has been obtained with DAOPHOT (Stetson 1987), while in the cases of CvnII and Leo IV the photometry has been obtained using DOLPHOT (Dolphin 2000). In all the cases we derived a very accurate SFH, using the IAC-method, which consists a set of codes developed by our group: IACstar/IAC-pop/MinnIAC (Aparicio & Gallart 2004; Aparicio & Hidalgo 2009; Hidalgo et al. 2011).

The main results can be summarised as follows:

- **Boötes I.** The field of view of all the Subaru images is $34' \times 27'$, which allows to cover a significant fraction of the galaxy. The images were taken with Suprime-Cam in the V and I filters. Thanks to the deep CMD obtained, we were able to derive the SFH for the entire lifetime of the galaxy. Boötes I is a very metal poor system. The mean metallicity of the solution is [Fe/H] = -2.53 ± 0.14. This value falls within the errors of the calculated value measured spectroscopically by Lai et al. (2011) that is [Fe/H] = -2.59 ± 0.43. We have also studied the distribution of stellar populations in Boötes as a function of radius, selecting two regions in the

field observed. The SFH obtained for the inner and outer regions does not differ substantially from that obtained for the entire galaxy. In both regions the bulk of the star formation occurred at $\sim$ 13.5 Gyr ago and the width of the burst is $\sim$ 1 Gyr, as before. Even the mean metallicity is unchanged. The mean metallicity is [Fe/H] = -2.52 $\pm$ 0.15 for the inner region and [Fe/H] = -2.54 $\pm$ 0.14 for the outer one. So we can say that the galaxy, within the observed field (34×27 arcmin) does not shows an stellar population gradient. The solution shows that the SFH of Boötes is dominated by an old, main episode with a peak occurring $\sim$ 13.5 Gyr ago and a duration estimated in 1.45 Gyr (FWHM). This means that the star formation ended close to $\sim$ 12 Gyr ago, so we can say that for Boötes I the quenching of the star formation is almost concurrent with the end of the epoch of reionization, fixed $\sim$ 12.7 Gyr ago. The galaxy has a luminosity of $L_V = 3.0 \pm 0.6 \times 10^4 L_\odot$ and $\sim$ 66% of its stellar mass has been formed before reionization epoch. From these two facts Boötes can really be classified as a *true fossil* of the pre-reionization era. This scenario is compatible with the hypothesis that reionization by the UV background may have contributed to the suppression of star formation in this galaxy. Another possibility is that the star formation in Boötes was stopped due to local causes, such as intense galactic winds and SNe feedback. In order to investigate this hypothesis we have calculated the mechanical luminosity of the SNe released during the main star formation episode. This quantity together with the value of the mass of gas of the galaxy can be compared with the results presented in Mac Low & Ferrara (1999) to discern the modality according to which Boötes I had lost mass in the past. From the calculated values it is clear that Boötes is placed in the region of blow-away regime in concomitance to the blow-out/mass loss regime. This result indicates that effectively SNe could have played an important role in the fate of Boötes by removing almost completely the gas component, so preventing a star formation extended over time.

- **Canes Venatici II.** Deep HST/ACS data have allowed us to derive the lifetime SFH of this ultra-faint dwarf galaxy. The images were taken using the F606W and F814W filters and the camera has a field of view of $202'' \times 202''$, which corresponds to $3.37' \times 3.37'$. The galaxy has a luminosity of $L_V = 7.9^{+3.4}_{-3.7} \times 10^3 L_\odot$ and the cumulative mass fraction shows that it formed 70% of its stellar mass $\sim$ 13.3 Gyr ago. From these two facts Cvn II can really be classified a *true fossil* of the pre-reionization era in the sense introduced in Ricotti & Gnedin (2005). From our analysis based on the model results by Mac Low & Ferrara (1999) and the calculation

of the mechanical luminosity released from SNe during the brief episode of star formation, Cvn II is placed in the blow-away regime like Boötes I. We can advance the hypothesis that in Cvn II both the ultraviolet (UV) cosmic reionization and SNe feedback may have played a fundamental role in stopping star formation in Cvn II. Based on spectroscopic results, CVn II appears to be dark matter dominated with an $M/L_V = 360^{+380}_{-180}$ (Wolf et al., 2010) and is metal-poor, with $\langle[Fe/H]\rangle$ = -2.21 ± 0.5 (Kirby et al., 2011). Our results are in agreement with those obtained spectroscopically since the mean metallicity of the solution is [Fe/H] = -2.00 ± 0.2. We have also calculated the mass–metallicity relation for Cvn II and we have compared it with that obtained by Kirby et al. (2013). Our results are in agreement with those obtained by Kirby et al. (2013) and, above all, we can note that the values of the mean metallicities obtained through photometry are very similar to those obtained spectroscopically. The solution shows that the galaxy experienced a single main event of star formation at $\sim$ 13.5 Gyr with a duration estimated in 0.78 Gyr (FWHM). This means that the star formation decreased until stopping $\sim$ 12.7 Gyr ago, coinciding with the end of the reionization epoch. It has been shown in several studies that UV photometry allows to trace the various sub-populations in the Galactic GCs much better than the traditional optical photometric bands and do so across the whole color-magnitude diagram, from the main sequence (MS) all the way to the horizontal branch (HB). We decided to apply - for the first time - this technique to eventually trace the presence of distinct sub-population in Cvn II. For this reason, we propose to complete the existing F606W and F814W data with photometry in the Sloan *u'* filter at Gran Telescopio CANARIAS (GTC13-17A; IP: Sara Murabito) and define a new photometric index $c_{u',F606W,F814W}$. We have collected deep observations in F606W and F814W of Canes Venatici II with the ACS@HST, but they are not enough to define a photometric index capable to disentangle the multiple stellar populations. For this reason, we propose to complete the existing F606W and F814W data with photometry in the Sloan *u'* filter at Gran Telescopio CANARIAS (GTC13-17A; IP: Sara Murabito) and define a new photometric index $c_{u',F606W,F814W}$. We have matched the ACS photometry with the OSIRIS photometry using DAOMATCH and DAOMASTER. We focused only in the RGB stars ($0.4 < (F606W - F814W) < 0.8$ and $19 < F814W < 24.2$), since the GTC data reach to the base of RGB. Unfortunately only $\sim 27,9\%$ of the RGB stars observed with ACS have also been observed with OSIRIS. After showing that the problem of these missing stars not observed with OSIRIS does not depend

on the region where they are located (e.g. are not near a saturated or very large cosmetic failure of the CCD), we can hypothesize that they might be much dimmer in *u'* than expected. This could be an indicator that we have a group of stars in CvnII with a different pattern in metallicity than the rest of the stars. The resulting pseudo-CMD seems to show a color spread in the RGB, but the presence of multiple sequences is not evident. So, we can not confirm or deny the existence of multiple stellar populations in CvnII or in others UFDs galaxies. What is certain is that further studies are needed in this direction.

- **Leo IV.** We used HST/ACS observations to derive the SFH of the UFD galaxy Leo IV. As for Cvn II also the images of Leo IV were taken using the F606W and F814W filters. The detailed SFH reveals that Leo IV is dominated by an old, main episode with maximum occurring $\sim$ 13.5 Gyr ago and a duration estimated in 1.72 Gyr (FWHM). This means that the star formation ended close to $\sim$ 11.8 Gyr ago, after the end of the epoch of the reionization fixed at $\sim$ 12.7 Gyr (Becker et al. 2001). The galaxy has a luminosity of $L_V = 8.7^{+4.4}_{-4.7} \times 10^3 L_\odot$ and the cumulative mass fraction shows that it formed 70% of its stellar mass $\sim$ 11.78 Gyr ago. Although Leo IV continued to form a few stars even after the end of the epoch of reionization, it can anyway be classified a *true fossil* of the pre-reionization era. As for Boötes I and Cvn II, we have calculated the mechanical luminosity of the SNe released during the main star formation episode and the value of the mass of gas of the galaxy. From our analysis based on the model results by Mac Low & Ferrara (1999) it is clear that Leo IV places in the region of blow-out/mass loss regime, but fairly close to the blow-away regime. In Boötes I and Cvn II the feedback of SNe would have created outflows that completely blow away the gas, whereas in Leo IV the mass loss by galactic winds is important, but not complete. In other words, Leo IV seems to be massive enough to conserve at least a fraction of its gas against SN feedback. Note that Leo IV has the more extended SFH of the galaxies of this sample, reaching $\sim$ 1.7 Gyr, and a lower total number of SNe. This slower evolution of Leo IV compared with the other galaxies of the sample would have allowed to Leo IV keep a gas reservoir to keep forming stars. Leo IV is a very metal poor system. The mean metallicity of the solution is [Fe/H] = -2.52 $\pm$ 0.15. This value falls within the errors of the calculated value measured spectroscopically by (Kirby et al., 2011) that is [Fe/H] = -2.54 $\pm$ 0.07. We have also calculated the mass–metallicity relation for Leo IV and we have compared it with that obtained by Kirby et al. (2013).

This thesis confirms the fact that UFDs are galaxies mainly dominated by a unique old metal-poor stellar population, which seems to be well constrained in time.

The quenching of the star formation is concurrent in all the study cases with the end of the EoR, which makes these galaxies "true fossils" of the pre-reionization era. SNe feedback may have played a role in Böotes I and CnV II by heating and diluting the remaining gas after the peak of the star formation. In the case of Leo IV, it seems that the galaxy could have retained some gas after the end of the EoR, extending its stellar formation for a longer time. In this case, Leo IV is a good candidate to search for a multipopulation component.

Although UFD galaxies show a considerable lost of gas mass during its formation, they were able to reach the metal content expected for a galaxy of its stellar mass, following the well know mass-metallicity relation. This points to a metallicity enrichment driven by the gas mass present at its formation time.

7.2 Future Work

UFD galaxies are important targets for understanding the physics of dark matter and galaxy formation on the smallest scales. The details of their nature provide crucial empirical input for verifying formation scenarios of the Milky Way (MW). Along with this thesis, we have comprehensively studied the UFDs Boötes I, Canes Venatici II and Leo IV but many new extremely faint, low mass galaxies in the Local Group have been discovered in the last few years. The methodologies applied in this thesis are easily applicable to other systems, providing the most comprehensive information about them.

We have seen how the HST data provided deep CMDs reaching the oMSTO necessary to derive a detailed SFH up to the oldest ages for CvnII and Leo IV. It would be interesting to apply the IAC method to obtain SFH also to other UFDs observed with HST. The HST archive provides images in the F606W and F814W filters for the following UFDs: Ursa Major I, Canes Venatici I, Coma Berenices, Leo V and Leo T. This would allow us to increase our UFDs sample to try to understand the effect of several physical processes in the formation and evolution of dwarf galaxies, such as the reionization, feedback by supernovas or tidal interactions.

It would also be interesting to see if a combination of UV filters (we have only used *u'* in the case of CvnII) can be a powerful tool for tracking the presence of distinct subpopulations using a photometric data set as in the case of GCs (Bellini et al. 2010, 2013; Milone et al. 2010, 2012b, 2013; Piotto et al. 2012, 2013).

We have attempted, for the first time in a UFD galaxy, investigate the presence of multipopulations using a combination of one UV filter, but the results are not clear. Extending these observations to another UV filter would be necessary to ascertain if UFD host subpopulations as in the GCs. In this sense, the GRANTECAN will be a magnificent facility to understand the nearest UFD and to reach fully study of these systems.

A

Telescopes and Instruments

A.1 Introduction

SINCE its invention 400 years ago, the astronomical telescope has evolved from a small, manually pointed device for visual observations to a large, sophisticated, computer-controlled instrument with full digital output. Throughout this development, two properties have been particularly important: the light-collecting power, or diameter of the telescope's mirror (allowing for the detection of fainter and more distant objects), and the image sharpness, or angular resolution (allowing smaller and fainter objects to be seen).

With advancing technology, astronomers discovered many faint stars and the calculation of stellar distances. In the 19th century, using a new instrument called a spectroscope, astronomers gathered information about the chemical composition and motions of celestial objects. Twentieth century astronomers developed bigger and bigger telescopes and, later, specialized instruments that could peer into the distant reaches of space and time.

The 20th century also saw the development of telescopes that worked in a wide range of wavelengths from radio to gamma-rays. Since the atmosphere is opaque for most of the electromagnetic spectrum, only a few bands can be observed from the Earth's surface. These bands are visible, near-infrared and a portion of the radio-wave part of the spectrum. For this reason there are no X-ray or far-infrared ground-based telescopes as these have to be observed from orbit. The first purpose built radio telescope went into operation in 1937. Since then, a tremendous variety of complex astronomical instruments have been developed.

Ground-based telescopes, like Subaru, are limited by the presence of the

Earth's atmosphere, which absorbs and scatters incident electromagnetic radiation. *Astronomical seeing* refers to the blurring and twinkling of astronomical objects such as stars caused by turbulent mixing in the Earth's atmosphere that causes variations of the optical refractive index. The astronomical seeing conditions on a given night at a given location describe how much the Earth's atmosphere perturbs the images of stars as seen through a telescope.

Seeing is one of the biggest problems for Earth-based astronomy: while large telescopes have theoretically milli-arcsecond resolution, the real image will never be better than the average seeing disc during the observation. This can easily mean a factor of 100 between the potential and practical resolution. Starting in the 1990s, new adaptive optics have been introduced that can help correct for these effects, dramatically improving the resolution of ground based telescopes. The technique of active optics, which is now in use in most modern medium-sized and large telescopes, preserves optimal image quality by pairing a flexible mirror with actuators that actively adjust the mirror's shape during observations.

But while these technologies are revolutionizing the ability of ground-based telescopes to image beyond the Earth's atmosphere, additional advances in the design and construction of space-based telescopes are having an equally significant impact on deep-space research. In the decades that followed the giant-balloon strategy of the 1960s, it became clear that what was really needed was free-flying space telescopes—that is, telescopes that can orbit on their own. So, NASA's Great Observatories program was born. The Great Observatories program led to the creation of four big, powerful space-based astronomical telescopes, including the Spitzer Space Telescope and the Hubble Space Telescope that launched over 25 years ago, in 1990.

Space-based telescopes like Hubble get a much clearer view of the universe than most of their ground-based counterparts. They are also able to detect frequencies and wavelengths across the entire electromagnetic spectrum. Ground-based telescopes can't do the same, because the Earth's atmosphere absorbs a lot of the infrared and ultraviolet light that passes through it.

Nevertheless, space-based telescopes are expensive to build and difficult to maintain. But as technology advances, both telescopes on the ground and in space are continuing to improve. The next telescope that will push the boundaries of technology for astronomical observation is NASA's James Webb Space Telescope, scheduled to launch in 2018. It will be used by thousands of astronomers worldwide, studying every phase in the history of the Universe.

In this thesis I used data coming from both ground-based telescopes (Subaru Telescope and Gran Telescopio Canarias) and space telescopes (Hubble Space Telescope). The characteristics of the Suprime-Cam, WFC and OSIRIS are

listed in Tab.A.1.

	Suprime-Cam	WFC	OSIRIS
Telescope	Subaru	HST	GTC
Field of view	∼34' × 27'	202" × 202"	7.8' × 7.8'(unvignetted)
Pixel scale	0.20"/pixel	∼0.05"/pixel	0.254"/pixel (binning 2×2)
Pixel size	15 μm	15 × 15 μm	15 μm
Number of CCDs	5 × 2	2	2
Image format	2048×4096 pixels	2 × 2048×4096 pixels	2 × 2048×4096 pixels
Spectral response	3500 Å to 10500 Å	∼3500 Å to 11000 Å	3650 Å to 10500 Å
Detector efficiency	95% at 6500 Å	83% at 6000 Å	90% 6000 Å
Gain	2.5-3.7 e^-/ADU	1.953 - 2.014 e^-/ADU	0.95 e^-/ADU
Read noise	10 e^-	4.2 e^-	∼4.5 e^-

Table A.1. Instrumental characteristics of the Suprime-Cam, WFC and OSIRIS.

In Fig.A.1 is show the difference between the spectral sensitivity of WFC wide filters (top panel) and standard Johnson filters (botton pannel) as function of the wavelength. In particular, the Subaru data analyzed here are in the latter photometric system.

A.2 The Isaac Newton Telescope

The Isaac Newton Telescope started operations in Herstmonceux, United Kingdom, in 1967, but after a number of years it became clear that better astronomical weather conditions would benefit the astronomical use of the telescope. Such conditions are found on the Roque de Los Muchachos Observatory and therefore it was decided to move the telescope to La Palma, where it resumed operations in 1984.

The Isaac Newton Telescope has a 2.5-metre primary mirror. It uses a polardisc and fork type of equatorial mount supported by five axial and three radial hydrostatic oil bearing pads. Instruments can be mounted either at the Prime focus or the Cassegrain focus, and they offer the possibility of carrying out both wide-field imaging and intermediate to low dispersion spectroscopy.

The instruments offered at the INT are:

- Wide Field Camera (WFC): Imaging over a 33-arcmin field with a wide variety of broad- and narrow-band filters.
- Intermediate Dispersion Spectrograph (IDS): Medium-low resolution long-slit spectroscopy. IDS is offered with a set of 16 gratings providing disper-

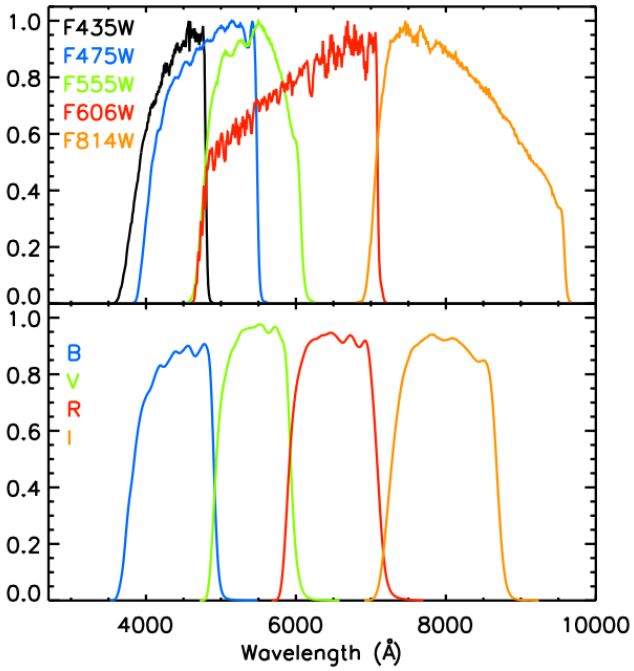

Figure A.1. Comparison between the transmission curves between WFC filters (*top panel*) and standard Johnson-Cousins filters (*bottom panel*), as those of the Subaru.

sions in the range of 4-0.24 Å pixel-1. It can be used with Red+2 detector (default) or EEV10 detector (if requested and justified in the proposal).

The number of scientific highlights obtained using the Isaac Newton Telescope over the years is very high. The telescope has made many important contributions to the research of quasars, supernovas, black holes, dwarf galaxys, the Milky Way, planetary nebulae, and star evolution. The first ever observational evidence of the existence of a black hole is one of the most outstanding results obtained using the Isaac Newton Telescope.

A.2.1 The Wide Field Camera

The Wide Field Camera is an advanced instrument which offers unique opportunities to execute high resolution, very deep, wide field optical imaging surveys. It consists of a mosaic of 4 thinned EEV 2kx4k CCDs that cover a field of view of 34 × 34 arcmin. The CCDs have a pixel size of 13.5 microns corresponding to 0.33 arcsec/pixel. The cycle time for the whole mosaic is around 42 seconds. A maximum of 6 filters could be installed in the wheel. Both broadband and Stromgren filter sets are available, as well as a range of narrowband filters. Table A.2 summarizes some physical characteristics of the Wide Field Camera, whereas Figure A.2 show the details of gaps between image areas of mosaic elements.

Field of view	34 × 34 arcmin
Pixel scale	0.333 arcsec/pixel
Pixel size	13.5 μm × 13.5 μm
Number of CCDs	4
Image format	2048×4100 pixels

Table A.2. Physical characteristics of the Wide Field Camera.

A.3 The Subaru Telescope

The Subaru Telescope is an 8.2-m optical-infrared telescope located on the summit (4200 m) of Mauna Kea, a dormant volcano on the Big Island of Hawaii. Construction of the telescope began in April 1991, and later that year, a public contest gave the telescope its official name, "Subaru Telescope". Construction was completed in 1998, and the first scientific images were taken in January 1999. It is operated by the National Astronomical Observatory of Japan (NOAJ).

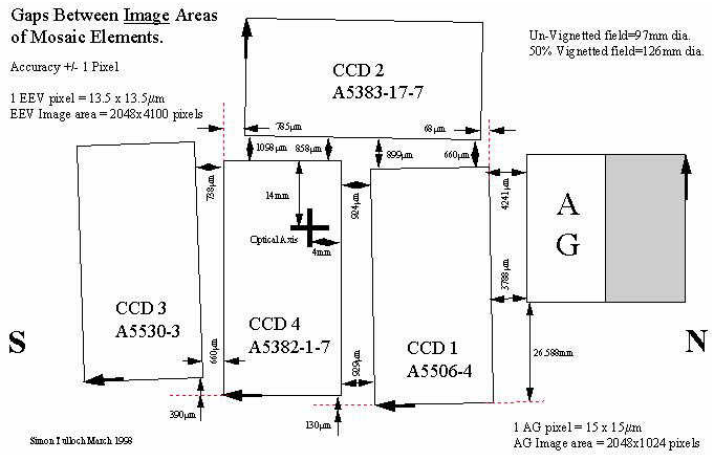

Figure A.2. Details of gaps between image areas of mosaic elements of WFC@INT.

Subaru is a Ritchey-Chretien reflecting telescope. Instruments can be mounted at a Cassegrain focus below the primary mirror, in enclosures on either of two Nasmyth focal points on the sides of the telescope mount, to which light can be directed with a tertiary mirror, or, in an arrangement rare on large telescopes, at the prime focus, in lieu of a secondary mirror, to provide a wide field of view suited to deep wide-field surveys.

The telescope represents a new generation in telescope design not only because of the size of its primary mirror with an effective aperture of 8.2 meters, but also because of the various revolutionary technologies used to achieve outstanding performance. An active support system that maintains an unprecedentedly high mirror surface accuracy, a new enclosure design to suppress local atmospheric turbulence, an extremely accurate tracking mechanism using magnetic driving systems, seven observational instruments installed at the four foci, and an auto-exchanger system to use the observational instruments effectively are just some of the unique features associated with this telescope.

Subaru Telescope has a suite of nine facility instruments providing imaging and spectroscopic capabilities over the full range of wavelengths from optical to mid-infrared.

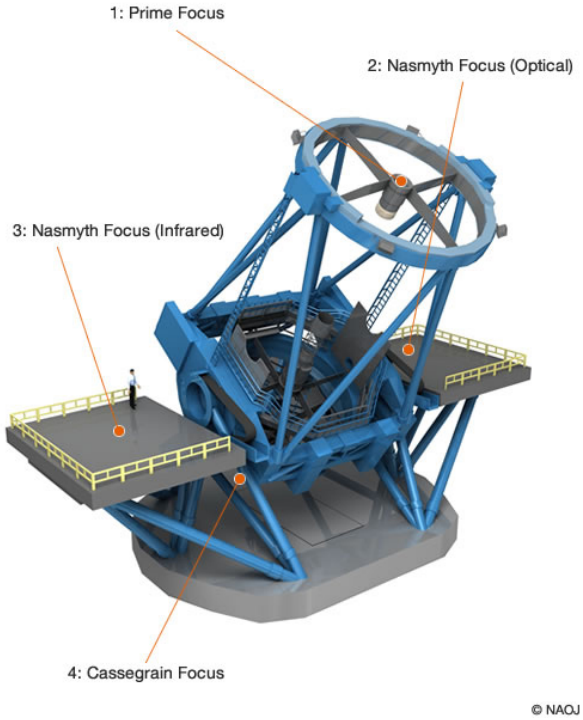

Figure A.3. The four foci of the Subaru Telescope.

- HSC: Hyper Suprime-Cam which provides optical imaging over a very large field of view (1.5 degree diameter) with a mosaic of CCDs.
- FMOS: Fiber Multi-Object Spectrograph is a powerful, fiber-fed, wide-field spectroscopy system that enables near-infrared spectroscopy of over 100 objects at a time.
- MOIRCS: Multi-Object Infrared Camera and Spectrograph is a near-infrared camera and spectrograph that combines a wide field of view with the capacity to capture the spectra of about 40 objects simultaneously. Provides imaging and low-resolution spectroscopy from 0.9-2.5 microns over a 4 arcmin × 7 arcmin field of view.
- IRCS: Infrared Camera and Spectrograph is a versatile near-infrared camera and spectrograph that provides high-angular resolution imaging combined with AO188, low-resolution grism and high-resolution echelle spectroscopies over 0.9-5.6 microns.
- COMICS: Cooled Mid Infrared Camera and Spectrometer provides imaging and spectroscopy from 7.5-25 microns.
- FOCAS: Faint Object Camera And Spectrograph provides optical imaging and longslit and multi-slit spectroscopy over a 6 arcmin field of view.
- Suprime-Cam: Subaru Prime Focus Camera has the extaordinary capability not only of efficiently imaging a wide field of view but also of capturing images of very faint objects with high levels of detail and contrast—in a single exposure.
- HDS: High Dispersion Spectrograph provides extremely high-resolution optical spectroscopy.
- AO: Subaru 188-Element Adaptive Optics delivers diffraction-limited images in the near-infrared.

A.3.1 Suprime-Cam

The Subaru Prime Focus Camera (Suprime-Cam, Miyazaki et al., 2002) is a mosaic of ten 2048 × 4096 CCDs, located at the prime focus of Subaru Telescope, which covers a 34' × 27' field of view with a pixel scale of 0.20". The parameters of the Suprime-Cam are summarized in Table A.1.

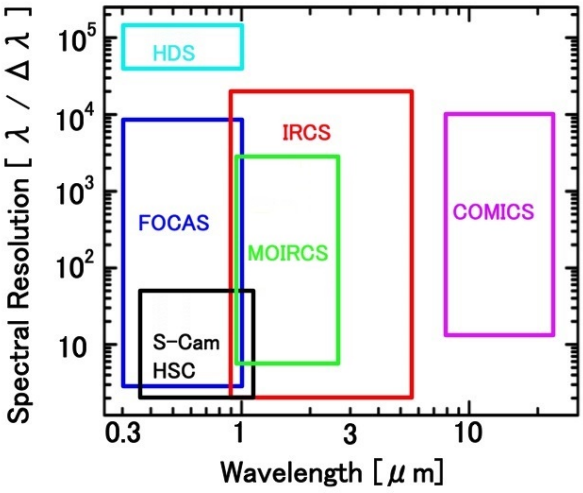

Figure A.4. The figure shows the wavelength regime detected by the instruments above and how finely each can divide that light into component of wave-lengths or colors (spectral resolution). Instruments with different fields of view or special features optimized for particular scientific targets sometimes have overlapping wavelength and resolution coverage.

The focal plane consists of ten high-resistivity 2k×4k CCDs developed by MIT Lincoln Laboratory, which are cooled by a large Stirling-cycle cooler. The CCD readout electronics was designed to be scalable, which allows the multiple read-out of tens of CCDs. It takes 50 seconds to readout entire arrays. Small gaps exist between the CCDs due to the coplanarity requirement at the prime focus of Subaru Telescope. The following diagram indicates the approximate sizes of the interchip gaps (Fig. A.5).

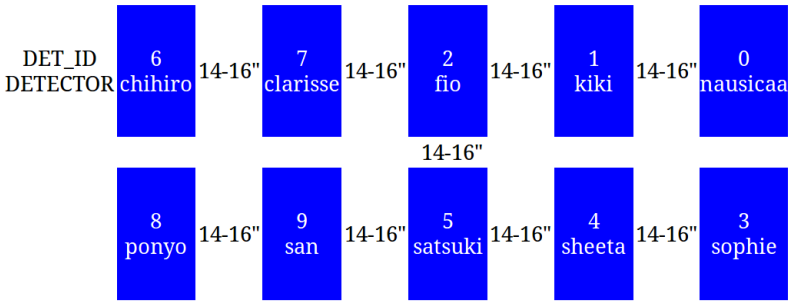

Figure A.5. Schematic plot of the 10 CCDs of the Suprime-Cam. The total field of view covered by the 10 CCDs is 34' × 27'

Note that the 10 CCDs do not provide uninterrupted sky coverage. The gaps between adjacent CCDs correspond to approximately 14-16" on the sky. Three exposures are required to cover a contiguous region of sky. Data from each individual chip are stored separately, and thus one image from Suprime-Cam consists of ten FITS files. Each chip has a one-digit detector ID, recorded in the FITS keyword DET_ID. Each chip also has a "call name" consisting of a series of characters and numbers which are recorded in the FITS keyword DETECTOR. DET_ID corresponds to the final digit of the FRAMEID which is a sequencial number (SUPA***) assigned to each FITS file in the data archive system STARS/MASTARS and SMOKA (e.g., DET_ID=8 for FRAMEID=SUPA00157008).

A.4 The Hubble Space Telescope

The Hubble Space Telescope (HST) is a cooperative program of the European Space Agency (ESA) and the National Aeronautics and Space Administration

(NASA) to operate a space-based observatory for the benefit of the international astronomical community. Hubble was funded in the 1970s, with a proposed launch in 1983, but the project was beset by technical delays, budget problems, and the Challenger disaster (1986). When finally launched in 1990, Hubble's main mirror was found to have been ground incorrectly, compromising the telescope's capabilities. The optics were corrected to their intended quality by a servicing mission in 1993. Since its preliminary inception, HST was designed to be a different type of mission for NASA. To accomplish this goal and protect the spacecraft against instrument and equipment failures, NASA planned on regular servicing missions. Responsibility for conducting and coordinating the science operations of the Hubble Space Telescope rests with the Space Telescope Science Institute (STScI) on the Johns Hopkins University Homewood Campus in Baltimore, Maryland. STScI is operated for NASA by the Association of Universities for Research in Astronomy, (AURA).

HST is a 2.4-meter reflecting telescope, which was deployed in low-Earth orbit (600 kilometers) by the crew of the space shuttle Discovery (STS-31) on 25 April 1990. Light hitting the telescope's main, or primary mirror is reflected to a smaller, secondary mirror suspended above the primary. The secondary, in turn, reflects the light back through a hole in the primary where it enters Hubble's instruments (cameras and spectrographs) for final focus before it hits their detectors. Hubble's primary mirror is not only exquisitely polished, but at 94.5 inches (2.4 m) in diameter, collects an immense amount of light. Hubble can detect objects that are 10 billion times fainter than the unaided eye can see. High above the blurring effects of Earth's atmosphere, Hubble also gets a much clearer view of the cosmos than do telescopes located on the ground. The space telescope can distinguish astronomical objects with an angular diameter of a mere 0.05 arc seconds — the equivalent to discerning the width of a dime from a distance of 86 miles. This resolution is about 10 times better than the best typically attained by even larger, ground based telescopes. High resolution enables Hubble to locate such objects as dust discs around stars or the glowing nuclei of extremely distant galaxies.

Because of HST is location above the Earth's atmosphere, these science instruments can produce high-resolution images of astronomical objects. Ground-based telescopes are limited in their resolution by the Earth's atmosphere, which causes a variable distortion in the images. Hubble can observe ultraviolet radiation, which is blocked by the atmosphere and therefore unavailable to ground-based telescopes. In the infrared portion of the spectrum, the Earth's atmosphere adds a great deal of background, which is absent in Hubble observations. This gives astronomers using Hubble a fuller view into the energetic processes

that create the radiation seen and measured.

Finally, Hubble's observations are predictably consistent. The telescope's seeing conditions do not change from day to day or even orbit to orbit. Astronomers can revisit targets with the expectation that they will be imaged at the same high quality each time. This optical stability is critical for detecting tiny motions or other small variations in celestial objects. Such is not the case for ground-based observatories, where observing conditions vary with weather and directly affect the quality of the images acquired.

HST is current complement of science instruments includes three cameras, two spectrographs, and fine guidance sensors (primarily used for accurate pointing, but also for astrometric observations).

- STIS: The Space Telescope Imaging Spectrograph is a second-generation imager/spectrograph. It is used to obtain high resolution spectra of resolved objects and can study these objects across a spectral range from the UV (115 nanometers) through the visible red and the near-IR (1000 nanometers). STIS has the special ability to simultaneously obtain spectra from many different points along a target.

- NICMOS: The Near Infrared Camera and Multi-Object Spectrometer is an HST instrument providing the capability for infrared imaging and spectroscopic observations of astronomical targets. NICMOS detects light with wavelengths between 0.8 and 2.5 microns - longer than the human-eye limit. NICMOS has three adjacent but not contiguous cameras, designed to operate independently, each with a dedicated array at a different magnification scale.

- ACS: The Advanced Camera for Surveys is a camera designed to provide HST with a deep, wide-field survey capability from the visible to near-IR, imaging from the near-UV to the near-IR with the point-spread function critically sampled at 6300 Å, and solar blind far-UV imaging.

- FGS: The Fine Guidance Sensors, in addition to being an integral part of the HST Pointing Control System (PCS), provide HST observers with the capability of precision astrometry and milliarcsecond resolution over a wide range of magnitudes ($3 < V < 16.8$). Its two observing modes - Position Mode and Transfer Mode - have been used to determine the parallax and proper motion of astrometric targets to a precision of 0.2 mas, and to detect duplicity or structure around targets as close as 8 mas (visual orbits can be determined for binaries as close as 12 mas). Hubble has three FGSs onboard the observatory.

- COS: The Cosmic Origins Spectrograph is a fourth-generation instrument that was installed on the Hubble Space Telescope (HST) during the 2009 servicing mission. COS is designed to perform high sensitivity, moderate- and low-resolution spectroscopy of astronomical objects in the 115-320 nm wavelength range. It significantly enhances the spectroscopic capabilities of HST at ultraviolet wavelengths, and provides observers with unparalleled opportunities for observing faint sources of ultraviolet light. The primary science objectives of the COS are the study of the origins of large scale structure in the Universe, the formation and evolution of galaxies, the origin of stellar and planetary systems, and the cold interstellar medium.

- WFC3: The Wide Field Camera 3 is also a fourth generation instrument that was installed during the 2009 servicing mission. Equipped with state-of-the-art detectors and optics, WFC3 provides wide-field imaging with continuous spectral coverage from the ultraviolet into the infrared, dramatically increasing both the survey power and the panchromatic science capabilities of HST. The WFC3 has two camera channels: the UVIS channel that operates in the ultraviolet and visible bands (from about 200 to 1000 nm), and the IR channel that operates in the infrared (from 900 to 1700 nm). The performance of the two channels was designed to complement the performance of the ACS.

The relative locations of the science instruments in the focal plane and their fields of view are shown schematically in Fig. A.6.

A.4.1 The Advanced Camera for Surveys

The Advanced Camera for Surveys (ACS) is a third-generation instrument that was installed in the Hubble Space Telescope during Servicing Mission 3B, on March 7, 2002. Its primary purpose was to increase HST imaging discovery efficiency by about a factor of 10, with a combination of detector area and quantum efficiency that surpasses previous instruments. ACS has three independent cameras that have provided wide-field, high resolution, and ultraviolet imaging capabilities respectively, using a broad assortment of filters designed to address a large range of scientific goals. In addition, coronagraphic, polarimetric, and grism capabilities have made the ACS a versatile and powerful instrument.

The ACS includes three channels (Avila et al., 2017):

- a Wide Field Channel (WFC), with a field of view of 202×202 square arcsec covering the range from 3500 Å to 11000 Å and a plate-scale of 0.05 arcsec/pixel;

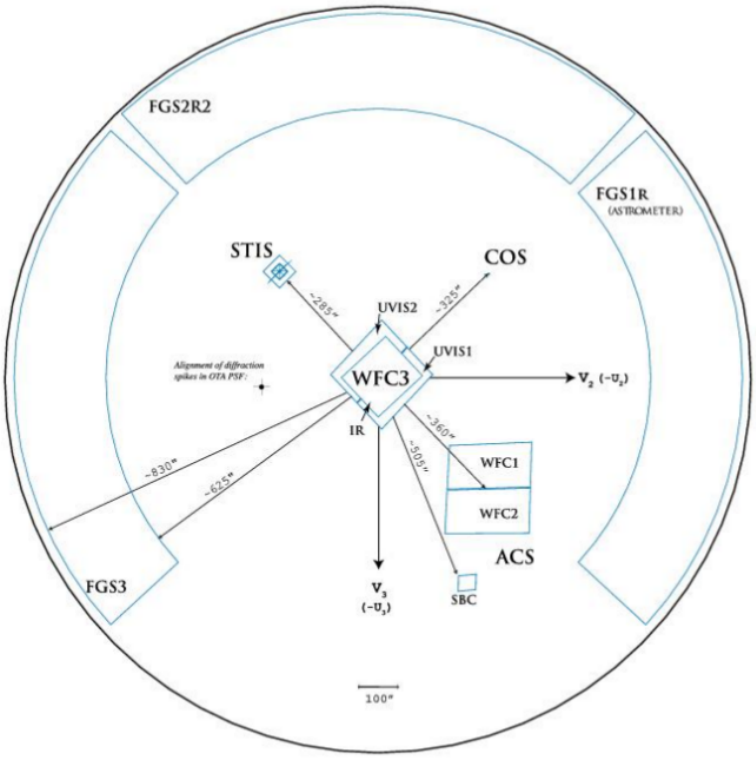

Figure A.6. Hubble Space Telescope field of view with the onboard instruments indicated.

- a High Resolution Channel (HRC), with a field of view of 29×26 square arcsec covering the range from 1700 Å to 11000 Å and a plate-scale of 0.027 arcsec/pixel;
- a Solar Blind Channel (SBC), with a field of view of 34.6×30.5 arcsec field of view, spanning the range from 1150 Å to 1700 Å and a plate-scale of 0.032 arcsec/pixel.

I have used data coming from the WFC@ACS, whose optical design is schematically show in Fig. A.7.

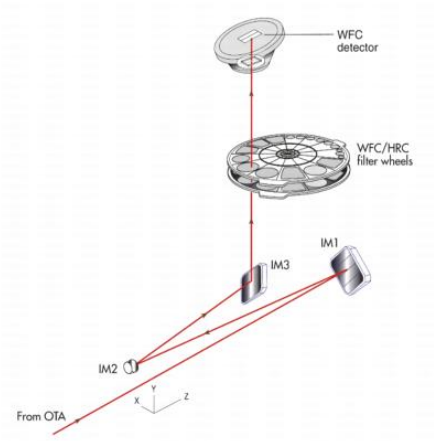

Figure A.7. ACS Wide Field Channel optical design.

The ACS design incorporates two main optical channels: one for the WFC, and one which is shared by the HRC and SBC. Each channel has independent corrective optics to compensate for spherical aberration in the HST primary mirror. The WFC has silver-coated optics to optimize instrument throughput in the visible and near-IR. The silver coatings cut off wavelengths shortward of 3500 Å. The WFC has two filter wheels which it shared with the HRC, offering the possibility of internal WFC/HRC parallel observing for some filter combinations. The WFC/HRC filter wheels contain the major filter sets. Each wheel also contains one clear WFC aperture and one clear HRC aperture.
The CCD filter wheels contain filters of two different sizes. Some filters (F435W,

F475W, F502N, F550M, F555W, F606W, F625W, F658N, F660N, F775W, F814W, F850LP, and, G800L) are full-sized filters that can be used with both WFC and HRC. Others (F220W, F250W, F330W, F344N, F892N, POL0UV, POL60UV, POL120UV, POL0V, POL60V, POL120V, and PR200L) are smaller, giving a full unvignetted field of view when used with the HRC, but a vignetted field of view of only 72×72 arcseconds when used with the WFC. Use of the small UV filters with WFC is not supported due to the unpredictable behavior of the silver coating shortward of 4000 Å.

A summary of the WFC CCD performance is given in Table A.1.

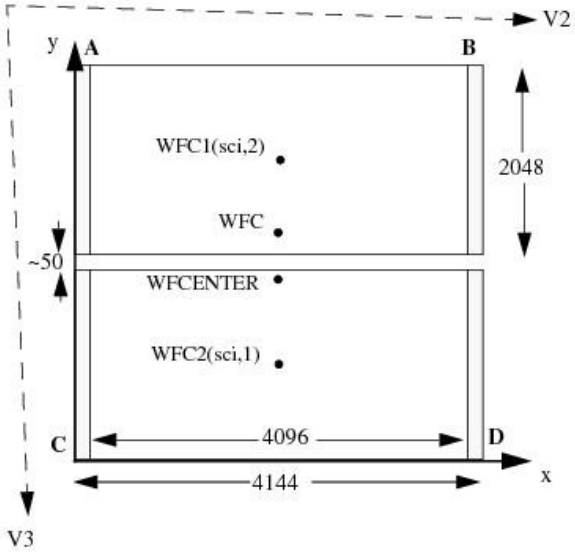

Figure A.8. The WFC apertures plotted with respect to the V2,V3 reference frame, and oriented such that the x-axis runs approximately towards the right and the y-axis runs approximately straight up. In pipeline data products, WFC2 is displayed below WFC1 (along the y-axis) and is therefore designated as extension 1.

The active image area of each WFC detector is 4096 by 2048 pixels. The mean scale is 0.049 arc seconds/pixel, and the combined detectors cover an

approximately square area of 202 arc seconds on a side. In establishing reference pixel positions we have to consider the overscan pixel areas which extend 24 pixels beyond the edges in the long direction. So each CCD must be regarded as a 4144 by 2048 pixel area. The gap between the two CCDs is equivalent to 50 pixels. In Figure A.8 the letters A, B, C, and D show the corner locations of the four readout amplifiers. The apertures named WFC1 and WFC2 represent the two CCDs, with their reference points near the geometric center of each chip. The positions have been moved about 50 pixels from the center line to avoid a discontinuity at the amplifier readout boundary. The aperture WFC encompasses both detectors, and has its reference point near the overall center but about 10 arcseconds away from the inter-CCD gap. This reference point is (2124,200) on the WFC1 CCD. WFCENTER is similar to WFC, but is placed at the center of the combined WFC full field. The center is defined as the average of the four corners in the distortion corrected space. Because of the scale variation this does not appear at the center in pixel space, but rather is on WFC2 about 20 pixels from the edge. Selection of WFCENTER can be of use in obtaining observations with maximum overlap at unique orientations and for mosaics. On sky, the WFC aperture is roughly square, and it is natural to design observations in steps of 90° to consistently cover the same area. There will be some region at the edges not covered at all four orientations. However, a square area of side 194.8 arcseconds centered on WFCENTER, and with edges parallel to the V2 and V3 axes, is overlapped at all four positions. In designing a mosaic which combines observations at 90° steps, a translation of about 190 arcseconds between pointings would provide continuous coverage.

WFC filter (F435W, F475W, F555W, F606W, and F814W) spectral sensitivity is shown in the top panel of Fig. A.1, where the wavelength is in Å. In the bottom panel of the same figure the standard Johnson filters as function of the wavelength are plotted in order to show the difference between WFC wide filters and the standard ones. In particular, the Subaru data analyzed here are in the latter photometric system.

A.5 Gran Telescopio Canarias

The Gran Telescopio CANARIAS (GTC), is currently the largest and one of the most advanced optical and infra-red telescopes in the world. It is located in one of the top astronomical sites in the Northern Hemisphere: the Observatorio del Roque de los Muchachos (ORM, La Palma, Canary Islands). With the leadership of the Instituto de Astrofísica de Canarias (IAC), its First Light Ceremony was celebrated in the early morning of 14th July, 2007. Scientific production of

the telescope started in March of 2009, once the telescope optics and its control system was sufficiently well developed, and the first science instrument, OSIRIS, had been installed.

In 1994, the public limited company GRANTECAN, S.A. was founded with the aim to design and construct the Gran Telescopio CANARIAS, or GTC. The project is actively supported by the Spanish Government and the Local Government from the Canary Islands through the European Funds for Regional Development (FEDER) provided by the European Union. GTC also has an international recognition through the agreements signed with the Mexican Government to participate in the project through the Instituto de Astronomía de la Instituto de Astronomía de la Universidad Nacional Autónoma de México y del Instituto Nacional de Astrofísica, Óptica y Electrónica de Puebla. In addition, participation from the United States is through collaboration with the University of Florida. The telescope time is shared by Spanish scientists (90%), Mexico (5%) and the U.S. (5%), the same percentage who contributed to the initial project.

The Gran Telescopio Canarias (GTC) has an altitude-azimuth mount and an optical layout of the Ritchey-Chrétien type with Nasmyth, Cassegrain and Folded Cassegrain foci. Its useful wavelength range extends from 365nm to 25μm. Its primary mirror consists of 36 individual hexagonal segments of Zerodur coated with aluminium that together act as a single mirror. Each segment measures 1.9m from vertex to vertex and has a side length of 0.9m and a weight of 470 kg. They cover a total surface of 75.7 square metres (73 m^2 effective area) and have gaps of 3mm between them. The light collecting mirror surface area of GTC is equivalent to that of a telescope with a 10.4m diameter single monolithic mirror. Due to the curvature of M1 the segments are not all identical but come in 6 types, corresponding to their six different distances to the center. Each segment, regardless of type, is supported by 3 position actuators which enable movements in piston, tip and tilt, as well as 6 moment actuators which allow a slight deformation of the segment. The relative positions of segments with respect to each other are measured with edge sensors. These are capacitive sensors that are mounted in pairs on the sides of adjacent segments.

In order for M1 to act as one mirror instead of 36 individual telescopes it is necessary to align the segments in a specific way so as to form a near-perfect common focus. This process comprises two steps: stacking and phasing. For stacking, initially the image of a star is taken with the M1 segments in some random configuration. The positions of the 36 individual images are compared with their nominal position, and from the difference an array with piston, tip and tilt for each segment is calculated. In a second step, a fine tuning of the

stacking including the alignment with the secondary mirror (M2) is performed with images from a wave front sensor. The alignment array is loaded at the beginning of each night to align M1 and M2. The stacking is quite stable so that the rough stacking procedure is necessary only after a major intervention such as a change of segments for cleaning and re-coating. The fine stacking is needed to maintain the best possible image quality, and is currently performed typically once or twice a week.

Once M1 is stacked, the next step is phasing which ensures that light from different segments is coherent. The process of phasing is carried out in two steps. First the image of the pupil is aligned with the lenslet array of the wavefront sensor to ensure that the two apertures of a double slit coincide with adjacent segments. The second step is the actual phasing, in which the segments are moved in piston. The interference pattern produced by adjacent segments allows to determine the piston positions where the light from both segments is coherent. In this way, the piston positions are calculated for all the segments to be in phase. Tip and tilt are not relevant for the phasing as these are determined during the stacking. Also the phasing stability is quite good, which means that normally twice per month the process has to be carried out.

Apart from the 3 position actuators controlling movements in piston, tip and tilt, each segment has 6 moment actuators which allow a certain deformation of the segment. This function allows to compensate for deformations due to gravity and for imperfections of the polishing. It is relevant for the future implementation of adaptive optics, but not for stacking and phasing. The maximum deformation of a segment is such that the difference between centre and edge reaches about 1 μm.

The GTC has also a secondary mirror and a tertiary mirror that together with the primary mirror produce the telescope focal plane in the focal station of choice. The secondary mirror is a lightweight convex hyperbolid of beryllium with aluminium coating. M2 defines the telescope pupil, and in order to minimize effects of thermal radiation its outer perimeter and central hole reflect the shape of M1. Its area is equivalent to a circular mirror with a diameter of 1.06 m. For alignment with M1, M2 has 5 degrees of freedom: movement in x and y (decentring) and focus (along the optical axis) as well as tip- tilt rotations. For chopping, the maximum frequency is 14 movements per second.
The tertiary mirror is a at elliptical shaped mirror with dimensions of 1521 cm $\times$ 1073 cm. M3 is mounted in a tower of 7m in altitude and 1.8m in diameter and can be inserted in the beam to direct the light to either of the Nasmyth foci or parked so that the beam reaches the Cassegrain focus.

The telescope mount, a large mechanical, steel structure that holds the mir-

rors, allows rotational movements of the telescope along a horizontal and vertical axis. This movement has to be extremely precise in order to keep the stars projected stably onto the detector. The telescope is designed so that it is able to observe the optical and infrared light ranges.

The dome has a height of 24m and an outside diameter of 35m. The shutter has a width of 13 m; the lower shutter with a weight of 16 tons is powered by 2 motors while the upper shutter with a weight of 41 tons is powered by 4 motors. For reasons of safety of the equipment it is currently not possible to open the dome to elevations higher than 72 degrees, the lower limit is 25 degrees.

The scientific instruments that are placed in the focal station then analyse and detect the light, and store the final data.

A.5.1 OSIRIS

OSIRIS is an imager and spectrograph for the optical wavelength range, located in the Nasmyth-B focus of GTC. The OSIRIS acronym stands for *Optical System for Imaging and low-intermediate Resolution Integrated Spectroscopy*, which encapsulated in a few words the versatile nature of this instrument. Apart from the standard broad-band imaging and long-slit spectroscopy, it provides additional capability such as the narrow-band tunable filters imaging, charge-shuffling and multi-object spectroscopy.

A key scientific driver in the design of OSIRIS has been the study of star formation indicators in nearby galaxies and more distant objects, back to the furthest observable galaxies with GTC. In particular, star formation in galaxies as a function of redshift is a classical topic and one main objectives of several current projects of instruments for large telescopes both, ground based and aboard satellites.

OSIRIS is directly attached to the GTC field rotator and guide unit in the GTC Nasmyth-B focal station (Figure A.9). The instrument optics are designed around the classical concept of collimator plus camera. For reasons of keeping the instrument compact, the optical train is folded and the field is off-axis. Its compact design will allow future migration of the instrument to the Cassegrain focal station.

The detector of OSIRIS consists of a mosaic of two Marconi CCD42-82 (2048×4096 pixels) with a 37 pix (binned) gap between them. The single pixel physical size is 15 μm, which corresponds to a scale of 0.127" in on the sky. However, OSIRIS standard observing modes use 0.254" binned pixels.
OSIRIS covers the wavelength range from $\lambda = 3650$ Å to $\lambda = 10000$ Å with a total field of view of 7.8×8.5 arcmin (7.8×7.8 arcmin unvignetted), and 7.5×6.0 arcmin, for direct imaging and multi-object spectroscopy respectively. The full

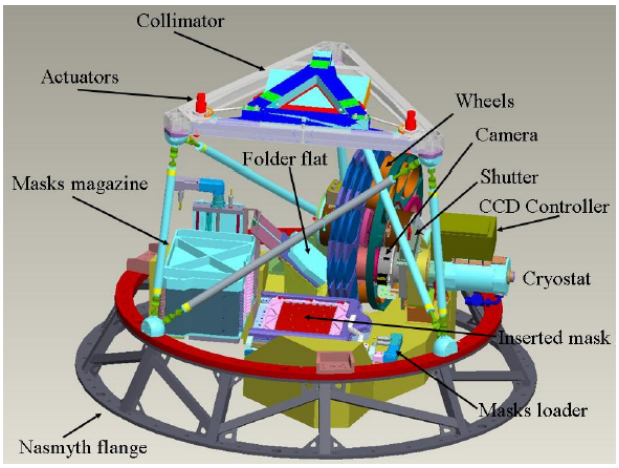

Figure A.9. 3D of OSIRIS showing the main subsystems.

spectral range is covered by the Sloan system broadband filters: u' (λ3500 Å), g' (λ4750 Å), r' (λ6300 Å), i' (λ7800 Å), z' (λ9250 Å).
Figure A.10 shows an image with the default pointing positions for all the OSIRIS observing modes: Broad Band imaging (1), Longslit Spectroscopy (2), and Tunable Filter Imaging (3) (the Tunable Filter's center and the MOS reference pointing are also shown). The OSIRIS standard pointing in Broad Band imaging mode is at the CCD2 pixel (256,1024) to maximize the available FOV and in order to avoid possible cosmetic effects, which are more abundant in the CCD1. The distance between the CCDs (gap) is 9.4" (approximately 37 pixels). This distance is measured in the central area of the CCDs, because it changes slightly from top to bottom (the CCD2 is inclined by about 0.04 degrees from the vertical direction). The CCD2 also is shifted about 0.5" (= 2 pix) down respect to the CCD1.

Some main characteristics of OSIRIS are summarized in Table A.1.

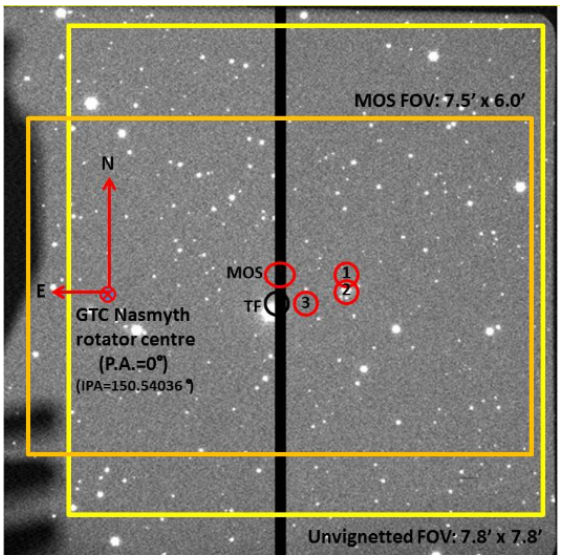

Figure A.10. OSIRIS CCDs mosaic. The image shows the default pointing positions for all the OSIRIS observing modes: Broad Band imaging (1), Longslit Spectroscopy (2), and Tunable Filter Imaging (3) (the Tunable Filter's center and the MOS reference pointing are also shown).

B

Pre-reduction

B.1 The process

BEFORE the data can be analysed, the images must be processed to remove artifacts introduced in the CCD camera by electronic readout noise, thermal electrons, and pixel-to-pixel sensitivity variations. The process of reduction of images consist of a set of passages which allow to transform the raw image obtained directly to the telescope in a scientific image, calibrated in physical units in which we can do the measures. The standard pre-reduction process can be summarized by the following equation:

$$scientific\ image = \frac{raw\ image - < bias >}{< (flat - < bias >)_{norm} >} \tag{B.1}$$

The basic steps of the reduction are as follows:

- Overscan and bias subtraction;
- Flat field correction;
- Fringe correction (only for i filter)

We performed the single steps of the pre-reduction using IRAF. [1]

[1] IRAF is an acronym for Image Reduction and Analysis Facility and is a collection of software written at the National Optical Astronomy Observatory (NOAO) geared towards the reduction of astronomical images in pixel array form.

B.1.1 Overscan and Bias

The first step before reducing the data is to determine which section of the image is the area of "overscan", which we refer to as "biassec". In addition it is necessary to determine the section that contains good data, that is to say without vignetting and outside of the section of "overscan", namely "trimsec". The level of zero can change throughout the night, so each image usually has an area where the zero level is stored, the so-called "overscan" zone. This area is formed by additional columns or rows, which usually contain all the images. These rows or columns are virtual, do not physically exist on the detector, being created artificially by the reading electronics, and therefore are not illuminated. However, this level is not representative of all pixels, but only a few columns or rows. If this section is available, it is usually calculate the average value of the counts and subtract this average value from each pixel of the scientific image. To evaluate zero level and its error, two methods can be used: the bias image or the overscan section.
A bias frame is essentially a zero-length exposure with the shutter closed and they are used to remove the readout signal from your camera sensor. Bias images should be taken every night of observation, as they may vary depending on temperature and other factors. Each pixel will have a slightly different value, but except for a small amount of noise, the value for any one pixel will be consistent from image to image. Since the bias is consistent from image to image it can be subtracted. The bias frame itself contains a small amount of readout noise. This readout noise is produced inside the electronics that read the pixels. It can be very low in sophisticated cameras, but it is never zero. This noise can be easily suppressed by combining a number of bias frames together (*master bias*).

B.1.2 Flat field

All the pixels making the CCD surface are almost similar; however, they present some variations of sensitivity: some of them will convert the light photons more efficiently into electrons than others. Also, the filters and lenses that are between the sky and the CCD can accumulate some dust particle, that will cast a shadow on the CCD. The result of all these effects is that the image of a uniformly illuminated target will not appear uniform on the CCD. To correct this effect, we take several images of a flat field (uniformly illuminated). A flat field image is taken while, for example, pointing the telescope at the sky at dusk or dawn (*sky flat*), or while pointing the telescope at a uniformly illuminated screen (*dome flat*). The scientific image should be divided into flat, but this must

be normalized first, because our flat image has a large number of counts per pixel (we took an image of a brightly illuminated screen), whereas our science images have relatively few counts per pixel (astronomical objects are faint). If we simply divide one by the other, we would drastically reduce the counts of the scientific image and lose the linear correspondence between the measured counts and the amount of light emitted by the source and incident on the CCD. To normalize the flat, it is divided by its average value. Now we need to combine the flats from each filter in order to obtain a *master flat* and then use them to map the sensitivity variations across the CCD (the images were divided by the master flat).

B.1.3 Fringe

The final step was to average all the images for the each filter, to obtain one final image for every exposure, i.e. long and short. In addition, for the i images we needed to remove the fringe pattern, which is very strong in the i band images acquired with this telescope, as shown in Fig. 3.2. Fringe is caused by multiple reflections of the interacting photon inside the CCD, and it affects more i than g photons. This effect can be corrected using specific IRAF pipelines, provided that the images were taken with a small dithering. Using the single long exposure images and the specific IRAF pipeline we created a fringe mask, which we subtracted from all the images. The result was satisfactory, as shown in Fig. B.1. Once we corrected the fringe pattern in all the i images, we averaged them to obtain one final image for every exposure, as in the case of the other bands.

B.1.4 Subaru/HST calibration

The images of Subaru and HTS Telescope are delivered calibrated therefore we did not to apply the pre-reduction process described above, just the photometry. In the case of HST, the images were pre-reduced by the HST team, using a specific calibration pipeline (see Section 4.2 for details).

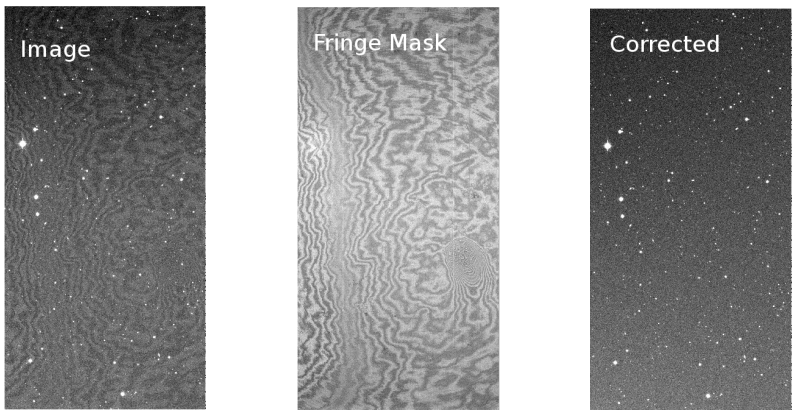

Figure B.1. Example for the fringe pattern correction for one image in the i band. *Left panel:* original image in the i band, corrected for bias and flat field. The fringe pattern is clearly visible in the image. *Middle panel:* evaluation of the fringe contribution using the set of images in the i band together with IRAF routines. *Right panel:* same image as in the left panel after applying the fringe correction. The result appears satisfactory. Using the same fringe mask all i images were corrected.

C

Photometry

C.1 Introduction

To measure brightnesses of point sources in CCD images, there are basically two methods: aperture photometry and PSF (Point Spread Function) fitting. In aperture photometry, one defines one aperture (usually circular) enclosing the source, and another (usually a ring outside the first) that contains only sky. One obtains the mean counts per pixel from the sky aperture, subtracts that mean from each pixel in the source aperture, and sums the remaining counts to find the total in the stellar image. The advantage of this technique is that it is simple; the primary disadvantage is that doing photometry on crowded star fields, such as globular clusters or open clusters, aperture photometry will not yield reliable results. If your stars are not substantially isolated on the sky, you will have overlapping PSFs, and aperture photometry will fail. It is better to use a Point Spread Function: a gaussian that can be fitted to all of the stars in the field in order to find their magnitudes.

Aperture correction is the different between PSF photometry and aperture photometry. The larger the aperture, the more of the flux from the star is within the aperture. But the larger the aperture, the larger is the error from the sky subtraction, and the more cosmic ray events will be within the aperture. Thus, the optimal aperture is one which is large enough to enclose most of the flux, but otherwise is as small as possible. The aperture correction is computed from a growth curve, i.e. a plot of magnitude within a given aperture versus aperture size.

C.2 DAOPHOT Photometry

The photometry of INT data and Boötes I has been done using DAOPHOT (Stetson, 1987) and its companion packages ALLSTAR and ALLFRAME (Stetson, 1994). DAOPHOT is a package for stellar photometry and astrometry developed to deal with crowded fields. It was developed by Peter B. Stetson at the Dominion Astronomical Observatory (DAO), and it is now available as "DAOPHOT II: The Next Generation". DAOPHOT identifies the brightness peaks in the frame, performs synthetic aperture photometry, and tries to estimate an accurate PSF.

Before I start up DAOPHOT I need to have some 'options' files which list the parameters DAOPHOT needs to run. At minimum I need to know: the read-noise and the gain of the detector, the FWHM of the sources in the image I wish to detect, and the maximum good value a pixel can have on the image. I created the text files (in the directory where I will be running DAOPHOT) called *daophot.opt*, *phot.opt*, *allstar.opt* and *allframe.opt*.

According to Stetson (2000), a typical DAOPHOT run in a crowded field can be summarized as follows (in the following the parameter's name and DAOPHOT commands are in capital letters):

- **Sky determination** (FIND). The average sky brightness is determined by the modal value in the sky annulus, whose radius is set by the user. The program provides also the standard deviations of the sky luminosity so estimated. The sky luminosity is then subtracted during the phase of photometry of the stars.
- **Stellar sources identification** (FIND). After having determined the luminosity of the sky the image is scanned pixel by pixel and the peaks of luminosity are detected at the confidence level selected by the user through the parameters contained in the daphot.opt file. The star detection threshold is set according to the gain and readout noise of the detector. The output is a file containing the stars coordinates.
- **Aperture Photometry** (PHOT). The first step is to set the radii of the apertures to perform the photometry of the star (or group of stars) and to fix inner and outer radii to estimate the luminosity of the sky in that region. DAOPHOT then performs the photometry adding the counts (ADU) within each aperture and removing the average luminosity of the sky which has been estimated in an annulus around the stellar image. There are two obvious drawbacks affecting aperture photometry: on one side in case of crowded images it is arduous to isolate the contribution of

each star to the luminosity of the image, on the other side, even in case of isolated images, photometry of faint objects, because the limited number of counts, is dominated by the error in the estimate of the background error and by fluctuations and statistics of the counts.

- **Create a list of PSF stars** (PICK). Once the aperture photometry has been performed, DAOPHOT selects a list of PSF stars. First, the task asks for an input file containing a list of positions and magnitudes: the aperture photometry file created with PHOT is ideal. The user set the number of PSF stars and the limiting instrumental magnitude for the faintest star he would like to consider using for the PSF. The routine then sorts the input star list by apparent magnitude (note that if you have set the HIGH GOOD DATUM parameter appropriately, any saturated stars should have magnitudes of 99.999 and will appear at the end of the list), and then it uses the FITTING RADIUS and the PSF RADIUS that the user has specified among the optional parameters to eliminate: (a) stars that are too close to the edge of the frame (within one FITTING RADIUS), and (b) stars that are too close to brighter stars or possibly saturated stars (within one PSF RADIUS plus one FITTING RADIUS). Any stars that remain after this culling process will be written out in order of increasing apparent magnitude, up to the number that the user has specified as a target. Stars fainter than the magnitude limit will be included only if otherwise there would be too few PSF stars to map out the degree of spatial variation that you specified with your "VARIABLE PSF" option.

- **PSF modeling** (PSF). DAOPHOT II offers a wider range of choices in modelling the points spread function. In particular, different numerical models besides the bivariate Gaussian function may be selected for the analytic first approximation. These are selected by the "ANALYTIC MODEL PSF". If the PSF routine discovers that a PSF star has a bad pixel (defined as being below the low good data value or above the HIGH GOOD DATUM value) inside one FITTING RADIUS of the star's centroid, it will refuse to use the star. If it discovers that the star has a bad pixel outside one FITTING RADIUS but inside a radius equal to (one PSF RADIUS plus two pixels), what it does again depends on the WATCH PROGRESS option. The value labeled "chi" represents the rootmean-square residuals of the actual brightness values contained within circles of radius one FITTING RADIUS about the centroids of the PSF stars. The analytic function that gives rise to a smaller "chi" value will be the one to be used

to construct our PSF.

- **PSF fitting** (ALLSTAR). This is a separate stand-alone program. ALLSTAR uses all the information collected in the former steps to perform an individual PSF fitting of all the sources. In each iteration, ALLSTAR subtracts all the stellar images from a working copy of the program image according to the current best guesses of their positions and magnitudes. The program then computes increments to the positions and magnitudes of the images from examination of the subtraction residuals around each position, and then checks each star to see whether it has converged or has become insignificant. When a star has converged, its results are written out and the star is subtracted permanently from the working copy of the image; when a star has disappeared it is discarded. Usually the procedure converges rapidly so that the image can be subtracted permanently from the working copy of the frame. After all the program stars have been subtracted from the original frame ALLSTAR memorizes the final image, which can be interactively analyzed to check the quality of the fit and the possible existence of not yet detected faint objects.

- **Create a list of stars for ALLFRAME** (DAOMATCH and DAOMASTER). The images are reduced one by one but the user usually want to combine photometry in each filter and match up stars in different filters to determine colours. This is done by DAOMATCH and DAOMASTER. Use DAOMATCH with .als files and produce a .mch file with the coordinate transformations. This is usually used as the first guess, to be fed into DAOMASTER. DAOMASTER takes the DAOMATCH .mch files with transformations and a list of .als files and (1) refines the transformationsusing all matched stars, (2) derives robust photometric offsets between frames and (3)correctly averages measurements.

- **Looking for the best PSF** (ALLFRAME). Up to this step the PSF fitting has been performed by ALLSTAR on single images. ALLFRAME is the final step of the procedure as it performs the simultaneous best fit of the stars in all the images, using the geometric and photometric information acquired in the previous steps. The pipeline DAOPHOT/ ALLSTAR/ DAOMASTER has produced different PSF stars list with the relative magnitude and the transformations from one frame to the other, ALLFRAME exploits all the information acquired to produce a list of stars to fit the same object simultaneously on all the frames. The key point of this package is the accuracy in the centroid determination, that allows an optimal fit of the stellar profile, which ensures precise estimates of the

deconvolution volume magnitudes. Moreover using all the images stacked together it is possible to reach a deeper photometric level and identify the faintest stars.

C.2.1 How to get a good PSF

Given the importance of this issue for the following discussion, it seems appropriate to discuss the adopted procedure in some detail. The PSF-fitting algorithms ALLSTAR/ALLFRAME require a good estimate of the PSFs on each frame. The first step is to select the stars to identify the PSF. The main criteria adopted to select PSF stars are:

- the stars should be bright, but the images should not be saturated, and they should have good shape parameters;
- the stars too near to the edge of the image are rejected;
- the stars should be isolated from other stars, especially the brighter ones, and not in region with a high crowding;
- the sample of stars selected should be distributed uniformly across the image.

The last point becomes fundamental when working in crowded fields, as it is the case for this thesis. In a crowded field the selection of the images is fundamental to derive the analytical expression of the PSF. We used a macro named *psffile.csh* that allows to change automatically the values of "ANALYTIC MODEL PSF" and "VARIABLE PSF" to obtain different PSF. I obtained the best PSF fitting using a "Penny" function, that is the sum of a Gaussian and a Lorentz function, having five free parameters. To perform a good PSF fitting on each image we used an iterative procedure. This procedure consists in working on an image where all the neighbors of the PSF stars have been subtracted (SUBSTAR) and the steps listed before are repeated on these new images. We took advantage of the interactivity of the program to check the list of PSF stars and reject not suitable candidates (as stars near the edge, or two stars which were too near to be distinguished by the program). The iteration allows ALLSTAR to give step by step a better determination of the centroids and as a consequence to perform an appropriate PSF fitting and, thus, a good photometry.

C.3 DOLPHOT Photometry

DOLPHOT (Dolphin, 2000) is a stellar photometry package that was adapted from HSTphot for general use. It currently supports two modes. One is a generic PSF-fitting package, which uses analytic PSF models and can be used for any camera. The second mode uses ACS PSFs and calibrations, and is effectively an ACS adaptation of HSTphot. The ACS module replaces the analytic PSF model with a lookup table computed using Tiny Tim PSFs. It also includes built-in CTE corrections and photometric calibrations, and thus serves as an ACS adaptation of HSTphot. For the ACS module to run correctly, data should be in the format they are obtained from the STScI archive so, as we mentioned before, we used `flc.fits/drc.fits` images.

Assuming that an appropriate reference image exists, the recipe for generating photometry is reasonably simple.

1. Run *acsmask* on all ACS images.
2. For ACS/WFC image, use *splitgroups* to split into *.chip1.fits and *.chip2.fits files.
3. Run *calsky* on each image to generate *.sky.fits files.
4. If not using UseWCS of 1 or 2 in DOLPHOT, run *acsfitdistort* to compute the alignment of each image to the reference.
5. Run dolphot.
6. If artificial star tests are to be run, use *acsfakelist* to generate the star list and re-run dolphot with the FakeStar parameter used to trigger artificial star mode.

C.3.1 *acsmask*: Mask Bad Pixels and Multiply Pixel Area Map (PAM)

```
acsmask -keepcr <fits files>
```

Acsmask takes as input FITS files in the format used by the STScI archive. (HRC images are 3-extension files; WFC images are 6-extension files. See the instrument handbook for details on what is contained in the extensions.) *Acsmask* masks out all pixels flagged as bad in the data quality image, and multiplies by the pixel areas so that the resulting images are approximately in units of electrons on the raw image. The `-keepcr` flag will cause acsmask to keep pixels

containing repaired cosmic rays (they are masked by default). This is useful if there are more than two subimages; otherwise it is generally best for the pixel to be ignored. The output image will have one extension if it is an HRC or drizzled image, or two if a WFC image.

C.3.2 *splitgroups*: Split WFC Chips

If you are using a drizzled reference image, you will need to split the WFC image files (which contain both chips) into two files, one for each chip. Assuming you have put your data into a working directory that contains only the data you will be photometering, typing `splitgroups *.fits` should convert all of your FITS files to single-chip format.

C.3.3 *calcsky*: Calculate Sky for Image

`calcsky <fits base>` $< r_{in} >$ $< r_{out} >$ `<step>` $< \sigma_{low} >$ $< \sigma_{high} >$

Calcsky creates a sky image, which depending on your DOLPHOT parameters can either provide an initial guess of the sky map or a definitive measurement. The sky computation is made by taking all pixels in an annulus around the pixel in question. The annulus extends from r_{in} to r_{out} pixels from the pixel whose value is being measured, and is sampled every step pixels. While step = 1 will always work, one can typically set step to the PSF size and achieve equally good results. The algorithm is a mean with iterative rejection. Each iteration, the mean and standard deviation are calculated, and values falling more than σ_{low} below or σ_{high} above the mean are rejected. This procedure continues until no pixels are rejected. After an initial sky map is calculated, it is boxcar smoothed with a kernel of size step. The resulting sky image is a FITS file named <fits base>.sky.fits.
Recommended parameters for WFC data are as follows:
$r_{in} = 15$
$r_{out} = 35$
step = 4 for an accurate sky map, or step = -128 for a quick one.
$\sigma_{low} = 2.25$
$\sigma_{high} = 2.00$

C.3.4 Running DOLPHOT

The workhorse of the DOLPHOT package is the routine *dolphot*.

```
dolphot <output> <options>
```

The output file contains the photometry. The options can be a combination of parameter files (-p<filename>) and parameter settings (<variable>=<value>). DOLPHOT's behavior is controlled by the parameters set in the parameter files. Following is a list of parameters and default values.
`Nimg :` Set the number of images to be photometered.
`img_file :` Specify base filename of image (the filename minus the .fits suffix).
`img_shift = 0 0:` Set offset of image relative to reference. This value can be an initial guess that is later adjusted by DOLPHOT. Values are x and y on the image minus x and y on the reference image. Note that this parameter should not be set for the reference image.
`img_xform = 1 0 0:` Set the scale ratio, cubic distortion, and rotation of the image relative to the reference image. This value can be an initial guess that is later adjusted by DOLPHOT. Note that this parameter should not be set for the reference image.

We set the parameter file following the recommended values for ACS/WFC (Dolphin, 2011).

```
RAper = 3       #photometry apeture size (flc)
Rchi = 2.0       #chi statistic apeture size (flc)
PSFPhot = 1       #photometry type (int/0=aper,1=psf,2=wtd-psf)
FitSky = 2       #fit sky?  (int/0=no,1=yes,2=small,3=with-phot)
RSky0 = 15       #inner sky radius (flc>=RAper+0.5)
Rsky1 = 35       #outer sky radius (flc>=RSky0+1)
SkipSky = 2       #spacing for sky measurement (int>0)
SkySig = 2.25       #sigma clipping for sky (flc>=1)
SecondPass = 5       #second pass finding stars (int 0=no,1=yes)
SearchMode = 1       #searching algorithm (int 0=S/N/chi,1=1/chi)
SigFind = 2.5       #sigma detection threshold (flc)
SigFindMult = 0.85       #Multiple for quick-and-dirty photometry (flc>0)
SigFinal = 3.5       #sigma output threshold (flc)
SubResRef = 1       #subpixel resolution for reference image (int>0)
MaxIT = 25       #maximum iterations (int>0)
NoiseMult = 0.10       #noise multiple in imgadd (flc)
FSat = 0.999       #fraction of saturate limit (flc)
FlagMask = 4       #Use Saturated Cores?  (4 if yes)
```

```
ApCor = 1       #find/make aperture corrections?  (int 0=no,1=yes)
Force1 = 1       #force type 1/2 (stars)?  (int 0=no,1=yes)
Align = 2       #align images?  (int 0=no,1=const,2=lin,3=cube)
Rotate = 1       #allow cross terms in alignment?  (int 0=no, 1=yes)
RCentroid = 1       #centroid box size (int>0)
PosStep = 0.25       #search step for position iterations (flc)
dPosMax = 2.5       #maximum single-step in position iterations (flc)
RCombine = 1.5     #minimum separation for two stars for cleaning (flc)
RPSF = 10       #PSF size (int>0)
SigPSF = 5.0       #min S/N for psf parameter (flc)
PSFres = 1       #make PSF residual image?  (int 0=no,1=yes)
psfoff = 0.0       #coordinate offset (PSF system - dolphot system)
DiagPlotType = PNG
UseWCS = 1
#UseACS = 1       #ACS PSF library
ACSpsfType = 0       #use Anderson PSF cores?  (int 0=no, 1=yes)
InterpPSFlib = 0
ACSuseCTE = 1
FakeStars= <filename>.crow
#FakeMatch
```

C.3.5 DOLPHOT Output

DOLPHOT's output is quite complex, but breaks into simple sections. All information for one star is contained on one line to facilitate the use of text utilities such as awk. An output file with the suffix of `columns` identifies the specific contents of each column of the output data; what follows is a description of the values rather than a specific ordered list. Positions are specified by extension number (zero if not in an extension), chip (for 3-D FITS images only), and X and Y position on the chip.

Fit quality can be estimated by several parameters given for the combined data as well as the per-chip data: χ, signal-to-noise, sharpness, roundness, major axis, crowding, and object type.

The sharpness is zero for a perfectly-fit star, positive for a star that is too sharp (perhaps a cosmic ray), and negative for a star that is too broad (perhaps a blend, cluster, or galaxy). In the uncrowded field, good stars should have sharpness values between -0.3 or 0.3.

The crowding parameter is in magnitudes, and tells how much brighter the star would have been measured had nearby stars not been fit simultaneously. For an isolated star, the value is zero. High crowding values are also generally

a sign of poorly-measured stars.

Object types are as follows:

- 1: good star
- 2: star too faint for PSF determination
- 3: elongated object
- 4: object too sharp
- 5: extended object

It goes without saying that anything fit as types 3, 4, or 5 should be excluded from photometry list.

After this come the blocks of photometry, one per image. Each photometry block contains all of the goodness of fit values listed above, plus counts, background, count rate, count rate uncertainty, magnitude, magnitude uncertainty, FWHM, PSF ellipticity, the three PSF parameters (a, b, and c), and error flag. Most of these are defined in the same way as described above.

An error flag of zero means the star was recovered extremely well in the image; other values added to the flag indicate the type of problem:

Object types are as follows:

- 1: photometry aperture extends off chip
- 2: too many bad or saturated pixels
- 4: saturated at center of star
- 8: extreme case of one of the above

In general, star errors of types 1-3 are usable; if the error flag is 4 or higher, it is unusable. Star errors of types 4-7 may be usable, if charge from the saturated pixels does not leak into adjacent pixels. If precision photometry is required, only error flags of zero or perhaps one should be used. There are a number of additional output files created. The most important is likely ¡output¿.info, which contains the general information for the image, including a listing of the photometry blocks as well as image alignments and aperture corrections.

An image residual and PSF residual (*.res.fits and *.psf.fits) show the subtracted image and PSF alterations. These are ordinary FITS files and can be viewed.

Two other files are useful for troubleshooting: <output>.apcor, and <output> .psfs. The aperture correction file lists image number (starting from 0), chip,

X, Y, PSF-fit magnitude, aperture correction to 0.5 arcsec, uncertainty, and weight. Finally the PSF star file lists the PSF stars, followed by values of 0 or 1 to tell whether they were (1) or were not (0) used for each image.

As with all photometry, you will need to trim your detection list to eliminate objects classified as non-stellar, low signal-to-noise, or bad photometry quality.

D

The Star Formation History

D.1 Deriving the star formation history: the method

THE star formation history (SFH) is a powerful tool to derive fundamental properties of galaxies and their evolution. The IAC method to solve the SFH is based on three main codes developed by members of our team. The flow chart summarising a standard execution is shown in Figure D.1.

The entire procedure can be divided into five steps:

1. *The synthetic CMD.* It is created using IAC-star (Aparicio & Gallart, 2004). The requested inputs are as follows.
   (a) A set of theoretical stellar evolution models. We adopted the BaSTI evolutionary library (Pietrinferni et al., 2006).
   (b) A set of bolometric corrections.
   (c) No a priori age–metallicity relation is adopted: the number of stars is constant as a function of age, in the range $2 < t < 15$ Gyr, and of metallicity, for $0.00001 < Z < 0.001$.
   (d) The initial mass function (IMF), taken from Kroupa (2002). This is expressed with the formula $N(m)dm = m^{-\alpha}dm$, where $\alpha = 1.3$ for stars with mass smaller than 0.5 $M_{\odot}$, and $\alpha = 2.3$ for stars of higher mass.
   (e) The binary fraction, β, and the relative mass distribution of binary stars.
   (f) The assumed mass loss during the RGB phase follows the empirical relation by Reimers (1975), with efficiency $\eta = 0.35$.

2. *The observational effects simulation.* The code to simulate the observational effects in the synthetic CMD, called *obsersin*, has been developed by Hidalgo et al. (2011). This is a fundamental step because the distribution of stars in the observed CMD is strongly modified from the actual distribution due to the observational errors, particularly at the faint magnitude level near the old TO, which is where most of the information on the most ancient star formation is encoded.

3. *Parameterization.* MinnIAC is a suite of routines developed specifically to accomplish this purpose. "Parameterization" of the CMD means two things: (1) defining the age and metallicity bins that fix the simple populations and (2) defining a grid of boxes covering critical evolutionary phases in the CMDs, where the stars of the observed and model CMD are counted.

4. *Solving.* IAC-pop (Aparicio & Hidalgo, 2009) is a code designed to solve the SFH of a resolved stellar system.

5. *Averaging.* A posteriori, MinnIAC was also used to read the individual solutions, and calculate the mean best SFH.

A brief description of the characteristics of the single codes are listed in the following:

- **IAC-star (Aparicio & Gallart, 2004).** The code IAC-star generates synthetic HR and color-magnitude diagrams (CMDs) and is mainly aimed at star formation history studies in nearby galaxies. Composite stellar populations are calculated on a star-by-star basis, by computing the luminosity, effective temperature, and gravity of each star by direct bi-logarithmic interpolation in the metallicity and age grid of a library of stellar evolution tracks. It also provides integrated masses, luminosities, and magnitudes, as well as surface brightness fluctuation luminosities and magnitudes for the total synthetic stellar population, and therefore it can also be used for population synthesis research. Trying to be as general as possible, IAC-star offers the possibility to choose between a variety of stellar evolutionary and bolometric correction libraries, SFRs, chemical enrichment laws, and model functions such as IMFs and fraction of binary stars. Stars with age and metallicity following a continuous distribution are computed through interpolation in a stellar evolution library (e.g. BaSTI by Pietrinferni et al. 2004, Padova by Girardi et al. 2000). The mass loss is computed along the RGB and AGB phases. The bolometric correction library provides

colours and magnitudes of the stars as a function of their age, mass, and metallicity. Depending on the bolometric correction library, the colours and magnitudes are given in visual broadband, infrared, and HST filters (e.g. Castelli & Kurucz 2003 for the visual regime, Origlia & Leitherer 2000 for the HST filters). Thus, the output is a synthetic CMDs with smooth, realistic stellar distributions. This is the first fundamental element to obtain the SFH. For a full description see (Aparicio & Gallart, 2004).

- **IAC-pop (Aparicio & Hidalgo, 2009).** IAC-pop is a code designed to solve the SFH of a complex stellar population system, like a galaxy, from the comparison of observed and synthetic CMDs. Considering that time and metallicity are the most important variables in the problem, we define the SFH as a function of both. We will use two definitions, one in terms of the number of formed stars and another in terms of the gas mass converted into stars. Formally, $\psi(t,z)dtdz$ is the number of stars formed at time t' in the interval $t < t' \leq t + dt$ and with metallicity z' in the interval $z < z' \leq z + dz$, per unit time and metallicity. This function can be identified with the usual definitions of the star formation rate (SFR), as a function of time and metallicity. In addition, the solution of the SFH depends on other parameters, namely the model functions (i.e. IMF and the fraction of binary stars) and external parameters (i.e. photometric zeropoint, distance to the studied object and its reddening). However, the strongest limitation on the observational information is produced by the observational effects that will be discussed in Section D.2. The first step is to create a synthetic CMD (sCMD), as those generate by IAC-star, with a large number of stars, which span an age and a metallicity range. This range has to cover all the possible ages and metallicities of the stars in the studied stellar system. Observational effects (crowding, blending, external errors, etc.) should be simulated in the synthetic CMD. The stars in the sCMD are divided into a number of simple models, i.e. single populations ψ_i each one in a small bin of age and metallicity. They constitute a set of $n \times m$ models with no star in common between any two of them. In the CMD several regions, called *bundles*, are defined. Every bundle is sampled with a uniform grid, whose dimension can vary from one bundle to the other. In every box j and simple stellar population i, the number of stars, M_i^j, is computed. The same is done in the observed CMD, producing the array O_j, containing the number of observed stars in the box j. This step defines the parameterization of the CMD. With the former information, the distribution of stars in the CMD boxes can be

calculated for any model SFH as a linear combination of the M_i^j values:

$$M^j = A\sum_i \alpha_i M_i^j \tag{D.1}$$

where A is a scaling factor, and $\alpha_i \geq 0$. The CMD, M^j , best matching the distribution of stars O^j in the observed CMD is found using a merit function. A merit function is a function that measures the agreement between data and the fitting model for a particular choice of the parameters. In particular Mighell's χ^2_γ is used:

$$\chi^2_\gamma = \sum_j \frac{(O^j + min(O^j, 1) - M^j)^2}{O^j + 1} \tag{D.2}$$

We will use $\chi^2_\upsilon = \chi^2\gamma/\upsilon$, where υ is the number of freedom degrees. Minimization of χ^2_υ provides the best solution as a set of α_i values as well as a test on whether it is good enough. IAC-pop makes use of a genetic algorithm for an efficient searching of the χ^2_υ minimum. The solution SFH can be written as

$$\psi(t, z) = A\sum_i \alpha_i \psi_i, \tag{D.3}$$

where ψ_i refers to partial model i, with i taking values from 1 to $n \times m$, and A is a scaling constant. The solutions produced by IAC-pop depend on several input functions and parameters. These are the *model functions*, *external parameters*, *sampling parameters* (i.e. the bundles and the grid arrays for sampling the CMDs). In order to minimize the effects of these, many IAC-pop runs with different inputs are in general needed. All these solutions are averaged by MinnIAC.

- **MinnIAC (Hidalgo et al., 2011).** MinnIAC (from *Minne*sota and *IAC*) is a set of routines developed specifically to manage the process of selection of sampling parameters, creating input data sets, and averaging solutions. More in detail, MinnIAC is used for two tasks. First, to divide the sCMD in the corresponding single stellar populations CMDs according to the selected age and metallicity bins. Second, to define the bundles

and box grids in the CMDs and to count stars in them. With this information, MinnIAC creates the input files for each IAC-pop run. Once all the solutions have been obtained, MinnIAC averages them and computes errors for each age and metallicity interval as the root mean square of the solutions.

The method is more effective if the regions of the CMD more sensitive to evolutionary phases and better known in stellar evolutionary theories are considered, e.g. the MS TO. In fact, one of the fundamental requirements to obtain a detailed SFH is that this region should be well described. Therefore the use of deep photometric data is highly encouraged to obtain a good SFH.

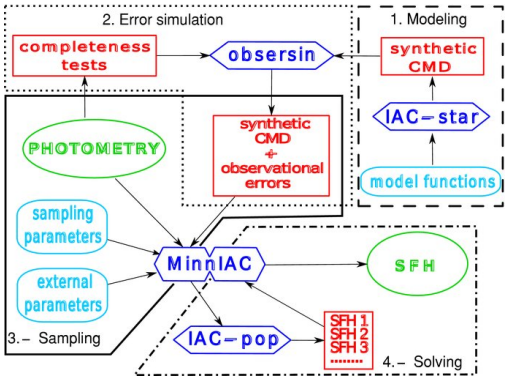

Figure D.1. Figure from Hidalgo et al. (2011). The flow chart shown summarises how the SFH solution is obtained. For further details see the text Hidalgo et al. (2011) and references therein. *Model functions* are the IMF and binary fraction. *External parameters* are distance and reddening to a galaxy. *Sampling parameters* are the bundles and the grid arrays for sampling the CMDs.

D.2 Characterisation of observational effects

The strongest limitation on the observational information is produced by the observational effects. These include all the factors affecting and distorting the observational material, namely, the signal-to-noise limitations, the defects of the detector, and the crowding and blending between stars. The consequences are

loss of stars, changes in measured stellar colors and magnitudes, and external errors larger and more difficult to control than internal ones. The best way to test how all these effects influence the SFH solution is working with synthetic CMDs, in which they have been simulated. Hidalgo et al. (2011) provide a detailed description of the procedures I adopted for the characterization and simulation of these observational effects. To characterize the observational effect, I adopted the standard method of artificial (or false) stars. I added a number of stars per field, placing them in a regular grid. The distance between two artificial stars was fixed in order to pack the largest number of stars but at the same time to ensure that the synthetic stars were not affecting each other. This value was chosen to be $R = 2R_{PSF} + 1$, where R_{PSF} is the PSF radius. In this way, the overlap of the wings of the artificial stars was minimized to avoid influencing the fit in the core of the PSF. With this criterion, taking into account the size of the CCD, the number of injected stars does not significantly alter the original crowding. In each iteration, the grid was moved by a few pixels, to better sample the crowding characteristics of the image.

Synthetic stars were randomly and uniformly distributed in order to cover the full colour and magnitude ranges of the observed stars. I set the limit in magnitude of the injected stars ~ 1 mag below the photometric limit. The photometry was then repeated with the same parameters and the same PSF of the original images. The same procedure was adopted for the three galaxies studied here.

Once the procedure is concluded the completeness can be evaluated. The completeness is defined as follows

$$Completeness = \frac{N_r}{N_i} \tag{D.4}$$

where N_r and N_i are the number of recovered and injected stars, respectively.

To derive the SFH, the observational effects need to be simulated in the sCMD. For this purpose, the IAC method uses an additional specific routine, *obsersin*. This code uses the unrecovered false stars and the difference between the injected (m_i) and measured magnitudes (m_r) of the recovered stars for the simulation. In addition, as the crowding changes depending on the density of stars, I also used the spatial dependency of the crowding. Since the density of stars (and thus the amount of crowding) normally varies substantially across the galaxy's field, spatial information has also been taken into account in the completeness test.

In short, for each synthetic star generated by IAC-star, of magnitude m_s a list of false stars with $|m_i - m_s| \leq \epsilon_m$ and $r \leq \epsilon_r$ is created for each filter. ϵ_m and

ϵ_r are free parameters set by the user, while r is the spatial distance between the synthetic and the false star. If the number of false stars selected in this way, in common to both filters, is < 10, the parameters ϵ_m and ϵ_r are increased in turn until 10 or more false stars are found. Then, one of them is randomly selected from this list. If that star was unrecovered, the synthetic star is eliminated from the sCMD. If the selected star was recovered and m'_i and m'_r are its injected and recovered magnitudes in a given filter, then $m^e_s = m_s + m'_i - m'_r$ will be the magnitude of the synthetic star with observational effects simulated. The same is done for both filters. Further details on the code are given in Hidalgo et al. (2011).

Bibliography

Abazajian, K., Adelman-McCarthy, J. K., Agüeros, M. A., et al. 2004, AJ, 128, 502

Alvarez, M. A., Busha, M., Abel, T., & Wechsler, R. H. 2009, ApJ, 703, L167

Aparicio, A., & Gallart, C. 1995, AJ, 110, 2105

—. 2004, AJ, 128, 1465

Aparicio, A., & Hidalgo, S. L. 2009, AJ, 138, 558

Aparicio, A., Hidalgo, S. L., Skillman, E., et al. 2016, ApJ, 823, 9

Avila, R., et al. 2017, "ACS Instrument Handbook", Version 16.0 (Baltimore: STScI)

Bailin, J., & Ford, A. 2007, MNRAS, 375, L41

Bailyn, C. D. 1995, ARA&A, 33, 133

Balbinot, E., Santiago, B. X., da Costa, L., et al. 2013, ApJ, 767, 101

Barkana, R., & Loeb, A. 1999, ApJ, 523, 54

Barnes, D. G., Staveley-Smith, L., de Blok, W. J. G., et al. 2001, MNRAS, 322, 486

Bechtol, K., Drlica-Wagner, A., Balbinot, E., et al. 2015, ApJ, 807, 50

Becker, R. H., Fan, X., White, R. L., et al. 2001, AJ, 122, 2850

Bellini, A., Bedin, L. R., Piotto, G., et al. 2010, AJ, 140, 631

Bellini, A., Piotto, G., Milone, A. P., et al. 2013, ApJ, 765, 32

Belokurov, V. 2013, New A Rev., 57, 100

Belokurov, V., Irwin, M. J., Koposov, S. E., et al. 2014, MNRAS, 441, 2124

Belokurov, V., Zucker, D. B., Evans, N. W., et al. 2006, ApJ, 647, L111

—. 2007, ApJ, 654, 897

Belokurov, V., Walker, M. G., Evans, N. W., et al. 2008, ApJ, 686, L83

—. 2009, MNRAS, 397, 1748

—. 2010, ApJ, 712, L103

Benítez-Llambay, A., Navarro, J. F., Abadi, M. G., et al. 2015, MNRAS, 450, 4207

Benson, A. J., Frenk, C. S., Lacey, C. G., Baugh, C. M., & Cole, S. 2002, MNRAS, 333, 177

Blumenthal, G. R., Faber, S. M., Primack, J. R., & Rees, M. J. 1984, Nature, 311, 517

—. 1985, Nature, 313, 72

Bovill, M. S., & Ricotti, M. 2009, ApJ, 693, 1859

—. 2011, ApJ, 741, 18

Boylan-Kolchin, M., Bullock, J. S., & Kaplinghat, M. 2011, MNRAS, 415, L40

—. 2012, MNRAS, 422, 1203

Boylan-Kolchin, M., Weisz, D. R., Johnson, B. D., et al. 2015, MNRAS, 453, 1503

Brook, C. B., & Di Cintio, A. 2015, MNRAS, 450, 3920

Brooks, A. M., Kuhlen, M., Zolotov, A., & Hooper, D. 2013, ApJ, 765, 22

Brown, T. M., Tumlinson, J., Geha, M., et al. 2012, ApJ, 753, L21

—. 2014, ApJ, 796, 91

Bullock, J. S., Kravtsov, A. V., & Weinberg, D. H. 2000, ApJ, 539, 517

Cabrera-Lavers, A. 2014, "OSIRIS USER MANUAL", Version 3.1

Calura, F., Pipino, A., Chiappini, C., Matteucci, F., & Maiolino, R. 2009, A&A, 504, 373

Carretta, E., Bragaglia, A., Gratton, R. G., et al. 2009, A&A, 505, 117

Cassisi, S., Mucciarelli, A., Pietrinferni, A., Salaris, M., & Ferguson, J. 2013, A&A, 554, A19

Cassisi, S., & Salaris, M. 2014, A&A, 563, A10

Castelli, F., & Kurucz, R. L. 2003, in IAU Symposium, Vol. 210, Modelling of Stellar Atmospheres, ed. N. Piskunov, W. W. Weiss, & D. F. Gray, A20

Chan, T. K., Kereš, D., Oñorbe, J., et al. 2015, MNRAS, 454, 2981

Colín, P., Klypin, A. A., & Kravtsov, A. V. 2000, ApJ, 539, 561

Dall'Ora, M., Clementini, G., Kinemuchi, K., et al. 2006, ApJ, 653, L109

de Jong, J. T. A., Martin, N. F., Rix, H.-W., et al. 2010, ApJ, 710, 1664

de Jong, J. T. A., Rix, H.-W., Martin, N. F., et al. 2008, AJ, 135, 1361

Dekel, A., & Silk, J. 1986, ApJ, 303, 39

Dekel, A., & Woo, J. 2003, MNRAS, 344, 1131

Di Cintio, A., Brook, C. B., Macciò, A. V., et al. 2014, MNRAS, 437, 415

Dodelson, S., & Widrow, L. M. 1994, Physical Review Letters, 72, 17

Dolphin, A. 2011, "DOLPHOT/ACS User's Guide", Version 2.0

Dolphin, A. E. 2000, PASP, 112, 1383

Drlica-Wagner, A., Bechtol, K., Rykoff, E. S., et al. 2015, ApJ, 813, 109

Drlica-Wagner, A., Bechtol, K., Allam, S., et al. 2016, ApJ, 833, L5

Dubinski, J., & Carlberg, R. G. 1991, ApJ, 378, 496

Dutton, A. A., Macciò, A. V., Frings, J., et al. 2016, MNRAS, 457, L74

Efstathiou, G. 1992, MNRAS, 256, 43P

Fellhauer, M., Wilkinson, M. I., Evans, N. W., et al. 2008, MNRAS, 385, 1095

Ferrero, I., Abadi, M. G., Navarro, J. F., Sales, L. V., & Gurovich, S. 2012, MNRAS, 425, 2817

Flores, R. A., & Primack, J. R. 1994, ApJ, 427, L1

Frebel, A., & Norris, J. E. 2015, ARA&A, 53, 631

Frebel, A., Simon, J. D., Geha, M., & Willman, B. 2010, ApJ, 708, 560

Fukugita, M., Ichikawa, T., Gunn, J. E., et al. 1996, AJ, 111, 1748

Gallart, C., Zoccali, M., & Aparicio, A. 2005, ARA&A, 43, 387

Gallazzi, A., Charlot, S., Brinchmann, J., White, S. D. M., & Tremonti, C. A. 2005, MNRAS, 362, 41

Garnett, D. R. 2002, ApJ, 581, 1019

Garrison-Kimmel, S., Boylan-Kolchin, M., Bullock, J. S., & Kirby, E. N. 2014, MNRAS, 444, 222

Gilmore, G., Norris, J. E., Monaco, L., et al. 2013, ApJ, 763, 61

Giovanelli, R., Haynes, M. P., Kent, B. R., et al. 2005, AJ, 130, 2613

Girardi, L., Bressan, A., Bertelli, G., & Chiosi, C. 2000, A&AS, 141, 371

Gnedin, N. Y. 2000, ApJ, 542, 535

Gnedin, N. Y., & Kravtsov, A. V. 2006, ApJ, 645, 1054

Governato, F., Willman, B., Mayer, L., et al. 2007, MNRAS, 374, 1479

Governato, F., Brook, C., Mayer, L., et al. 2010, Nature, 463, 203

Governato, F., Zolotov, A., Pontzen, A., et al. 2012, MNRAS, 422, 1231

Gratton, R. G., Carretta, E., & Bragaglia, A. 2012, A&A Rev., 20, 50

Grebel, E. K., & Chu, Y.-H. 2000, AJ, 119, 787

Grebel, E. K., & Gallagher, III, J. S. 2004, ApJ, 610, L89

Greco, C., Dall'Ora, M., Clementini, G., et al. 2008, ApJ, 675, L73

Harris, W. E. 1996, AJ, 112, 1487

Hidalgo, S., & Aparicio, A. 2016, Mem. Soc. Astron. Italiana, 87, 350

Hidalgo, S. L., Aparicio, A., Martínez-Delgado, D., & Gallart, C. 2009, ApJ, 705, 704

Hidalgo, S. L., Aparicio, A., Skillman, E., et al. 2011, ApJ, 730, 14

Hidalgo, S. L., Monelli, M., Aparicio, A., et al. 2013, ApJ, 778, 103

Hodge, P. 1989, ARA&A, 27, 139

Hoeft, M., Yepes, G., Gottlöber, S., & Springel, V. 2006, MNRAS, 371, 401

Hooper, D., Kaplinghat, M., Strigari, L. E., & Zurek, K. M. 2007, Phys. Rev. D, 76, 103515

Irwin, M. J., Belokurov, V., Evans, N. W., et al. 2007, ApJ, 656, L13

Karachentsev, I. D., & Kaisina, E. I. 2013, AJ, 146, 46

Katz, H., & Ricotti, M. 2013, MNRAS, 432, 3250

—. 2014, MNRAS, 444, 2377

Kazantzidis, S., Łokas, E. L., & Mayer, L. 2013, ApJ, 764, L29

Kim, D., & Jerjen, H. 2015, ApJ, 808, L39

Kim, D., Jerjen, H., Mackey, D., Da Costa, G. S., & Milone, A. P. 2015, ApJ, 804, L44

Kirby, E. N., Cohen, J. G., Guhathakurta, P., et al. 2013, ApJ, 779, 102

Kirby, E. N., Cohen, J. G., Smith, G. H., et al. 2011, ApJ, 727, 79

Kirby, E. N., Guhathakurta, P., Bolte, M., Sneden, C., & Geha, M. C. 2009, ApJ, 705, 328

Kirby, E. N., Simon, J. D., Geha, M., Guhathakurta, P., & Frebel, A. 2008, ApJ, 685, L43

Kleyna, J. T., Wilkinson, M. I., Evans, N. W., & Gilmore, G. 2005, ApJ, 630, L141

Klypin, A., Karachentsev, I., Makarov, D., & Nasonova, O. 2015, MNRAS, 454, 1798

Klypin, A., Kravtsov, A. V., Valenzuela, O., & Prada, F. 1999, ApJ, 522, 82

Koposov, S., de Jong, J. T. A., Belokurov, V., et al. 2007, ApJ, 669, 337

Koposov, S., Belokurov, V., Evans, N. W., et al. 2008, ApJ, 686, 279

Koposov, S. E., Belokurov, V., & Torrealba, G. 2017, MNRAS, 470, 2702

Koposov, S. E., Belokurov, V., Torrealba, G., & Evans, N. W. 2015a, ApJ, 805, 130

Koposov, S. E., Yoo, J., Rix, H.-W., et al. 2009, ApJ, 696, 2179

Koposov, S. E., Gilmore, G., Walker, M. G., et al. 2011, ApJ, 736, 146

Koposov, S. E., Casey, A. R., Belokurov, V., et al. 2015b, ApJ, 811, 62

Koposov, S. E., Walker, M. G., Belokurov, V., et al. 2018, ArXiv e-prints, arXiv:1804.06430

Köppen, J., Weidner, C., & Kroupa, P. 2007, MNRAS, 375, 673

Kroupa, P. 2001, MNRAS, 322, 231

—. 2002, Science, 295, 82

Laevens, B. P. M., Martin, N. F., Sesar, B., et al. 2014, ApJ, 786, L3

Laevens, B. P. M., Martin, N. F., Ibata, R. A., et al. 2015a, ApJ, 802, L18

Laevens, B. P. M., Martin, N. F., Bernard, E. J., et al. 2015b, ApJ, 813, 44

Lai, D. K., Lee, Y. S., Bolte, M., et al. 2011, ApJ, 738, 51

Landolt, A. U. 2009, AJ, 137, 4186

Lanfranchi, G. A., & Matteucci, F. 2004, MNRAS, 351, 1338

Lapi, A., Mancuso, C., Celotti, A., & Danese, L. 2017, ApJ, 835, 37

Leitherer, C., Schaerer, D., Goldader, J. D., et al. 1999, ApJS, 123, 3

Liu, C., Hu, J., Newberg, H., & Zhao, Y. 2008, A&A, 477, 139

Lovell, M. R., Eke, V., Frenk, C. S., et al. 2012, MNRAS, 420, 2318

Lucas, R. A., e. a. 2016, "ACS Data Handbook", Version 8.0 (Baltimore: STScI)

Mac Low, M.-M., & Ferrara, A. 1999, ApJ, 513, 142

Macciò, A. V., & Fontanot, F. 2010, MNRAS, 404, L16

Madau, P., Kuhlen, M., Diemand, J., et al. 2008, ApJ, 689, L41

Madau, P., Shen, S., & Governato, F. 2014, ApJ, 789, L17

Magrini, L., Hunt, L., Galli, D., et al. 2012, MNRAS, 427, 1075

Mapelli, M., Ripamonti, E., Tolstoy, E., et al. 2007, MNRAS, 380, 1127

Marigo, P., Girardi, L., Bressan, A., et al. 2008, A&A, 482, 883

Martin, N. F., de Jong, J. T. A., & Rix, H.-W. 2008a, ApJ, 684, 1075

Martin, N. F., Ibata, R. A., Chapman, S. C., Irwin, M., & Lewis, G. F. 2007, MNRAS, 380, 281

Martin, N. F., Coleman, M. G., De Jong, J. T. A., et al. 2008b, ApJ, 672, L13

Martin, N. F., Schlafly, E. F., Slater, C. T., et al. 2013, ApJ, 779, L10

Martin, N. F., Nidever, D. L., Besla, G., et al. 2015, ApJ, 804, L5

Mashchenko, S., Wadsley, J., & Couchman, H. M. P. 2008, Science, 319, 174

Mateo, M. L. 1998, ARA&A, 36, 435

Matteucci, F. 1994, A&A, 288, 57

Mayer, L., Governato, F., Colpi, M., et al. 2001, ApJ, 547, L123

McConnachie, A. W. 2012, AJ, 144, 4

Milone, A. P., Marino, A. F., Piotto, G., et al. 2012a, ApJ, 745, 27

Milone, A. P., Piotto, G., King, I. R., et al. 2010, ApJ, 709, 1183

Milone, A. P., Piotto, G., Bedin, L. R., et al. 2012b, ApJ, 744, 58

Milone, A. P., Marino, A. F., Piotto, G., et al. 2013, ApJ, 767, 120

—. 2015, MNRAS, 447, 927

Miyazaki, S., Komiyama, Y., Sekiguchi, M., et al. 2002, PASJ, 54, 833

Monelli, M., Hidalgo, S. L., Stetson, P. B., et al. 2010a, ApJ, 720, 1225

Monelli, M., Gallart, C., Hidalgo, S. L., et al. 2010b, ApJ, 722, 1864

Monelli, M., Milone, A. P., Stetson, P. B., et al. 2013, MNRAS, 431, 2126

Moore, B. 1994, Nature, 370, 629

Moore, B., Ghigna, S., Governato, F., et al. 1999, ApJ, 524, L19

Moore, B., Governato, F., Quinn, T., Stadel, J., & Lake, G. 1998, ApJ, 499, L5

Moretti, M. I., Dall'Ora, M., Ripepi, V., et al. 2009, ApJ, 699, L125

Mould, J. R., Kristian, J., & Da Costa, G. S. 1983, ApJ, 270, 471

Muñoz, R. R., Carlin, J. L., Frinchaboy, P. M., et al. 2006, ApJ, 650, L51

Navarro, J. F., Frenk, C. S., & White, S. D. M. 1995, MNRAS, 275, 56

—. 1996, ApJ, 462, 563

—. 1997, ApJ, 490, 493

Navarro, J. F., & Steinmetz, M. 1997, ApJ, 478, 13

Oñorbe, J., Boylan-Kolchin, M., Bullock, J. S., et al. 2015, MNRAS, 454, 2092

Oh, S.-H., Hunter, D. A., Brinks, E., et al. 2015, AJ, 149, 180

Okamoto, S., Arimoto, N., Yamada, Y., & Onodera, M. 2008a, A&A, 487, 103

—. 2012, ApJ, 744, 96

Okamoto, T., Gao, L., & Theuns, T. 2008b, MNRAS, 390, 920

Origlia, L., & Leitherer, C. 2000, AJ, 119, 2018

Pagels, H., & Primack, J. R. 1982, Physical Review Letters, 48, 223

Papastergis, E., Giovanelli, R., Haynes, M. P., & Shankar, F. 2015, A&A, 574, A113

Papastergis, E., Martin, A. M., Giovanelli, R., & Haynes, M. P. 2011, ApJ, 739, 38

Paust, N. E. Q., Chaboyer, B., & Sarajedini, A. 2007, AJ, 133, 2787

Peñarrubia, J., Pontzen, A., Walker, M. G., & Koposov, S. E. 2012, ApJ, 759, L42

Peebles, P. J. E. 1984, ApJ, 277, 470

Perlmutter, S., Aldering, G., Goldhaber, G., et al. 1999, ApJ, 517, 565

Pfrommer, C., Chang, P., & Broderick, A. E. 2012, ApJ, 752, 24

Pietrinferni, A., Cassisi, S., Salaris, M., & Castelli, F. 2004, ApJ, 612, 168

—. 2006, ApJ, 642, 797

Piotto, G., Milone, A. P., Marino, A. F., et al. 2013, ApJ, 775, 15

Piotto, G., De Angeli, F., King, I. R., et al. 2004, ApJ, 604, L109

Piotto, G., Bedin, L. R., Anderson, J., et al. 2007, ApJ, 661, L53

Piotto, G., Milone, A. P., Anderson, J., et al. 2012, ApJ, 760, 39

Piotto, G., Milone, A. P., Bedin, L. R., et al. 2015, AJ, 149, 91

Pipino, A., Calura, F., & Matteucci, F. 2013, MNRAS, 432, 2541

Planck Collaboration, Ade, P. A. R., Aghanim, N., et al. 2014, A&A, 571, A16

—. 2016, A&A, 594, A13

Pontzen, A., & Governato, F. 2012, MNRAS, 421, 3464

Purcell, C. W., & Zentner, A. R. 2012, J. Cosmology Astropart. Phys., 12, 007

Quinn, T., Katz, N., & Efstathiou, G. 1996, MNRAS, 278, L49

Rashkov, V., Madau, P., Kuhlen, M., & Diemand, J. 2012, ApJ, 745, 142

Reimers, D. 1975, Memoires of the Societe Royale des Sciences de Liege, 8, 369

Ricotti, M. 2002, MNRAS, 336, L33

Ricotti, M., & Gnedin, N. Y. 2005, ApJ, 629, 259

Ricotti, M., Parry, O. H., & Gnedin, N. Y. 2016, ApJ, 831, 204

Riess, A. G., Filippenko, A. V., Challis, P., et al. 1998, AJ, 116, 1009

Sakamoto, T., & Hasegawa, T. 2006, ApJ, 653, L29

Salaris, M., & Cassisi, S. 2005, Evolution of Stars and Stellar Populations, 400

Salvadori, S., & Ferrara, A. 2009, MNRAS, 395, L6

Samushia, L., Reid, B. A., White, M., et al. 2013, MNRAS, 429, 1514

Sand, D. J., Seth, A., Olszewski, E. W., et al. 2010, ApJ, 718, 530

Sand, D. J., Strader, J., Willman, B., et al. 2012, ApJ, 756, 79

Santana, F. A., Muñoz, R. R., Geha, M., et al. 2013, ApJ, 774, 106

Sawala, T., Scannapieco, C., Maio, U., & White, S. 2010, MNRAS, 402, 1599

Sawala, T., Frenk, C. S., Fattahi, A., et al. 2015, MNRAS, 448, 2941

Sbordone, L., Salaris, M., Weiss, A., & Cassisi, S. 2011, A&A, 534, A9

Schlafly, E. F., & Finkbeiner, D. P. 2011, ApJ, 737, 103

Shen, S., Madau, P., Conroy, C., Governato, F., & Mayer, L. 2014, ApJ, 792, 99

Shetrone, M., Venn, K. A., Tolstoy, E., et al. 2003, AJ, 125, 684

Siegel, M. H. 2006, ApJ, 649, L83

Silich, S., & Tenorio-Tagle, G. 2001, ApJ, 552, 91

Simon, J. D., & Geha, M. 2007, ApJ, 670, 313

Skillman, E. D., Kennicutt, R. C., & Hodge, P. W. 1989, ApJ, 347, 875

Smith, J. A., Tucker, D. L., Kent, S., et al. 2002, AJ, 123, 2121

Spergel, D. N., Bean, R., Doré, O., et al. 2007, ApJS, 170, 377

Stetson, P. B. 1987, PASP, 99, 191

—. 1994, PASP, 106, 250

—. 2000, "User's Manual for DAOPHOT II", (Dominion Astrophysical Observatory)

Tammann, G. A. 1994, in European Southern Observatory Conference and Workshop Proceedings, Vol. 49, European Southern Observatory Conference and Workshop Proceedings, ed. G. Meylan & P. Prugniel, 3

Thoul, A. A., & Weinberg, D. H. 1996, ApJ, 465, 608

Tollerud, E. J., Boylan-Kolchin, M., & Bullock, J. S. 2014, MNRAS, 440, 3511

Tollerud, E. J., Bullock, J. S., Strigari, L. E., & Willman, B. 2008, ApJ, 688, 277

Tolstoy, E. 2010, in IAU Symposium, Vol. 262, Stellar Populations - Planning for the Next Decade, ed. G. R. Bruzual & S. Charlot, 119–126

Tolstoy, E., Hill, V., & Tosi, M. 2009, ARA&A, 47, 371

Torrealba, G., Koposov, S. E., Belokurov, V., et al. 2016, MNRAS, 463, 712

Torrealba, G., Belokurov, V., Koposov, S. E., et al. 2018, MNRAS, 475, 5085

Tremonti, C. A., Heckman, T. M., Kauffmann, G., et al. 2004, ApJ, 613, 898

Trujillo-Gomez, S., Klypin, A., Colín, P., et al. 2015, MNRAS, 446, 1140

van den Bergh, S. 1999, A&A Rev., 9, 273

—. 2000, ApJ, 530, 777

van den Bergh, S., Cohen, J. G., Hogg, D. W., & Blandford, R. 2000, AJ, 120, 2190

Vargas, L. C., Geha, M., Kirby, E. N., & Simon, J. D. 2013, ApJ, 767, 134

Vera-Ciro, C. A., Helmi, A., Starkenburg, E., & Breddels, M. A. 2013, MNRAS, 428, 1696

Wadepuhl, M., & Springel, V. 2011, MNRAS, 410, 1975

Walker, M. G., Belokurov, V., Evans, N. W., et al. 2009, ApJ, 694, L144

Walsh, S. M., Willman, B., & Jerjen, H. 2009, AJ, 137, 450

Wang, J., Frenk, C. S., Navarro, J. F., Gao, L., & Sawala, T. 2012, MNRAS, 424, 2715

Watkins, L. L., Evans, N. W., Belokurov, V., et al. 2009, MNRAS, 398, 1757

Weisz, D. R., & Boylan-Kolchin, M. 2017, MNRAS, 469, L83

Weisz, D. R., Dolphin, A. E., Skillman, E. D., et al. 2014a, ApJ, 789, 147

—. 2014b, ApJ, 789, 148

White, S. D. M., & Rees, M. J. 1978, MNRAS, 183, 341

Willman, B., Governato, F., Dalcanton, J. J., Reed, D., & Quinn, T. 2004, MNRAS, 353, 639

Willman, B., Dalcanton, J. J., Martinez-Delgado, D., et al. 2005, ApJ, 626, L85

Wolf, J., Martinez, G. D., Bullock, J. S., et al. 2010, MNRAS, 406, 1220

Zucker, D. B., Belokurov, V., Evans, N. W., et al. 2006, ApJ, 643, L103

Zurita, C. 2011, CAMELOT: IAC80 TELESCOPE CCD - User Manual, Instituto de Astrofísica de Canarias

Zwaan, M. A., Meyer, M. J., & Staveley-Smith, L. 2010, MNRAS, 403, 1969

Agradecimientos

Como todo en esta vida, también este doctorado ha tenido sus altibajos. Tuve la oportunidad de hacer experiencias importantes y tener grandes satisfacciones, pero también experimentar momentos de dificultad y crisis.
No soy buena para hacer discursos, nunca lo he sido, pero creo que es mi deber agradecer a todas las personas que me han acompañado y apoyado en este camino y sin los cuales este trabajo de tesis no hubiese sido posible.

Antes de todo quiero agradecer a mi director de tesis, Sebastián Hidalgo, por las enseñanzas, la ayuda y los valiosos consejos que me ha dado durante estos años de doctorado. Gracias por su continua disponibilidad, paciencia y por haber depositado en mi su confianza. Gracias también por heber sido no solo un director de tesis, sino también un amigo en tiempos de dificultad, angustia y crisis. Si esta tesis ha llegado a su fin, gran parte del mérito se debe a él.
También me gustaría agradecer a todas las personas con las cuales he colaborado y que me han ayudado durante mi carrera científica (universidad y doctorado) entre los cuales en particular Antonio Aparicio, Ricardo Carrera, Antonino Milone, Matteo Monelli y Santi Cassisi. Gracias también a Casiana Muñoz Tuñón por sus comentarios y sugerencias que sin duda han mejorado el resultado final.

Un agradecimiento especial va a mis padres por el apoyo psicológico, moral y económico. Gracias por haberme dado siempre la posibilidad de elegir y de cometer errores; creo que esto me ha ayudado a crecer y madurar.
Agradezco a mi hermana Silvia porque, a pesar de las diferencias de carácter, me quiere y siempre está lista para ayudarme.

Gracias a mi tía Simonetta y a mi tío Claudio por haberme siempre tratado como una hija y por haber siempre creído en mí. Gracias por haberme mimado, por los mil discursos y los valiosos consejos.
A Alessandro y Luca digo siplemente: "¡Gracias por todo! Sois los mejores primos del mundo y os quiero mucho". Sé que durante los años que he vivido

en Tenerife nos hemos alejado un poco debido a la distancia, pero el afecto que nos une ha permanecido igual.

Le agradezco a mi mejor amiga Diana por haberme enseñado que es la amistad, aquella verdadera y sincera. Gracias por estar siempre allí cuando lo necesitaba, sé que puedo y podré siempre contar contigo. Gracias por haberme querido a tu lado en momentos importantes de tu vida, para considerarme parte de tu familia y por ser la "tía" de dos adorables niños, Leone y Camilla.

Agradezco a todos mis amigos y compañeros del IAC, con los cuales he compartido "alegrías y dolores" del doctorado y no solo... Durante estos años en Tenerife tuve la suerte de conocer gente maravillosa que he querido y sigo quierendo y que espero me acompañe a lo largo de mi vida, a pesar de la distancia que nos separa.
Gracias a Laura y Luis, por haber sido maravillosos compañeros de piso y por ciudarme tanto. Además, tengo que agradecer a Luis por todas las veces que me ha ayudado en asuntos de informática.
Gracias a Javi y Victor por haber sido los primeros dos españoles que he encontrado en la Universidad de La Laguna y por haber tratado de integrarme a pasar de que no hablaba nada de español. Gracias también por su ironía y por apreciar mi comida (especialmente el tiramisú).
Gracias a Paulo por su amistad y por todas las veces que ha escuchado mis quejas. Gracias también por vacillarme tanto, espero que haya servido a ser menos "inocentonta".
Gracias a Maria y Alba por estar siempre a mi lado cuando lo he necesitado.
Gracias a Federica por su ayuda y su apoyo moral durante el doctorado.
Muchas gracias a Stefano, sin él estos años en Tenerife no hubieran sido lo mismo. Gracias por haberme hecho descubrir una isla maravillosa y, sobre todo, por cuidarme durante estos años.

Me gustaría agradecer a la familia Peruzzo (Mariano, Mariarosa, Laura y Anna) por haberme aceptada desde el primer momento haciéndome sentir parte de su familia.

Gracias a todos mis viejos amigos (Rachele, Elena, Chiara, Riccardo, Michele, Luca, Daniele y Veronica) con quienes mantuve la amistad y que siempre traté de ver cada vez que volvía a Italia.

Un agradecimiento especial va a mi tía Renza. Su pérdida fue el momento más doloroso que tuve y que todavía intento lidiar. Nunca imaginé que ella no estaría presente en esto y en otros momentos importantes de mi vida, pero desafortunadamente las cosas no siempre van como lo deseamos. La extraño cada día y con ella se fue también una parte de mí. Gracias por haberme mimada, por haberme enseñado a perdonar y a no guardar rencor. Siempre

permanecerás en mi corazón.

El último agradecimiento va para una persona que ocupa un lugar especial en mi corazón, Luca. Entraste a mi vida en un momento de profundo dolor, tu fuiste oxígeno puro, me estaba ahogando y tu me salvaste. Gracias por creer en nosotros, por haber aguantado una relación a distancia sin quejarte, por haber estado siempre a mi lado y haber soportado mis momentos de depresión. Gracias por hacerme feliz todos los días.

La Laguna, 14 de mayo de 2018

Ringraziamenti

COME ogni cosa in questa vita, anche questo dottorato ha avuto i suoi alti e bassi. Ho avuto la possibilitá di fare esperienze importanti e di avere grandi soddisfazioni ma anche di vivere momenti di difficoltá e di crisi.
Non sono brava a fare discorsi, non lo sono mai stata, ma credo sia doveroso da parte mia ringraziare tutte le persone che a vario titolo mi hanno accompagnato e supportato in questo percorso e senza le quali questo lavoro di tesi non sarebbe stato possibile.

Prima di tutti voglio ringraziare il mio direttore di tesi, Sebastián Hidalgo, per gli insegnamenti, l'aiuto e i preziosi consigli datomi durante questi anni di dottorato. Grazie per la sua continua disponibilitá, per la pazienza e la fiducia che ha riposto in me. Grazie anche per essere stato non solo un direttore di tesi, ma anche un amico nei momenti di difficoltá, di sconforto e di crisi. Se questa tesi é giunta al termine, gran parte del merito va a lui.
Vorrei anche ringraziare tutte le persone con cui ho collaborato e che mi hanno aiutata durante il mio percorso scientifico (universitá e dottorato) tra i quali in particolare Antonio Aparicio, Ricardo Carrera, Antonino Milone, Matteo Monelli e Santi Cassisi. Grazie anche a Casiana Muñoz Tuñón per i suoi commenti e suggerimenti che senza dubbio hanno portato a un miglioramento del risultato finale.

Un ringraziamento speciale va ai miei genitori per il sostegno psicologico, morale ed economico. Grazie per avermi sempre dato la possibilitá di scegliere e di sbagliare; penso che questo mi abbia aiutata a crescere e maturare.
Ringrazio mia sorella Silvia perché, nonostante le divergenze di carattere, mi vuole bene ed é sempre pronta ad aiutarmi.

Grazie a mia zia Simonetta e a mio zio Claudio per avermi sempre trattata come una figlia e per aver sempre creduto in me. Grazie per avermi viziata e coccolata, per i mille discorsi e i preziosi consigli.
Ad Alessandro e Luca dico semplicemente: "Grazie di tutto! Siete i migliori

cugini del mondo e vi voglio un sacco di bene". So che i miei anni a Tenerife ci hanno allontanato un pó a causa della distanza ma l'affetto che ci lega é rimasto lo stesso.

Ringrazio la mia migliore amica Diana per avermi insegnato che cos'é l'amicizia, quella vera e sincera. Grazie per esserci sempre stata quando ne avevo bisogno, so che su di te posso e potró sempre contare. Grazie per avermi voluta accanto in momenti importanti della tua vita, per considerarmi parte della tua famiglia e per avermi resa la "zia" di due adorabili bambini, Leone e Camilla.

Ringrazio tutti i miei amici e colleghi dell'IAC, con i quali ho condiviso "gioie e dolori" del dottorato e non solo... Durante questi anni a Tenerife ho avuto la fortuna di conoscere persone meravigliose a cui ho voluto e voglio bene e che spero mi accompagneranno durante tutta la mia vita, nonostante la distanza che ci separa.
Grazie a Laura e Luis, per essere stati dei coinquilini meravigliosi e per essersi sempre presi cura di me. Inoltre devo ringraziare Luis per tutte le volte che mi ha aiutato nelle questioni informatiche.
Grazie a Javi e Victor per essere state le prime due persone spagnole che ho incontrato all'Universitá della Laguna e per aver cercato di farmi integrare nonostante non parlassi spagnolo. Grazie anche per la loro ironia e per apprezzare la mia cucina (soprattutto il tiramisú).
Grazie a Paulo per la sua amicizia e per tutte le volte che ha ascoltato le mie lamentele. Grazie anche per avermi preso in giro cosí tante volte semplicemente per rendermi piú forte e meno "tonta".
Grazie a Maria ed Alba per essermi sempre state accanto quando ne avevo bisogno.
Grazie a Federica per l'aiuto e il supporto morale durante il dottorato.
Grazie mille a Stefano, senza di lui questi anni a Tenerife non sarebbero stati la stessa cosa. Grazie per avermi fatto scoprire un'isola meravigliosa e soprattutto per esserti preso cura di me in questi anni.

Vorrei ringraziare la famiglia Peruzzo (Mariano, Mariarosa, Laura e Anna) per avermi accolta e accettata sin dal primo momento facendomi sentire parte della loro famiglia.

Grazie a tutti i miei amici di vecchia data (Rachele, Elena, Chiara, Riccardo, Michele, Luca, Daniele e Veronica) con i quali ho mantenuto un legame e che ho sempre cercato di vedere ogni volta che tornavo in Italia.

Un ringraziamento speciale va a mia zia Renza. La sua perdita é stato il momento piú doloroso che ho dovuto e che tuttora cerco affrontare. Non avrei mai immaginato che lei non sarebbe stata presente in questo e in altri momenti importanti della mia vita ma purtroppo le cose non vanno sempre

come vorremmo. Sento la sua mancanza ogni giorno e con lei se n'è andata anche una parte di me. Grazie per avermi viziata, coccolata, per avermi insegnato a perdonare e a non portare rancore. Resterai sempre nel mio cuore.

L'ultimo ringraziamento va a una persona che occupa un posto speciale nel mio cuore, Luca. Sei entrato nella mia vita in un momento di profondo dolore, tu sei stato ossigeno puro, stavo annegando e tu mi hai salvata. Grazie per aver creduto in noi, per aver saputo affrontare una relazione a distanza senza lamentarti, per essermi stato sempre vicino e per aver sopportato i miei momenti di depressione. Grazie per rendermi felice ogni giorno.

La Laguna, 14 maggio 2018